UNIVERSITY OF CALIFORNIA
RIVERSIDE

Molecular Beam Epitaxy Growth of Monolayer Hexagonal Boron Nitride Films for Metal-Insulator-Metal Devices

A Dissertation submitted in partial satisfaction
of the requirements for the degree of

Doctor of Philosophy

in

Electrical Engineering

by

Yanwei He

June 2021

Dissertation Committee:
Dr. Jianlin Liu, Chairperson
Dr. Ming Liu
Dr. Yongtao Cui

The Dissertation of Yanwei He is approved:

_____

_____

_____

Committee Chairperson

University of California, Riverside

ACKNOWLEDGEMENTS

I would like to express my deepest appreciation to my advisor, Prof. Jianlin Liu, who is an honorable researcher, a supportive mentor, and a genuine friend. He consistently inculcates the spirit of rigor, hard work, and the aspiration of knowledge in me. Without his guidance and persistent help, this dissertation would not have been possible. Besides my advisor, I would like to thank my final dissertation defense committee members, Prof. Ming Liu and Prof. Yongtao Cui, for their insightful comments and constructive advice.

I am grateful to have established lifelong friendship with my wonderful lab mates: Dr. Mohammad Suja, Dr. Sunayna Bashar, Dr. Renjing Zheng, Dr. Jingchuan Yang, Dr. Dakuan Zhang, Dr. Alireza Khanaki, Dr. Hao Tian, Dr. Long Xu, Dr, Caixia Xu, Mr. Wenhao Shi, Miss. Zhenjun Cui, Mr. Ivan Chiang, Mr. Yuan Li, Mr. Tianchen Yang, and Mr. Chengyun Shou. We supported each other through hard time, and shared joys of success. Thanks for the help and company. I am also thankful to the following university staff who are always ready to lend a helping hand: Mrs. Kim Underhill, Dr. Yandong, Dr. Mark Heiden, Mr. Manglai Zhou.

Finally, I would like to thank my parents, sisters, and my fiancée for their unconditional love and support. They are the source of my strength, and the reason that I strive for a better self. I am so lucky to be able to explore all the life possibilities knowing they will always be there for me. My parents showed me the spirit of being industrious and persevering, and I will continue to use them to pursue for a better life and make the world a better place.

Previously Published Material Acknowledgment:

1. The results in Chapter 2 were published in:

   He, Y.; Tian, H.; Khanaki, A.; Shi, W.; Tran, J.; Cui, Z.; Wei, P.; Liu, J. Large-Area Adlayer-Free Single-Layer h-BN Film Achieved by Controlling Intercalation Growth. *Applied Surface Science* **2019,** *498*, 143851.

2. The results in Chapter 3 were published in:

   He, Y.; Tian, H.; Das, P.; Cui, Z.; Pena, P.; Chiang, I.; Shi, W.; Xu, L.; Li, Y.; Yang, T., Growth of High-Quality Hexagonal Boron Nitride Single-Layer Films on Carburized Ni Substrates for Metal–Insulator–Metal Tunneling Devices. *ACS Applied Materials & Interfaces* **2020,** *12* (31), 35318-35327.

3. The results in Chapter 4 were published in:

   He, Y.; Li, Y.; Isarraraz, M.; Pena, P.; Tran, J.; Xu, L.; Tian, H.; Yang, T.; Wei, P.; Ozkan, C. S., Robust Nanocapacitors Based on Wafer-Scale Single-Crystal Hexagonal Boron Nitride Monolayer Films. *ACS Applied Nano Materials* **2021** (DOI: 10.1021/acsanm.1c00298)

I dedicate my dissertation work to
my parents (何永涛 and 张子兰)
and my fiancée (徐嘉惠)

ABSTRACT OF THE DISSERTATION

Molecular Beam Epitaxy Growth of Monolayer Hexagonal Boron Nitride Films for Metal-Insulator-Metal Devices

by

Yanwei He

Doctor of Philosophy, Graduate Program in Electrical Engineering
University of California, Riverside, June 2021
Dr. Jianlin Liu, Chairperson

Two-dimensional (2D) hexagonal boron nitride (h-BN) plays a significant role in nanoscale electrical and optical devices because of its superior properties. However, the difficulties in the controllable growth of high-quality films hinder its applications. In this thesis, we focus on improving the quality of h-BN films with molecular beam epitaxy (MBE), and implementing the as-grown monolayer h-BN films in metal-insulator-metal (MIM) devices.

In the first project, i.e., Chapter 2, we present a study of h-BN adlayer growth and provide a strategy towards eliminating these adlayers for the precise control of the number of 2D layers. By varying the growth parameters such as substrate property, nitrogen source composition, and substrate carburization time, we found that the adlayer growth can be controlled by controlling the nucleation and intercalation processes, which is achieved by engineering the defects and impurities on substrate and the activeness of the h-BN edges.

In the second project, i.e., Chapter 3, we report a study of 2D h-BN growth on carburized Ni substrates. It was found that the carburization of Ni substrates with different surface orientations leads to different kinetics of h-BN growth. While the carburization of Ni (100)

enhances the h-BN growth, the speed of the h-BN growth on carburized Ni (111) reduces. As grown continuous monolayer h-BN films are used to fabricate Ni/h-BN/Ni MIM devices, which demonstrate a high breakdown electric field of 12.9 MV/cm.

In the last project, i.e., Chapter 4, we report an effective method to synthesize single-crystal monolayer h-BN films. We discovered that electropolishing plays an important role in drastically increasing the speed of h-BN film growth. 1-in^2 monolayer single-crystal h-BN films are obtained within 1 hour by MBE. Robust nano capacitors were fabricated using as grown monolayer h-BN films. The nano-capacitance effect and tunneling current mechanism were studied in detail, and the 'effective distance' concept is introduced to explain the quantum phenomenon in the van der Waals MIM devices using atomically thin dielectric h-BN films.

Table of Contents

List of Figures

Chapter 1: Introduction

1.1 Two-dimensional van der Waals materials

Ever since the isolation of graphene in 2004 [1], 2D materials have grown into a large family consisting of more than 2500 members. These materials showcase unprecedent electrical, optical, chemical, and mechanical properties, and demonstrate promising potential in various applications such as devices fabrication [2], sensing [3], catalysis [4], energy storage [5], etc. Take graphene as an example: its electron mobility is almost 200 times higher than Si; it conducts heat 2 times better than diamond; and it is 100 times stronger than steel of the same thickness [6]. Graphene and other graphene-like 2D materials are expected to be the new silicon for next-generation electronic devices as Moore's law reaches its limit.

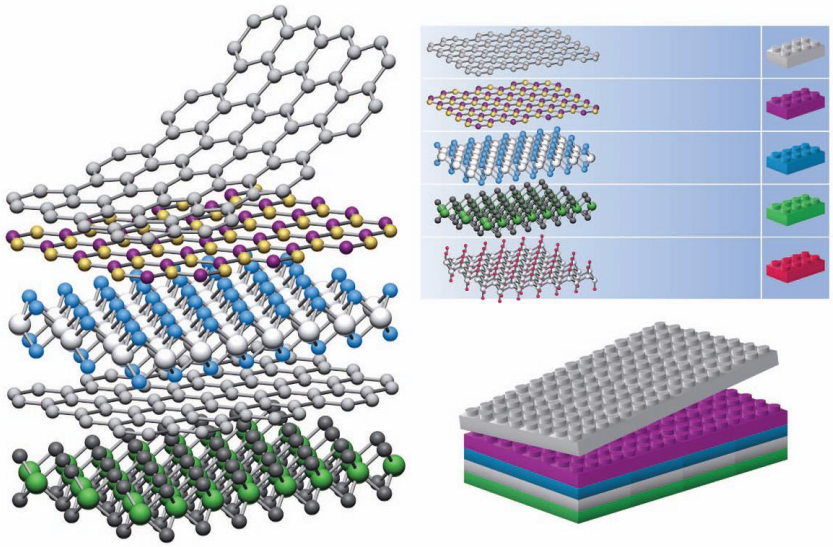

Figure 1.1. Van der Wall materials and their heterostructures in analog to Lego blocks [7]. Adapted with permission.

Featured by the in-plane covalent bond and out-of-plane van der Waals interaction, 2D materials can be reduced down to one atomic layer, and they can also be stacked up to

arbitrary thickness and composition like Lego blocks. As is illustrated in Figure 1.1, because of the weak out-of-plane interaction, 2D materials can be stacked together to form hybrid heterostructures. Due to the strong interlayer coupling and quantum confinement, the optical and electrical properties of 2D materials can be tailored by the number of layers and the way they are stacked. For example, molybdenum disulfide (MoS_2) has direct band gap (1.8 eV) as monolayer, but indirect bandgap when it is bilayer or few-layer [8]. More interestingly, it is found recently that when bilayer graphene is twisted in a magic angle of 1.1 degree, it demonstrates superconductivity, which gives rise to a new field called "twistronics" [9, 10]. By precisely controlling the way 2D materials are stacked, novel electronic and optoelectronic devices can be achieved.

There are two major ways to obtain 2D materials. One is the top-down approach, namely, obtain the 2D material by thinning its bulk materials. The most popular top-down method is called exfoliation, which can be analogous to the disassembling of a Lego structure. There are many ways of exfoliation, such as mechanical exfoliation [11], liquid phase exfoliation [12], and electrochemical exfoliation [13]. Exfoliation is a simple and low-cost approach to acquire 2D materials and has been widely used for research purposes. However, it does not support mass production of uniform films as the size of exfoliated flakes are only in millimeters at most. The exfoliated 2D flakes then can be stack layer by layer using transfer techniques. Figure 1.2 shows the fabrication of h-BN/Graphene/h-BN heterostructure. Again, the handcraft transfer procedure serves research purpose well as it is simple and low-cost, but it does not support mass production. Also, the contaminations

from polymer carrier and ambient adsorbates trapped between the layers hamper the performances of fabricated devices [15].

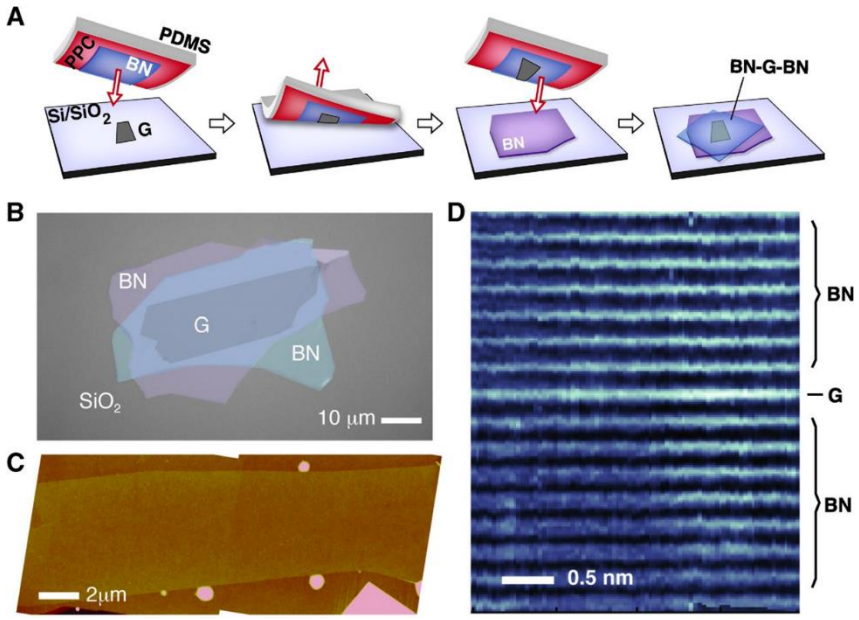

Figure 1.2. Polymer-free layer assembly. (**A**) Schematic of the van der Waals technique for polymer-free assembly of layered materials. (**B**) Optical image of a multi-layered heterostructure using the process illustrated in (A). (**C**) AFM image of a large-area encapsulated graphene layer showing that it is pristine and completely free of wrinkles or bubbles except at its boundary. (**D**) High-resolution cross-section ADF-STEM image of the device in (C). The BN-G-BN interface is found to be pristine and free of any impurities down to the atomic scale. Adapt with permission from AAAS.[14]

The other approach is called bottom-up, namely, synthesizing 2D materials from atomic or molecular precursors. There are many bottom-up methods to choose from, such as molecular beam epitaxy (MBE) [16, 19], chemical vapor deposition (CVD) [20, 22], atomic layer deposition (ALD) [23, 24], etc. The bottom-up approach is promising to be industrialized as it supports wafer-scale production of 2D films and their heterostructures. Significant effort has been made in the past decades along this direction, and some groups have reported the growth of wafer-scale single crystal graphene [25], h-BN [26, 28], and MoS_2 [29]. However, the

growth dynamic of 2D materials rely strongly on the supporting substrate. For example, wafer-scale single crystal h-BN film was only achieved on certain metal surfaces, where the catalytic effect can be utilized [26, 28]. There are still a lot of work to do to find the right conditions to grow wafer-scale 2D films on arbitrary substrate with controllable thickness and high crystallinity.

1.2 Hexagonal boron nitride (h-BN)

Hexagonal boron nitride (h-BN), the so-called white graphene, is an important member in 2D family. It has the same honeycomb-sp2 structure as graphene, but because of the strongly polarized B-N bond, it has a wide bandgap of around 6 eV [30]. It also has high breakdown electric filed [31], high thermal conductivity [32], and is chemically stable [33]. With these attributes, h-BN is a perfect insulating layer in van der Waals systems.

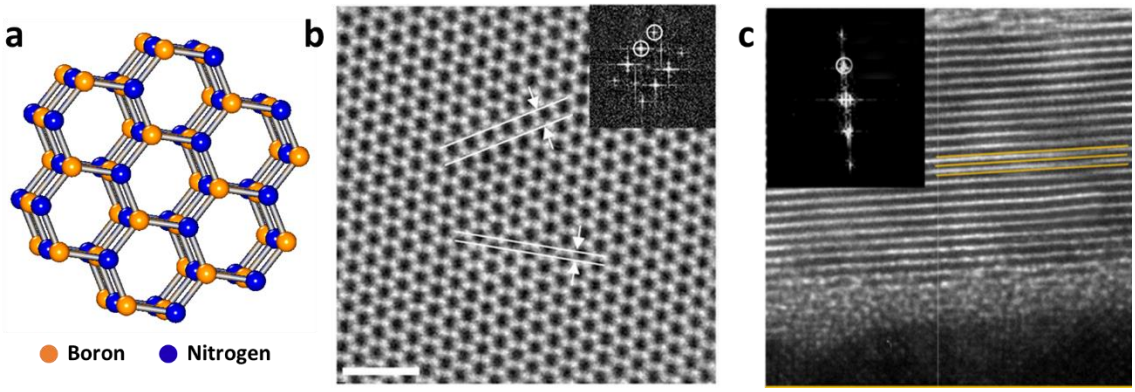

Figure 1.3. Structure of h-BN. (a) Schematic of tri-layer h-BN. (b) high-angle annular dark-field STEM image of a multilayer h-BN film; the inset shows the corresponding fast Fourier transform (FFT) image; (c) cross-sectional TEM images of a multilayer h-BN film; the inset shows the corresponding FFT image. Adapted with permission from FEF.[34], CC BY 4.0.

Figure 1.3a shows the atomic model of multilayer h-BN, with the orange and blue balls representing boron and nitrogen atoms, respectively. Figure 1.3b and 1.3c are the high-

resolution transmission electron microscopy (TEM) images from bird-view and cross-sectional view. The lattice constant of h-BN is about 2.5 Å for in-plane, 6.6 Å for out-of-plane, and the interlayer distance is about 3.3 Å, very close to that of graphene. H-BN has been used as dielectric layer in transistors [35], capacitors [36], and resistive switching devices [37, 38]. The out of plane dielectric constant of h-BN is 3 ~ 4 [39, 40], and the breakdown electric field is 7 ~ 12 MV/cm according to literature [41, 42]. The resistive switching property of h-BN is related to the defects and grain boundaries in polycrystal h-BN films, where metal ions can accumulate to form the conductive filament [37, 43]. The defects and grain boundaries are formed during growth, hence h-BN demonstrates forming free resistive switching properties. The surface of h-BN is atomically flat and dangling bond free, therefore, h-BN has also been used as anti-scattering substrate for graphene, MoS_2 and other 2D materials to improve their performances [44, 45]. For example, the mobility of graphene can be significantly increased by replacing the SiO_2 substrate with h-BN [44].

In addition to electronic devices, h-BN has also been used in novel optoelectronic devices. It has been demonstrated that bulk h-BN has indirect bandgap, and monolayer h-BN has direct bandgap [46]. Because of the wide band gap of around 6 eV, h-BN can be used for deep ultraviolet (DUV) emitter at wavelength of 215 nm [47]. Bright luminescent emission was observed in single crystal h-BN under excitation current. However, due to extremely low carrier density, electrically pumped DUV emitter was barely reported. Some efforts have been made to dope h-BN with II-IV group elements to achieve desired electronic and optical properties. P-type h-BN was reported with Be and Mg as dopants [48], and N-type h-BN was reported with C, Si, Ge, as dopants [49]. However, due to the large

energy difference between B-N bonds and B/N-dopant bonds, the dopants can hardly be incorporated evenly [50]. There are still a lot of work to do to find the right condition for controllable doping of h-BN. Another optoelectronic application of h-BN is single photon emission (SPE). This is a relatively new topic emerged in 2016 [51]. The SPE emitters in h-BN are associated with point defects, such as the anti-site defect NBVN, in which a nitrogen site is vacant, and the neighbor boron atom is substituted by a nitrogen [51]. The point defects can be introduced via thermal annealing and plasma/electron beam bombardment [52]. H-BN has been considered a promising 2D materials for future semiconductor quantum information processing technologies.

1.3 Molecular beam epitaxy (MBE)

Molecular beam epitaxy (MBE) is one of the bottom-up methods talked in previous section for thin film deposition. This technology was proposed by K.Z. Günther in 1958 [53], and the first successful epitaxial growth of semiconductor thin film (GaAs) was reported by J.E. Davey and T. Pankey in 1968 [54]. Since then, MBE has been widely used in semiconductor device fabrication.

MBE growth takes place in chamber with ultra-high vacuum (10^{-8}–10^{-12} Torr), which is maintained by a combination of mechanical, turbo, ion, and cryo- pumps. In a typical solid source MBE, ultra-pure elemental sources are put in separate Knudsen effusion cells, where they are heated up until sublime begins. The gaseous elements form collimated beams due to the long mean free path under the ultra-high vacuum and impinge on the substate where they can react with each other. The substrate is also heated up to a proper

Figure 1.4. Photo of Perkin Elmer 425 MBE system. (adapted from the corresponding manual book).

growth temperature to enable the reaction. The growth rate of thin film can be monitored by in-situ reflection high-energy electron diffraction (RHEED). Based on this set up, MBE has some apparent advantages over other deposition techniques, such as the fine control of film thickness and composition, and high purity of deposited thin film. But it is also less favored for industrialized mass production due to the high cost. Figure 1.4 shows a photo of the Perkin Elmer 425 MBE system equipped in our lab. Boron is supplied by a Knudsen effusion cell filled with B_2O_3 powder (Alfa Aesar, 99.999% purity); Ammonia gas (American Gas Group, 99.9995% purity) and N_2 plasma (Airgas, 99.9999% purity) generated by an electron cyclotron resonance (ECR) plasma generator are used as nitrogen source; C_2H_2 (Airgas, Atomic Absorption Grade) is used as carbon source for carburization. The gas flow is controlled by mass flow controller (MFC).

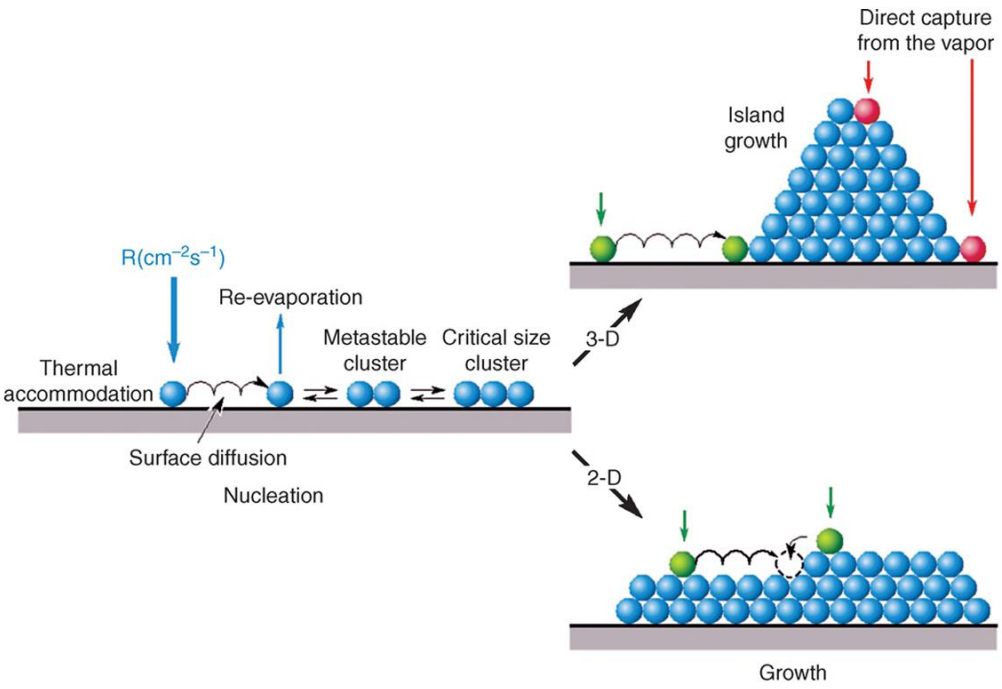

Figure 1.5. Schematic representation of MBE growth process. Adapt with permission [55].

The MBE growth mechanism is illustrated in Figure 1.5. Once the atom flux reaches the substrate surface, certain number of atoms will be physically adsorbed. The adsorbed atoms (adatoms) then undergo surface diffusion to find the energetically favorable position or bonds with other adatoms to form nuclei. The preferred adsorption and nucleation sites are the crystallographic defects and steps that are chemically reactive. During this process, some adatoms will desorb from the surface. The adsorption, desorption, diffusion, and bonding processes determine the thin film growth rate, which are all related to the substrate temperature. In general, higher temperature will promote the diffusion, and bonding processes (assuming the temperature is not high enough to break the bonds), which propel the growth; but it also hinders the adsorption process (or promote the desorption), which slows down the growth [56, 57]. Therefore, finding the proper growth temperature is very

important in MBE growth. Based on different interaction strength between the adatoms and the surface, the thin film grows majorly in three different mode [55, 58]. In the Volmer-Weber (VW) mode, the interaction of adatoms-adatoms is stronger than that of adatoms-surface, resulting in the formation of three-dimensional (3D) clusters or islands. Antithetically, in the Frank-van der Merwe (FM) mode, the adatoms-adatoms interaction is weaker than that of adatoms-surface, resulting in the growth of atomically smooth two-dimensional (2D) films. Stranski–Krastanov mode is an intermediate process which involves both 2D and 3D growth. Transition from layer-to-layer to island/cluster growth occurs at a critical film thickness where strain accumulates at certain area and results in the 3D growth. Due to the strong in-plane covalent bonds and weak out-of-plane van der Waals interaction, the growth of van der Waals materials is considered to follow the FM mode [59].

1.4 Chapter's arrangement

In this dissertation, we will present our work in the controllable growth of h-BN using MBE and the implementation of monolayer h-BN film in metal-insulator-metal (MIM) devices.

In Chapter 2, we provide a comprehensive study of the growth mechanism of h-BN aiming to understand how growth factors impact the growth process. We studied the h-BN growth on two different substrates, Co and Ni. Each of them can be further divided into two types, pristine and carburized. The h-BN is grown with two different types of N source, ammonia and nitrogen plasma, which can be regarded as molecular and atomic source, respectively. The influence of hydrogen passivation and plasma bombardment effect are

studied in detail. A strategy to eliminate the intercalation growth of adlayers is provided based on the study above, and large area adlayer-free monolayer h-BN film is obtained.

The study in Chapter 2 reveals that Ni is a proper substrate for h-BN growth. Therefore, in Chapter 3, we focus on the study of h-BN growth on Ni substrate. We studied the growth of h-BN on two different surface directions, (111) and (100). It turns out the growth temperature and growth rate on (111) surface is lower than that of (100) surface. While the carburization can promote growth on (100) surface, it hampers the growth on (111) surface. DFT calculation is employed to explain the observed phenomenon. MIM devices are fabricated to study the dielectric properties of as-grown films.

In Chapter 4, we further improve the growth of h-BN film by introducing wafer-scale single crystal substrate and electropolishing. The growth speed of h-BN is drastically increased after electropolishing, as a result, wafer-scale single-crystal monolayer h-BN films are achieved within a growth time of 1 hour. Low-energy deposition of Al is introduced in fabrication of MIM devices to alleviate the damage from metallization, and robust nanocapacitors are successfully fabricated. The tunneling behavior between asymmetric electrodes and the quantum capacitance effect are studied in depth. Effective distance between two electrodes is introduced to explain the observed phenomena.

These three chapters show a clear path of improving the quality of h-BN films and the performance of MIM devices. Lastly, in Chapter 5, we will conclude the dissertation work in a short summary.

1.5 References

1. Novoselov, K. S.; Geim, A. K.; Morozov, S. V.; Jiang, D.; Zhang, Y.; Dubonos, S. V.; Grigorieva, I. V.; Firsov, A. A., Electric Field Effect in Atomically Thin Carbon Films. *Science* **2004,** *306* (5696), 666-669.

2. Liu, Y., Weiss, N.O., Duan, X., Cheng, H.C., Huang, Y. and Duan, X., Van der Waals Heterostructures and Devices. *Nature Reviews Materials* **2016**, *1* (9), 1-17.

3. Yan, W., Fuh, H.R., Lv, Y., Chen, K.Q., Tsai, T.Y., Wu, Y.R., Shieh, T.H., Hung, K.M., Li, J., Zhang, D. and Coileáin, C.Ó., Giant Gauge Factor of Van der Waals Material Based Strain Sensors. *Nature Communications* **2021**, *12* (1), 1-9.

4. Deng, D., Novoselov, K.S., Fu, Q., Zheng, N., Tian, Z. and Bao, X., Catalysis with Two-Dimensional Materials and Their Heterostructures. *Nature Nanotechnology* **2016**, *11* (3), 218-230.

5. Zhang, P., Wang, F., Yu, M., Zhuang, X. and Feng, X., Two-Dimensional Materials for Miniaturized Energy Storage Devices: from Individual Devices to Smart Integrated Systems. *Chemical Society Reviews* **2018**, *47* (19), 7426-7451.

6. Radamson H.H. Graphene. In: Kasap S., Capper P. (eds) Springer Handbook of Electronic and Photonic Materials. *Springer Handbooks. Springer, Cham* **2017**

7. Geim, A.K. and Grigorieva, I.V., Van der Waals Heterostructures. *Nature* **2013**, *499* (7459), 419-425.

8. Mak, K.F., Lee, C., Hone, J., Shan, J. and Heinz, T.F., Atomically Thin MoS_2: A New Direct-Gap Semiconductor. *Physical Review Letters* **2010**, *105* (13), 136805.

9. Cao, Y., Fatemi, V., Fang, S., Watanabe, K., Taniguchi, T., Kaxiras, E. and Jarillo-Herrero, P., Unconventional Superconductivity in Magic-Angle Graphene Superlattices. *Nature* 2018, *556* (7699), 43-50.

10. Tarnopolsky, G., Kruchkov, A.J. and Vishwanath, A., Origin of Magic Angles in Twisted Bilayer Graphene. *Physical Review Letters* **2019**, *122* (10), 106405.

11. Yi, M. and Shen, Z., A Review on Mechanical Exfoliation for the Scalable Production of Graphene. *Journal of Materials Chemistry A* **2015**, *3* (22), 11700-11715.

12. Hernandez, Y., Nicolosi, V., Lotya, M., Blighe, F.M., Sun, Z., De, S., McGovern, I.T., Holland, B., Byrne, M., Gun'Ko, Y.K. and Boland, J.J., High-Yield Production of Graphene by Liquid-Phase Exfoliation of Graphite. *Nature Nanotechnology* **2008**, *3* (9), 563-568.

13. Su, C.Y., Lu, A.Y., Xu, Y., Chen, F.R., Khlobystov, A.N. and Li, L.J., High-Quality Thin Graphene Films from Fast Electrochemical Exfoliation. *ACS Nano* **2011**, *5* (3), 2332-2339.

14. Wang, L., Meric, I., Huang, P.Y., Gao, Q., Gao, Y., Tran, H., Taniguchi, T., Watanabe, K., Campos, L.M., Muller, D.A. and Guo, J., One-Dimensional Electrical Contact to A Two-Dimensional Material. Science **2013**, *342* (6158), 614-617.

15. Gasparutti, I., Song, S.H., Neumann, M., Wei, X., Watanabe, K., Taniguchi, T. and Lee, Y.H., How Clean Is Clean? Recipes for van der Waals Heterostructure Cleanliness Assessment. *ACS Applied Materials & Interfaces* **2020**, *12* (6), 7701-7709.

16. Nakhaie, S.; Wofford, J.; Schumann, T.; Jahn, U.; Ramsteiner, M.; Hanke, M.; Lopes, J.; Riechert, H. Synthesis of Atomically Thin Hexagonal Boron Nitride Films on Nickel Foils by Molecular Beam Epitaxy. *Applied Physics Letters* **2015**, *106* (21), 213108.

17. Vuong, T.; Cassabois, G.; Valvin, P.; Rousseau, E.; Summerfield, A.; Mellor, C.; Cho, Y.; Cheng, T.; Albar, J. D.; Eaves, L. Deep Ultraviolet Emission in Hexagonal Boron Nitride Grown by High-Temperature Molecular Beam Epitaxy. *2D Materials* **2017**, *4* (2), 021023.

18. Cho, Y.-J.; Summerfield, A.; Davies, A.; Cheng, T. S.; Smith, E. F.; Mellor, C. J.; Khlobystov, A. N.; Foxon, C. T.; Eaves, L.; Beton, P. H. Hexagonal Boron Nitride Tunnel Barriers Grown on Graphite by High Temperature Molecular Beam Epitaxy. *Scientific Reports* **2016**, *6*, 34474.

19. Pierucci, D., Zribi, J., Henck, H., Chaste, J., Silly, M.G., Bertran, F., Le Fevre, P., Gil, B., Summerfield, A., Beton, P.H. and Novikov, S.V. Van der Waals Epitaxy of Two-Dimensional Single-Layer H-BN on Graphite by Molecular Beam Epitaxy: Electronic Properties and Band Structure. *Applied Physics Letters* **2018**, *112* (25), 253102.

20. Wang, S., Wang, X. and Warner, J.H., All Chemical Vapor Deposition Growth of MoS2: h-BN Vertical van der Waals Heterostructures. *ACS Nano*, **2015**, *9* (5), 5246-5254.

21. Kim, K.K., Hsu, A., Jia, X., Kim, S.M., Shi, Y., Hofmann, M., Nezich, D., Rodriguez-Nieva, J.F., Dresselhaus, M., Palacios, T. and Kong, J., Synthesis of Monolayer Hexagonal Boron Nitride on Cu Foil Using Chemical Vapor Deposition. *Nano Letters*, **2012**, *12* (1), 161-166.

22. Shi, Y., Hamsen, C., Jia, X., Kim, K.K., Reina, A., Hofmann, M., Hsu, A.L., Zhang, K., Li, H., Juang, Z.Y. and Dresselhaus, M.S., Synthesis of Few-Layer Hexagonal Boron Nitride Thin Film by Chemical Vapor Deposition. *Nano Letters*, **2010**, *10* (10), 4134-4139.

23. Ferguson, J.; Weimer, A.; George, S. Atomic Layer Deposition of Boron Nitride Using Sequential Exposures of BCl_3 and NH_3. *Thin Solid Films* **2002**, *413* (1-2), 16-25.

24. Driver, M. S.; Beatty, J. D.; Olanipekun, O.; Reid, K.; Rath, A.; Voyles, P. M.; Kelber, J. A. Atomic Layer Epitaxy of h-BN (0001) Multilayers on Co (0001) and Molecular Beam Epitaxy Growth of Graphene on h-BN (0001)/Co (0001). *Langmuir* **2016**, *32* (11), 2601-2607.

25. Lee, Y., Bae, S., Jang, H., Jang, S., Zhu, S.E., Sim, S.H., Song, Y.I., Hong, B.H. and Ahn, J.H., Wafer-scale synthesis and transfer of graphene films. *Nano Letters* **2010**, *10* (2), 490-493.

26. Lee, J.S., Choi, S.H., Yun, S.J., Kim, Y.I., Boandoh, S., Park, J.H., Shin, B.G., Ko, H., Lee, S.H., Kim, Y.M. and Lee, Y.H., Wafer-Scale Single-Crystal Hexagonal Boron Nitride Film via Self-Collimated Grain Formation. *Science* **2018**, *362* (6416), 817-821.

27. Chen, T.A., Chuu, C.P., Tseng, C.C., Wen, C.K., Wong, H.S.P., Pan, S., Li, R., Chao, T.A., Chueh, W.C., Zhang, Y. and Fu, Q., Wafer-Scale Single-Crystal Hexagonal Boron Nitride Monolayers on Cu (111). *Nature* **2020**, *579* (7798), 219-223.

28. Wang, L., Xu, X., Zhang, L., Qiao, R., Wu, M., Wang, Z., Zhang, S., Liang, J., Zhang, Z., Zhang, Z. and Chen, W., Epitaxial Growth of a 100-Square-Centimetre Single-Crystal Hexagonal Boron Nitride Monolayer on Copper. *Nature* **2019**, *570* (7759), 91-95.

29. Yu, H., Liao, M., Zhao, W., Liu, G., Zhou, X.J., Wei, Z., Xu, X., Liu, K., Hu, Z., Deng, K. and Zhou, S., Wafer-Scale Growth and Transfer of Highly Oriented Monolayer MoS_2 Continuous Films. *ACS Nano* **2017**, *11* (12), 12001-12007.

30. Cassabois, G.; Valvin, P.; Gil, B. Hexagonal Boron Nitride Is an Indirect Bandgap Semiconductor. *Nature Photonics* **2016**, *10* (4), 262-266.

31. Hattori, Y.; Taniguchi, T.; Watanabe, K.; Nagashio, K. Layer-by-Layer Dielectric Breakdown of Hexagonal Boron Nitride. *ACS Nano* **2015**, *9* (1), 916-921.

32. Jo, I.; Pettes, M. T.; Kim, J.; Watanabe, K.; Taniguchi, T.; Yao, Z.; Shi, L. Thermal Conductivity and Phonon Transport in Suspended Few-Layer Hexagonal Boron Nitride. *Nano Letters* **2013**, *13* (2), 550-554.

33. Kostoglou, N.; Polychronopoulou, K.; Rebholz, C. Thermal and Chemical Stability of Hexagonal Boron Nitride (h-BN) Nanoplatelets. *Vacuum* **2015**, *112*, 42-45.

34. Kim, S.M., Hsu, A., Park, M.H., Chae, S.H., Yun, S.J., Lee, J.S., Cho, D.H., Fang, W., Lee, C., Palacios, T. and Dresselhaus, M., Synthesis of Large-Area Multilayer Hexagonal Boron Nitride for High Material Performance. *Nature Communications* **2015**, *6* (1), 1-11.

35. Lee, G.-H.; Yu, Y.-J.; Cui, X.; Petrone, N.; Lee, C.-H.; Choi, M. S.; Lee, D.-Y.; Lee, C.; Yoo, W. J.; Watanabe, K. Flexible and Transparent MoS2 Field-Effect Transistors on Hexagonal Boron Nitride-Graphene Heterostructures. *ACS Nano* **2013**, *7* (9), 7931-7936.

36. Jang, S. K.; Youn, J.; Song, Y. J.; Lee, S. Synthesis and Characterization of Hexagonal Boron Nitride as a Gate Dielectric. *Scientific Reports* **2016**, *6*, 30449.

37. Jing, X.; Puglisi, F.; Akinwande, D.; Lanza, M. Chemical Vapor Deposition of Hexagonal Boron Nitride on Metal-Coated Wafers and Transfer-Free Fabrication of Resistive Switching Devices. *2D Materials* **2019**, *6* (3), 035021.

38. Pan, C.; Miranda, E.; Villena, M. A.; Xiao, N.; Jing, X.; Xie, X.; Wu, T.; Hui, F.; Shi, Y.; Lanza, M. Model for Multi-Filamentary Conduction in Graphene/Hexagonal-Boron-Nitride/Graphene Based Resistive Switching Devices. *2D Materials* **2017**, *4* (2), 025099.

39. Hong, S.; Lee, C.-S.; Lee, M.-H.; Lee, Y.; Ma, K. Y.; Kim, G.; Yoon, S. I.; Ihm, K.; Kim, K.-J.; Shin, T. J., Ultralow-dielectric-constant amorphous boron nitride. *Nature* **2020,** *582* (7813), 511-514.

40. Laturia, A., Van de Put, M.L. and Vandenberghe, W.G., Dielectric properties of hexagonal boron nitride and transition metal dichalcogenides: from monolayer to bulk. *NPJ 2D Mater. Appl.* **2018**, *2* (1), 1-7.

41. Hattori, Y., Taniguchi, T., Watanabe, K. and Nagashio, K., Layer-by-Layer Dielectric Breakdown of Hexagonal Boron Nitride. *ACS nano*, **2015**, *9* (1), 916-921.

42. Cui, Z., He, Y., Tian, H., Khanaki, A., Xu, L., Shi, W. and Liu, J., Study of Direct Tunneling and Dielectric Breakdown in Molecular Beam Epitaxial Hexagonal Boron Nitride Monolayers Using Metal–Insulator–Metal Devices. *ACS Applied Electronic Materials* **2020**, *2* (3), 747-755.

43. Pan, C.; Ji, Y.; Xiao, N.; Hui, F.; Tang, K.; Guo, Y.; Xie, X.; Puglisi, F. M.; Larcher, L.; Miranda, E., Coexistence of Grain-Boundaries-Assisted Bipolar and Threshold Resistive Switching in Multilayer Hexagonal Boron Nitride. *Advanced Functional Materials* **2017,** *27* (10), 1604811.

44. Dean, C.R., Young, A.F., Meric, I., Lee, C., Wang, L., Sorgenfrei, S., Watanabe, K., Taniguchi, T., Kim, P., Shepard, K.L. and Hone, J., Boron Nitride Substrates for High-Quality Graphene Electronics. *Nature Nanotechnology*, **2010**, *5* (10), 722-726.

45. Lee, G.H., Yu, Y.J., Cui, X., Petrone, N., Lee, C.H., Choi, M.S., Lee, D.Y., Lee, C., Yoo, W.J., Watanabe, K. and Taniguchi, T., Flexible and Transparent MoS_2 Field-Effect Transistors on Hexagonal Boron Nitride-Graphene Heterostructures. *ACS Nano*, **2013**, *7* (9), 7931-7936.

46. Elias, C., Valvin, P., Pelini, T., Summerfield, A., Mellor, C.J., Cheng, T.S., Eaves, L., Foxon, C.T., Beton, P.H., Novikov, S.V. and Gil, B., Direct Band-Gap Crossover in Epitaxial Monolayer Boron Nitride. *Nature Communications* **2019**, *10* (1), 1-7.

47. Watanabe, K., Taniguchi, T. and Kanda, H., Direct-Bandgap Properties and Evidence for Ultraviolet Lasing of Hexagonal Boron nitride single crystal. *Nature Materials* **2004**, *3* (6), 404-409.

48. Sun, F., Hao, Z., Liu, G., Wu, C., Lu, S., Huang, S., Liu, C., Hong, Q., Chen, X., Cai, D. and Kang, J., P-Type Conductivity of Hexagonal Boron Nitride As A Dielectrically Tunable Monolayer: Modulation Doping with Magnesium. *Nanoscale* **2018**, *10* (9), 4361-4369.

49. Ding, Y.M., Shi, J.J., Zhang, M., Jiang, X.H., Zhong, H.X., Huang, P., Wu, M. and Cao, X., Improvement of n-Type Conductivity in Hexagonal Boron Nitride Monolayers by Doping, Strain and Adsorption. *RSC Advances* **2016**, *6* (35), 29190-29196.

50. Xie, W., Yanase, T., Nagahama, T. and Shimada, T., Carbon-Doped Hexagonal Boron Nitride: Analysis as π-Conjugate Molecules Embedded in Two-Dimensional Insulator. *C* **2016**, *2* (1), 2.

51. Tran, T. T.; Bray, K.; Ford, M. J.; Toth, M.; Aharonovich, I., Quantum Emission from Hexagonal Boron Nitride Monolayers. *Nature Nanotechnology* **2015**, *11*, 37-41.

52. Xu, Z.Q., Elbadawi, C., Tran, T.T., Kianinia, M., Li, X., Liu, D., Hoffman, T.B., Nguyen, M., Kim, S., Edgar, J.H. and Wu, X., Single Photon Emission from Plasma Treated 2D Hexagonal Boron Nitride. *Nanoscale* **2018**, *10* (17), 7957-7965.

53. Günther, K.G., Aufdampfschidhten aus halbleitenden III-V-Verbindungen. *Zeitschrift für Naturforschung A*, **1958**, *13* (12), 1081-1089.

54. Davey, J.E. and Pankey, T., Epitaxial GaAs Films Deposited by Vacuum Evaporation. *Journal of Applied Physics* **1968**, *39* (4), 1941-1948.

55. Greene, J.E., Thin Film Nucleation, Growth, and Microstructural Evolution: An Atomic Scale View. In: Handbook of Deposition Technologies for Films and Coatings. *William Andrew Publishing* **2010**, 554-620.

56. Kadhim, N. J., and D. Mukherjee. Rate-Temperature Relation for MBE Growth of GaAs Layers. *International Journal of Electronics Theoretical and Experimental* **1990**, *69* (5),641-645.

57. Shaw, Don W. Influence of Substrate Temperature on GaAs Epitaxial Deposition Rates. *Journal of The Electrochemical Society* **1968**, *115* (4), 405-408.

58. Venables, J., Introduction to surface and thin film processes. *Cambridge University Press* **2000**

59. Heo, H., Sung, J.H., Ahn, J.H., Ghahari, F., Taniguchi, T., Watanabe, K., Kim, P. and Jo, M.H., Frank‐van der Merwe Growth versus Volmer‐Weber Growth in Successive Stacking of a Few‐Layer Bi_2Te_3/Sb_2Te_3 by van der Waals Heteroepitaxy: The Critical Roles of Finite Lattice‐Mismatch with Seed Substrates. *Advanced Electronic Materials*, **2017**, *3* (2), 1600375.

Chapter 2: Large-area Adlayer-free Single-layer Hexagonal Boron Nitride Film Achieved by Controlling Intercalation Growth

2.1 Introduction

Since the isolation of single-layer graphene in 2004 [1], 2D materials have been intensively investigated, resulting in many novel devices that have unparalleled performances [2-6]. Many of these applications require precise control of film thickness. For example, single layer h-BN film may act as perfect encapsulation or insulation for other 2D materials, while multilayer film is used as excellent tunneling barrier or robust field-effect dielectric for tunneling devices and transistors, respectively. Further accurate control of the number of atomic layers in vertical heterostructures also potentially maximizes the performance of the devices based on these structures. However, while progress has been made in the scalable growth on several catalyst metal substrates [7-13], the precise control of its thickness has remained a great challenge. Non-uniform adlayers in h-BN growth are frequently observed, which compromise the uniformity and flatness of films. Thus, understanding of the formation of adlayers can provide insight into the growth of uniform 2D layers. Specifically, single-layer film can be achieved if adlayer growth is eliminated. In contrast, large multilayer film can be achieved if each layer of the adlayer seeds can grow uniformly in the lateral direction.

To date, the growth mechanism of adlayers remains elusive. One proposed mechanism suggests that sequential layers grow on top of existing layers with an assistance of defective nucleation sites [14], while others suggest that sequential layers grow underneath through

intercalation[15] or precipitation [16]. Similar debate exists in graphene growth for a long time. Some propose that sequential graphene layers grown on top originate from multilayer seed [17]. For example, Kidambi *et al*. reported on-top growth mechanisms by using hydrogen etching [15]. On the other hand, Li *et al.* demonstrated that the second layer grows underneath the first layer on Cu foil by carbon isotope labeling [18]. Also in graphene/h-BN heterostructure growth, intercalation growth of graphene under h-BN cover on Ni substrate was directly observed by *in situ* LEEM [19]. On the other hand, direct growth of graphene on exfoliated h-BN was also achieved under an extremely high growth temperature of 1850 °C [20]. Thus, whether sequential layers grow on top or from bottom depends on the growth conditions and techniques used.

2D h-BN layers are synthesized using various methods such as atomic layer deposition (ALD) [21-23], chemical vapor deposition (CVD) [10, 16, 24-28], and molecular beam epitaxy (MBE) [29-36]. Each one has its own merits. For example, the ALD technique can produce h-BN films with relatively high quality at low growth temperature. Low-temperature process is important for some device applications. CVD process usually requires high temperature to decompose gaseous sources, but it is relatively simple, thus perhaps it is the most popular method. As an alternative, MBE is versatile for the synthesis of 2D h-BN due to its great controllability of growth parameters and in situ atomic-layer monitoring technique such as reflection high-energy electron diffraction (RHEED). In our recent paper regarding the MBE growth of 2D h-BN films on carburized Co and Ni substrates, we demonstrated that subsurface carbon interstitials enhance the absorption and diffusion of B and N atoms on the surface for promoting the h-BN growth [37]. Here, we focus on a study of the growth of

h-BN adlayers. We used two different nitrogen sources, namely nitrogen plasma and ammonia to study the influence of hydrogen atoms; used polycrystalline Co, polycrystalline Ni, and single crystalline Ni substrates to study the influence of substrate crystallographic defects; and used different substrate carburization time to study the interstitial carbon effect. The samples were characterized by X-ray photoelectron spectroscopy (XPS), atomic force microscopy (AFM), Raman spectroscopy, scanning electron microscopy (SEM), and transmission electron microscopy (TEM). By optimizing these growth parameters, we achieved the growth of a large-area adlayer-free single-layer h-BN film, and thus this study provides a strategy towards uniform h-BN 2D film growth.

2.2 Experimental details

A Perkin-Elmer MBE system with a background pressure of ~10^{-9} Torr was used for the sample growth. Boron was supplied by a Knudsen effusion cell filled with B_2O_3 powder (Alfa Aesar, 99.999% purity), which is heated up to around 1150 °C. Nitrogen plasma was produced by introducing nitrogen gas (Airgas, 99.9999% purity) through an electron cyclotron resonance (ECR) nitrogen plasma generator. ECR current was set at 60 mA with a power of 228 W. Ammonia (American Gas Group, 99.9995% purity) was introduced independently through another channel. Gas flow rate of each nitrogen source is limited up to 10 sccm by a mass flow controller (MFC), and total gas flow rate is limited up to 15 sccm by the turbo pump ability. Before growth, Co and Ni substrates with a size of 1 cm × 1 cm, a thickness of 0.1 mm, and a purity of 99.995% were mechanically polished, then cleaned with acetone, IPA and diluted hydrochloric acid (10%), and deionized (DI) water.

All samples were grown at a substrate temperature of 900 °C. Without specific notification, the growth on Ni lasts 6 h, and on Co lasts 3 h.

SEM images were acquired using a FEI NNS450 system in secondary electron (SE) imaging mode with a beam voltage of 10 kV. Raman characterizations were performed using a HORIBA LabRam system equipped with a 60-mW, 532-nm green laser. AFM images were obtained using a Veeco D5000 AFM system. TEM images and selected area electron diffraction (SAED) patterns were acquired using a FEI Tecnai12 system. TEM sample was prepared by picking a transferred h-BN film using a 200-mesh Cu grid covered with holey carbon film with orthogonal array of 1.2-μm diameter holes. XPS characterization was conducted using a Kratos AXIS ULTRA XPS system equipped with an Al Kα monochromatic X-ray source and a 165-mm mean radius electron energy hemispherical analyzer. The fitting of XPS data was performed using CasaXPS software.

2.3 Results and Discussion

2.3.1 Summary of growth results with adlayers

We performed experiments based on three major growth factors, namely hydrogen, substrate type, and substrate carburization level. Figure 2.1 shows the characterization of substrates. The substrates were polished, cleaned, and then annealed at 900 °C in hydrogen environment for 3 h. Fig. 2.1 a/b show optical microscope images of Co and Ni, respectively. Co substrate is much rougher than Ni substrate due to the formation of twins, slip bands, and large triangular and trapezoidal terraces, which may be formed during the special phase transformation between HCP and FCC phases [38]. More detailed surface

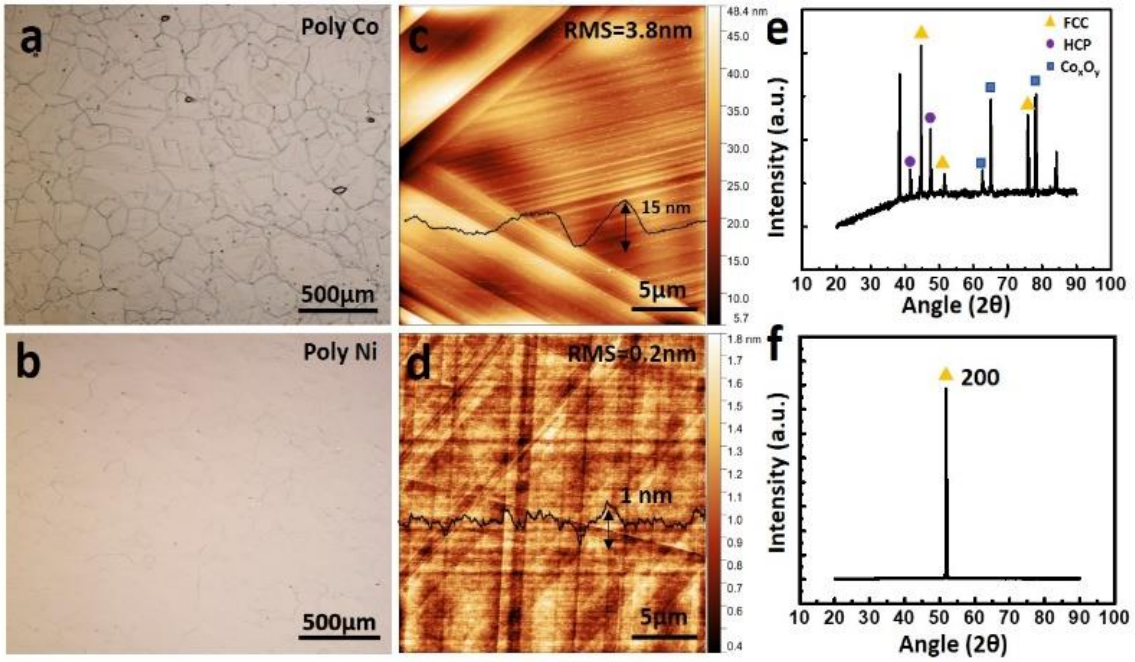

Fig. 2.1. Characterization of polycrystalline Co and Ni substrates. (a/b) Optical microscope images, (c/d) AFM images, and (e/f) XRD results of Co and Ni substrates, respectively; The substrates were polished and annealed in hydrogen environment at 900 °C for 3 h.

morphology was revealed by the AFM images in Fig. 2.1 c/d for Co and Ni, respectively. The formation of terrace on Co substrate results in large steps and slopes, which are about 15 nm in height. On the other hand, Ni surface is much flatter and smoother, as indicated by root mean square (RMS) roughness (3.8 nm for Co vs 0.2 nm for Ni). Fig. 2.1 e/f show XRD results of Co and Ni substrates, respectively. Multiple peaks appear for Co substrate. Besides FCC (111), (200), (220) peaks at 44.55°, 51.49°, 75.88°, respectively, there are also HCP peaks at 41.60° and 47.50°, and Co_xO_y peaks at 62.54°, 65.06°, and 78.10°. Ni substrate only gives a dominant FCC (100) peak around 51.87°, indicating that Ni substrate has better crystallographic uniformity. Overall, there are more crystallographic defects on polycrystalline Co substrate than on polycrystalline Ni substrate.

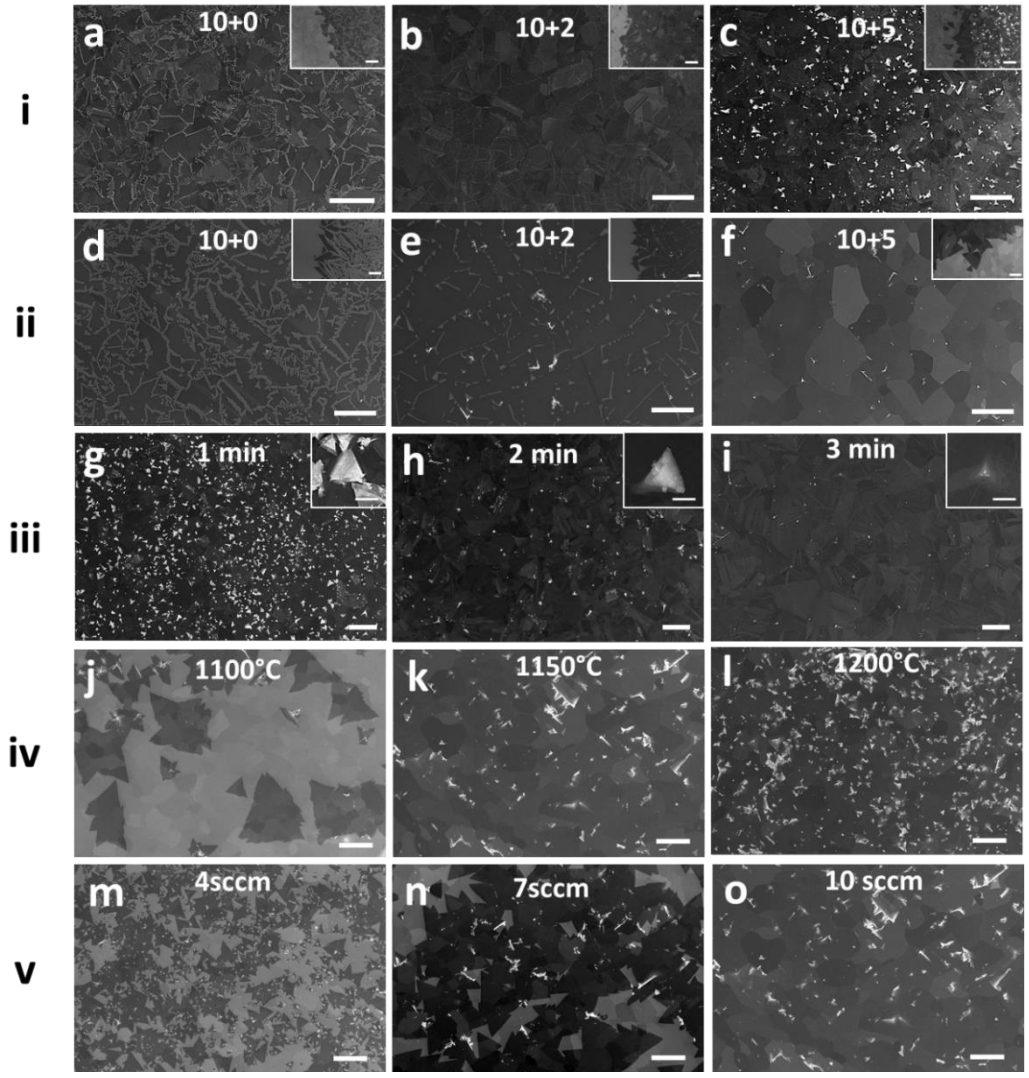

Figure 2.2. SEM images for morphology evolution of h-BN at different growth condition. (i) and (ii) are samples grown with different "N_2 plasma + ammonia" mixture on Co and Ni, respectively. Insets are SEM images taken near the edge. The numbers on SEM images stand for gas flow rate (sccm). (iii) are samples grown with different carburization time on Co. Insets are close-up of adlayers. The scale bar for insets in (h), (i), and (j) are 50 μm, 25 μm, and 10 μm, respectively. C_2H_2 gas flow rate used for carburization is also 0.5 sccm, and the nitrogen mixture is 10+5. (iv) are samples grown with different boron source temperature on Ni with 10 sccm ammonia. (v) are samples grown with different gas flow rate of ammonia with boron cell kept 1150 °C. For samples in (i), (ii), (iii), and (iv), the substrates were carburized with 0.5-sccm C_2H_2 for 1 min before growth. All samples were grown with substrate temperature kept at 900 °C. Growth time on Co is 3 h, while growth time on Ni is 6 h. All the scale bars are 200 μm.

Figure 2.2 (i) and (ii) show two rows of SEM images of as grown films using different "N_2 plasma + ammonia" mixture, respectively. The numbers on the SEM images stand for the gas flow rates (sccm) of N_2 plasma and ammonia, respectively. While the samples in Figure 2.2 (i) were grown on polycrystalline Co, those in Figure 2.2 (ii) were grown on polycrystalline Ni. Thin h-BN film appears to be darker than bare metal surface due to the attenuation effect, while thick h-BN adlayers appear to be bright due to charging effect [39]. Before growth, the substrates were annealed at 900 °C in hydrogen environment for 20 min to remove native oxide layers, then carburized with 0.5-sccm C_2H_2 for 1 min to promote the adsorption and diffusion of B and N atoms [37]. Immediately after these substrate treatments, the growth for all h-BN samples took place by introducing B sources from a B_2O_3 effusion cell at 1150 °C and N mixture sources at a substrate temperature of 900 °C. Samples grown on Ni last 6 h, and on Co last 3 h. After the growth, the substrate was cooled to room temperature at a rate of about 10 degree/min. Other growth details are described in the Experimental Details section. Clear h-BN morphology transformation was demonstrated in the images from left to right on both Ni and Co substrates, as more adlayers appear with the increased amount of ammonia. However, there are fewer adlayers on Ni than on Co under the same growth conditions, therefore the h-BN morphology transformation on Ni is less drastic. Figure 2.2 (iii) shows SEM images of films grown on Co with different carburization time. For this batch of samples, the nitrogen source of "10+5" mixture was used. As shown in Figure 2.2 (iii), while continuous 2D h-BN films have been formed in all samples, introducing more carbon into Co results in fewer adlayers. Similar change of the adlayer density with the level of carburization is also observed for

the samples grown using shorter growth duration of 1h [37]. With the same carburization, nitrogen and boron source flux rates also have influence on the growth of adlayers. Figure 2.2 (iv) shows SEM images of samples grown with different B_2O_3 effusion cell temperature and the same 10-sccm ammonia. Figure 2.2 (v) shows SEM images of samples grown with different ammonia flux and the same B_2O_3 effusion cell temperature of 1150 °C. All these samples were grown at 900 °C for 6 h with 1-min carburization of Ni. As can be seen, increasing the source flux rate of either boron or nitrogen results in larger coverage at the same growth duration, which indicates larger growth speed. Meanwhile, adlayers appear in all samples, and their density increases with the increase of source flux rate.

Before discussing how these three factors influence the morphology of adlayers, we briefly discuss how the adlayers may have been formed in our case, namely, whether the adlayers are formed by growing sequential layers from top of or underneath existing layers. In general, growth without metal surface catalysis requires extreme growth conditions, such as high partial pressure (e.g. ambient pressure) [40], high temperature [20, 41, 42], or special technique [43] to overcome the activation barrier, and the resulted films often have low coverage and uniformity [44]. On the other hand, direct growth on transition metal surface can be achieved at much lower temperature with higher coverage due to a reduced activation barrier by catalytic effect. Since the growth temperature we used is very low (900 °C), it is unlikely to trigger the growth of h-BN on top of the non-catalyzing surface. Till now, two growth mechanisms were reported for the growth-from-below scenario, namely, precipitation (or segregation) and intercalation. Precipitation growth refers to the segregation of source atoms from catalyst substrate, which requires a large solubility of

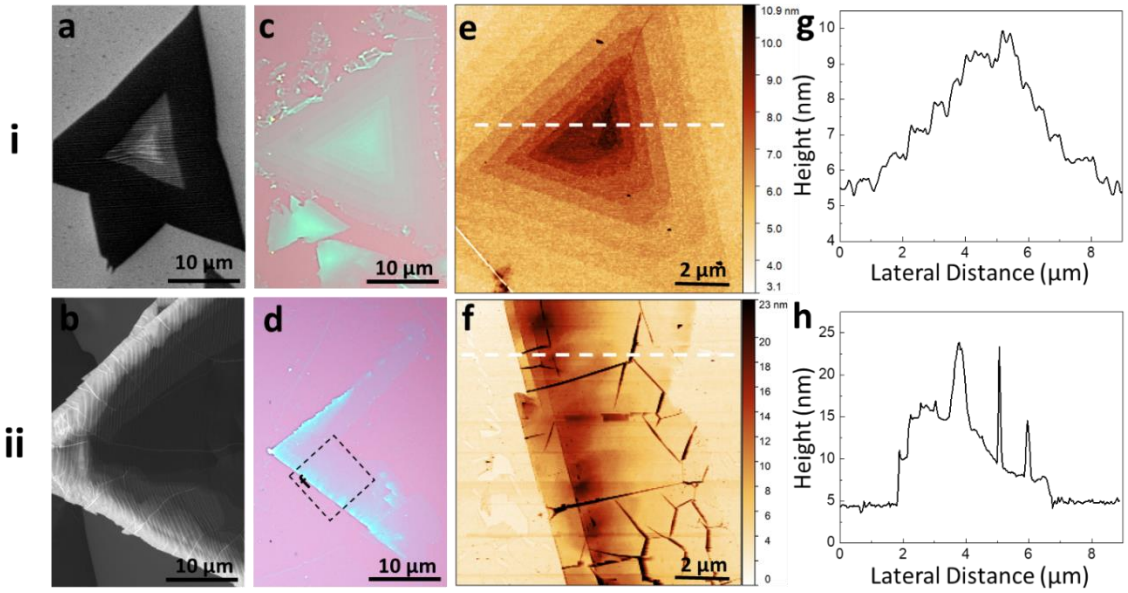

Figure 2.3. Configuration of adlayers with (i) and without (ii) a nucleation site in the center. (a/b) SEM images of adlayers on as grown sample; (c/d) Optical microscope images of adlayers after transferred onto SiO_2/Si substrate; (e/f) AFM images of adlayers after transferred onto SiO_2/Si substrate; (g/h) Height profile taken along white dashed lines in e/f, respectively.

precursor [45-48] and a tendency to form metastable carbide (for graphene growth) [49, 50]. On the other hand, intercalation growth is caused by the diffusion of source atoms into the film/substrate interface, which is reported to be related to edge atom state [51, 52] and interface binding [19]. Although B solubilities in Ni (~0.3 at. % at 1085 °C [53]) and Co (~0.3 at. % at 1110 °C [54]) are considerably large, N solubilities in these metals are reported to be extremely low (in Ni, ~0.004 at. % at 1550 °C [55]; in Co, ~0.017 at. % at 1600 °C [56]). Thus, those adlayers should be most probably formed by intercalation, instead of precipitation.

Since adlayers are formed from below, the growth of adlayers can be influenced mainly by two processes: one is the nucleation process; the other is the intercalation process. The growth of adlayers requires both a nucleation site to start the growth and a path for source

supply in the interface. We first discuss how the nucleation process influences the adlayer growth. The detailed structures of adlayers are shown in Figure 2.3. Two kinds of adlayers are observed. Figure 2.3(i) shows the configuration of "prism-adlayers" with a preferential nucleation site in the center, and Figure 2.3(ii) shows the configuration of "ribbon-adlayers" with preferential nucleation sites along the edges. The SEM images shown in Figure 2.3 a/b are taken on as grown samples, with brighter area corresponding to thicker area. Figure 2.3 c/d show optical microscope images of the transferred adlayers on SiO_2/Si, indicating clear thickness distribution. On "prism-adlayers", a defective nucleation site is always found in the center, as resolved by the AFM image in Figure 2.3e. The line profile in Figure 2.3g, which was taken across the adlayer further shows the protrusion in the center and h-BN steps around it. The narrow peaks are caused by wrinkles on h-BN. On the other hand, no discernable nucleation site is observed on "ribbon-adlayers", as shown in the AFM image of Figure 2.3f. The line profile in Figure 2.3h shows the decreased thickness towards the center of the flake (right hand side).

The "prism-adlayers" may originate from crystallographic defects and impurities on substrate surface, where the high surface energy is beneficial to h-BN nucleation process [14]. Multilayer seeds might form at the beginning of the growth, however, the upper layers with outer edges receive more resources than inner layers, which results in different lateral growth speeds, leading to the formation of prism-like structures. The inner layer will stop growth once it is too far away from the outmost edges, or the outmost edges merge with other flakes, which stops the intercalation process. On the other hand, the "ribbon-adlayers" are likely formed during the h-BN flake expansion. The specific reason of this kind of

adlayer growth is not clear, nevertheless, it may be related to the changes of atom arrangement on substrate surface. As h-BN edges reach those regions with different atom arrangement during growth, mismatch is formed due to the loss of epitaxial relationship between h-BN film and substrate. The mismatch results in weaker binding areas where more intercalation happens [19]. B and N sources intercalate and accumulate in the confined interface, and subsequently nucleate to form atom rings and clusters, which later grow into extra layers. Similar nucleation process was reported in graphene growth [57].

2.3.2 Influence of substrate morphology

As seen from Figure 2.2, even though these two kinds of adlayers coexist on every sample with adlayers, "prism-adlayers" are dominant on Co substrate, while "ribbon-adlayers" dominate on Ni surface. Co and Ni are quite similar in terms of their catalytic effect [58] and B/N solubilities. However, their surface morphology is quite different after heat treatment (Figure 2.1). More crystallographic defects (twin boundaries, terraces, large steps, etc.) form on Co surface than on Ni surface, which may be related to the special phase transformation of Co between HCP and FCC phases [38]. This observation further confirms that "prism-adlayers" are related to crystallographic defects and impurities. Meanwhile, more adlayers are formed on polycrystalline Co substrate than on polycrystalline Ni substrate at the same growth condition, which may be due to the formation of more multilayer seeds on Co.

Figure 2.4 shows SEM images of a sample, which was grown using the same growth conditions as the sample shown in Figure 2.2k or 2.2o, further revealing different adlayer

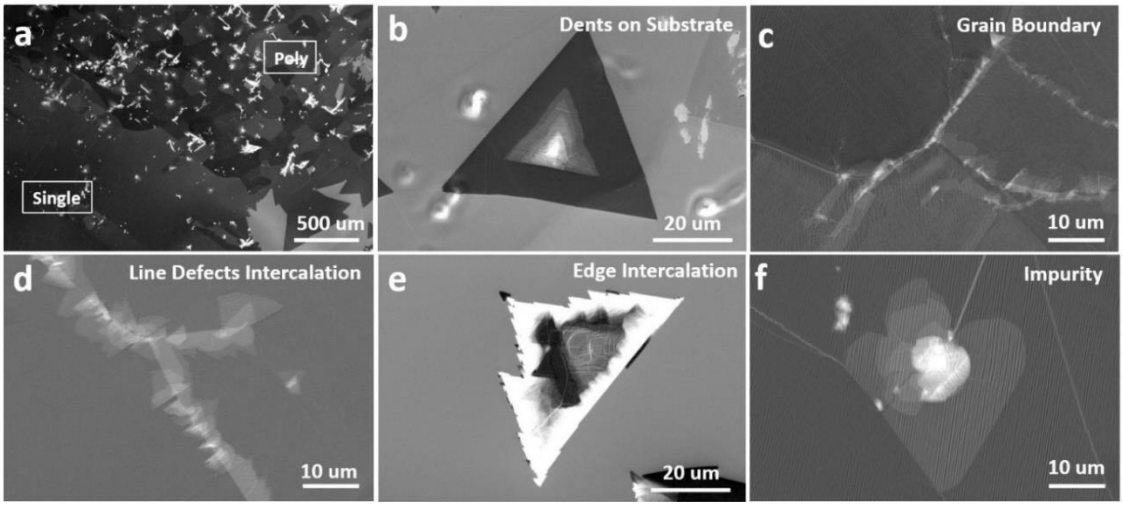

Figure 2.4. SEM images of h-BN adlayers. (a) h-BN grown on Ni with polycrystalline region (upper right) and single crystalline region (lower left); (b) close-up of adlayer grown around dents on substrate surface; (c) close-up of adlayer grown along substrate grain boundary; (d) close-up of adlayer grown along h-BN line defects; (e) close-up of adlayer grown near h-BN flake edges; (e) close-up of h-BN adlayer grown around impurity.

growth scenarios. As shown in Figure 2.4a, more adlayers appear on polycrystalline region (upper right) than on single crystalline region (lower left), which illustrates the strong influence of crystallographic defects in adlayer growth. Figure 2.4 b/c are adlayers grown around dents and grooves (grain boundaries) on substrate surface. Except for the adlayers directly caused by crystallographic defects, some adlayers are formed due to the intercalation near edges, such as line defects (Figure 2.4d) and edges of flakes (Figure 2.4e). The existence of small amount of adlayers on single crystalline region is mainly caused by impurities, as shown in Figure 2.4f.

2.3.3 Influence of nitrogen source

During the growth, N precursor is provided from two sources, namely, N_2 plasma and ammonia. While N_2 plasma is atomic source, ammonia can be regarded as molecular

source. The N_2 plasma generated by ECR plasma generator consists of N_2, N_2*, N_2+, N+, N, and e-, among which only N+ (neutralizes once reaching the grounded substrate surface) and N can bond with B atom and contribute to h-BN growth. On the other hand, ammonia undergo stepwise dehydrogenation on hot metal surface, which results in NH_2, NH radicals, and N and H atoms [59]. By using different mixture of N_2 plasma and ammonia, we observed the h-BN morphology transformation from smooth sub-monolayer to non-uniform multilayer growth. As shown in Figure 2.2 (i) and (ii), when pure N_2 plasma was used as N source (Figure 2.2 a/d), as grown h-BN film is uniform without any adlayers. However, dendritic gaps (1 μm to 8 μm wide) are formed between adjacent h-BN flakes all over the

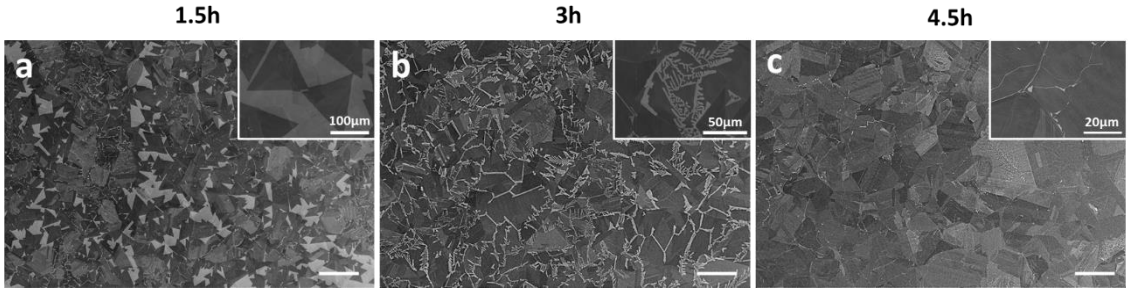

Fig. 2.5. SEM images of time dependent growth of h-BN on Co substrates with 10 sccm N_2 plasma. (a) 1.5h; (b) 3h; (c) 4.5h.

surface. Fig. 2.5 shows SEM images of samples grown with nitrogen plasma on Co under different growth time. Dendritic edge has been widely reported in graphene growth, which is believed to originate from the competition between adatom diffusion along island edges and adatom surface diffusion [60]. When surface diffusion is much faster, edge atoms cannot relax efficiently to find energetically more favorable locations along island edges before additional adatoms migrate by surface diffusion to join them, resulting in dendritic edges. However, our time dependent growth shows that isolated flakes are in well-defined triangle

shape with straight edges (Figure 2.5a), which indicates fast edge atom diffusion rate. Only when those edges of adjacent flakes approach closer, twig-like gaps are formed. The resistance to merge may be related to the bombardment effect of N_2 plasma. According to ECR plasma studies, N_2+ and N+ ions have kinetic energy ranging from 6 eV to 30 eV due to the so-called Sheath potential, which is resulted from ambipolar diffusion of ions and electrons [61]. Ions with this kinetic energy have been used for poly-Si etching, and are able to damage GaN epilayer [62].

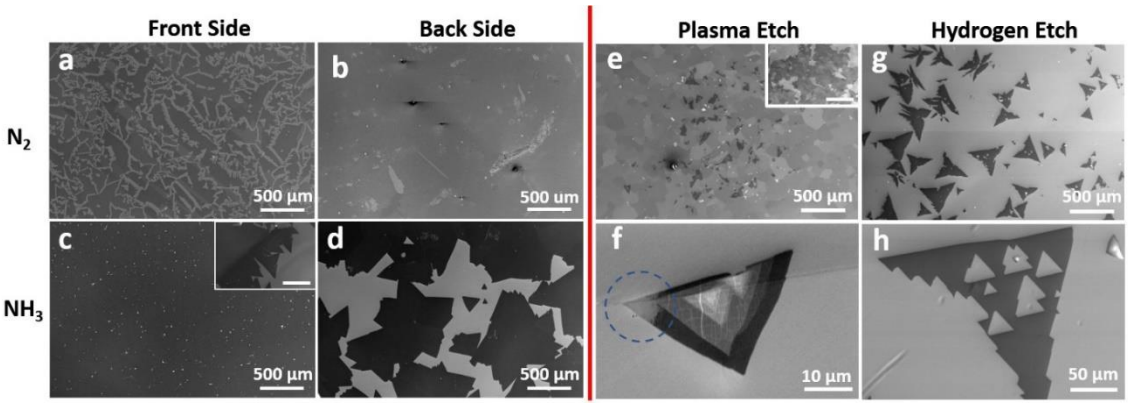

Fig. 2.6. SEM images of as grown h-BN on Ni substrates. (a/b) Front and back side of as grown sample using 10-sccm nitrogen plasma; (c/d) front and back side of as grown sample using 10-sccm ammonia; the scale bar of inset image in (c) is 500 µm; (e) front side of 5-min-plasma-etched sample grown with 10+5 mixture; the inset shows backside of the sample with a scale bar of 500 µm; (f) close-up of an h-BN flake in (e); (g) 5-min-hydrogen-etched sample grown with 10+5 mixture; (h) close-up of an h-BN flake in (g). All samples were grown at 900 °C with 1-min carburization, and the B_2O_3 effusion cell kept at 1150 °C.

To demonstrate the bombardment effect of N_2 plasma clearly, we designed the contrast experiment shown in Figure 2.6. In order to eliminate changes of any other variable, we grow h-BN on both side of substrate, and bombard only one side, then compare the results on frontside and backside. This cannot be done without taking advantage of ammonia's

ability to grow on backside of the substrate, so we highlighted this unique phenomenon of ammonia by comparing the growth results to N_2 plasma in Figure 2.6 a/b/c/d. As seen from the images, when N_2 plasma is used, the front side is covered with h-BN domains, while no growth is observed on the back side of the substrate. When ammonia is used, the front side of the substrate is fully covered by h-BN film, while on the back side, there is also some growth. The difference is caused by the different property of N_2 plasma and ammonia gas. First of all, different to N atoms, B atoms with relatively large solubility can reach the back side of the substrate by bulk diffusion. Ammonia as gas molecules in everywhere of the chamber can reach and decompose on the back side of the substrate and contribute to the h-BN growth. However, N_2 plasma, which is a collimated beam source, cannot reach the backside of the substrate due to the block of substrate holder, leading to no growth on the back side.

Based on the above phenomenon, we did the N_2 plasma etching experiment. We first grew h-BN on both sides of the substrate. The sample was grown on Ni substrate (1-min carburization) using "10+5" mixture for 6 h with B_2O_3 effusion cell kept at 1150 °C. Then we stopped ammonia and boron supply and started cooling while keeping the plasma on for 5 more minutes. The etching is performed during cooling so as to eliminate the influence of thermal decomposition. Figure 2.6e shows the result. While the film on the front side is severely damaged, the film on the back side (Figure 2.6e inset) is still intact. Figure 2.6f is a close-up SEM image of survived flake with one corner etched away.

To further understand this physical bombardment effect, we compared it to the hydrogen chemical etching process. The sample was grown using the same growth recipe. After growth, we stopped all source supply, and introduced 5-sccm hydrogen for 5 minutes during cooling. As shown in Figure 2.6 g/h, etching happened not only on the edge, but also inside the flake. Triangle holes facing the same direction were created, which indicates the anisotropic etching effect. Through this comparison, we conclude that the bombardment etching is isotropic and preferentially affects the edges of the h-BN flakes.

When 2-sccm ammonia was introduced in addition to 10-sccm N_2 plasma, the gaps begin to sew up (Figure 2.2 b, e). Since the growth pressure (2×10^{-4} Torr) did not change much, the alleviation of the plasma's bombardment effect due to mean free path change can be ignored. Instead, the "sewing effect" may be caused by hydrogen. Hydrogen atoms are known to have strong influence in graphene growth. For example, the graphene crystal patterns can be tailored by adjusting CH_4/H_2 ratio [60]; the formation of single and bilayer graphene is closely related to the presence of hydrogen [52], super large single-crystalline graphene domain can be achieved by removing hydrogen atoms on growing edges [63]. Similar to graphene growth, hydrogen atom can also terminate h-BN edge [64, 65]. The presence of hydrogen on h-BN edges can be inferred from the irregular shape of h-BN domains formed when using pure ammonia as N precursor. Figure 2.7 shows the SEM images of time dependent growth of h-BN on Co substrates with 10 sccm ammonia. As can be seen, 1.5-h growth results in irregular shaped h-BN flakes as well as adlayers (Fig. S4d). Doubling the growth time only ends up with larger flakes and more adlayers (Fig. S4e). Prolonging the growth time to 4.5 h leads to a continuous film with adlayers.

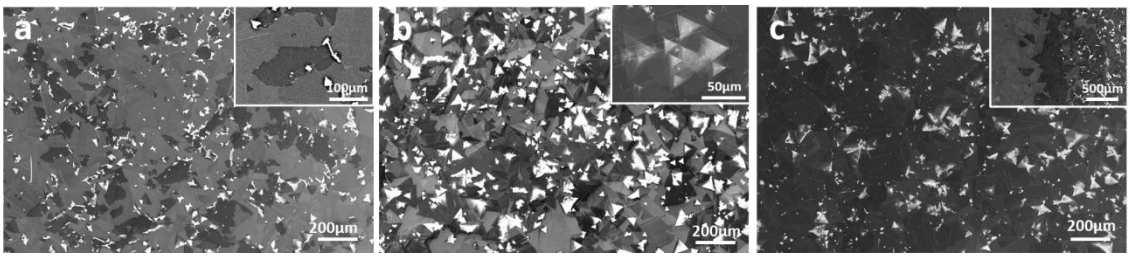

Fig. 2.7. SEM images of time dependent growth of h-BN on Co substrates with 10 sccm ammonia. (a) 1.5h; (b) 3h; (c) 4.5h.

Hydrogen termination results in lower edge atom diffusion rate, thus edge atoms cannot relax sufficiently to find energetically more favorable locations along island edges before additional B/N atoms migrate by surface diffusion to join them. In the absence of such relaxation, irregular edges are formed [66, 67]. The presence of hydrogen atoms on growing edges could have alleviated the plasma's bombardment effect, so as to make the edges easier to merge. On the other hand, the presence of hydrogen on growing edges may also be responsible for the lower lateral growth rate when using ammonia. For the same growth time, using ammonia results in lower coverage than using N_2 plasma (Figure 2.5). Additional activation energies are needed to release hydrogen species from hydrogen terminated edge atoms and/or hydrogen-contained incoming precursors to form h-BN [63], resulting in lower growth rate.

Adlayers were formed when more ammonia was introduced (Figure 2.2c/f). As discussed above, these adlayers should be formed from below by intercalation. In graphene growth, people had reported that hydrogen atoms terminating the growing edges could result in the intercalation growth of adlayers [51, 52]. Here we propose a similar intercalation model, in which the density of B/N atoms in the interface (n_{in}) is proportional to the

penetration probability j_{pnen} (possibility of atoms penetrate through the edge) and the density of B/N atoms outside the edge (n_{out}). j_{pnen} is a factor related to the activeness of h-BN edges, which is determined by the activation energy barrier for h-BN growth. The more active the edges are, the more likely that upcoming atoms get caught and contribute to the lateral growth, thus the less likely these atoms penetrate into the interface. n_{out} is related to source flux rate and adsorption coefficient on catalyst substrate. Larger source flux rate and adsorption coefficient would result in larger n_{out}. By passivating the edges with hydrogen, we actually increase the j_{pnen}, thus more B/N atoms end up in the interface, and in turn, adlayers grow. In a hydrogen-free environment (N_2 plasma as N source), the growing edges with unpaired dangling bonds are very active and readily catch upcoming B and N atoms, thus the j_{pnen} is small, leading to no adlayer growth. It is worth noting that potential use of the mixture of hydrogen and nitrogen gas as N source cannot replace the role of ammonia because pure hydrogen gas strongly etches h-BN (Figure 2.6h).

2.3.4 Influence of carburization

Interstitial carbon embedded in the substrate affects the adlayer growth as well. The amount of interstitial carbon was controlled by the introduction time of C_2H_2 treatment of hot substrates prior to h-BN growth, and longer carburization time led to higher density of interstitial carbon in the substrate, as revealed by XPS studies. Figure 2.8 shows XPS spectra of C_1s on samples with different carburization time as shown in Figure 2.2(iii). As-measured XPS data was first deconvoluted, and fitted with Shirley background and GL(30) line shape. The spectrum was then calibrated by shifting C-C main peak to 284.8

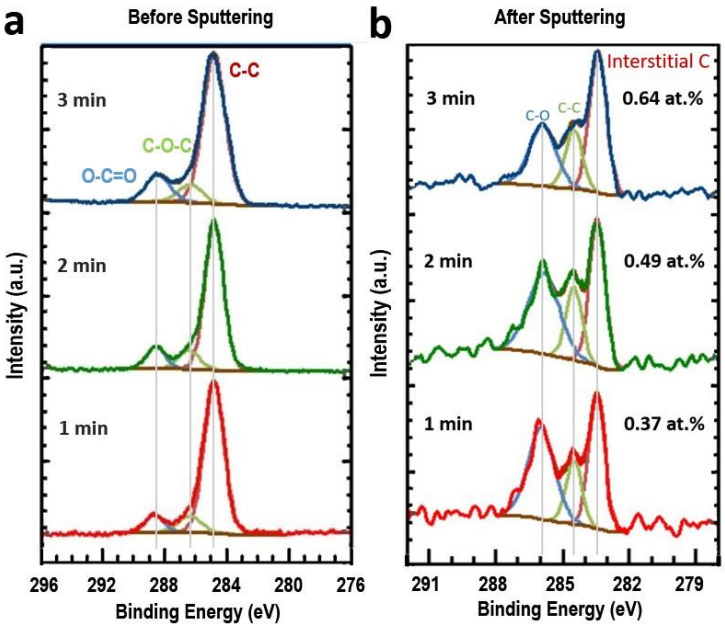

Figure 2.8. XPS characterization of C_1s on samples with 1-min, 2-min, and 3-min carburization. (a) Before sputtering; (b) and after sputtering. As the carburization time increases, the subsurface carbon concentration increases.

eV. As shown in Figure 2.8a, the C_1s signal was dominated by adventitious carbon before sputtering, with C-C/C-H peak at 284.8 eV, C-O-H/C-O-C at 286.3 eV, and O-C=O at 288.5 eV, respectively. Even with different carburization time, no discernable differences were observed before sputtering. Figure 2.8b shows the C_1s peak after 60-s Ar+ ion sputtering. From bottom to up, these are the profiles for 1-min, 2-min, and 3-min carburized samples, respectively. After sputtering, the dissolved interstitial carbon peak at 283.6 eV is resolved [68, 69]. The other two small peaks at 284.8 eV and 286.3 eV are assigned to residual adventitious C-C/C-H and C-O-H/C-O-C carbon, respectively. Precipitated carbon onto grain boundaries may also contribute to the peak at 284.8 eV. No sp^2 C-C bond and Ni-C bond signals are detectable within the limit of the XPS system, suggesting no graphitic or graphene structures have been formed. Based on the depth resolved XPS data,

we calculated the interstitial carbon concentration. It was found that the atomic percentage for 1-min, 2-min, and 3-min carburization is 0.37 at.%, 0.49 at.%, and 0.64 at.%, respectively. However, since the depth resolved XPS data were obtained at room temperature, the real carbon concentration at the growth temperature may be different. According to the first-principles calculation, the subsurface carbon concentration in Ni can be as high as 50 at.% before carbon atoms diffuse deep into the bulk [70], thus the carbon concentration at subsurface during growth should be proportional to carburization time.

As shown in Figure 2.2 (iii), increasing the carburization time suppresses the growth of adlayers. Our previous work indicates that interstitial carbon atoms at the subsurface octahedral sites can enhance the absorption of B and N atoms on Co and Ni substrates and increase the h-BN growth speed [37]. The increased growth speed can be caused by increased source supply (n_{out}), since the absorption of B and N atoms on the surface is enhanced. It may also be caused by improved catalytic activities of the transition metals under the interstitial carbon incorporation, which results in smaller activation energy barrier for the nucleation and growth of h-BN. In other words, h-BN edges are more active in catching upcoming B and N atoms and the growth becomes faster. To elucidate how interstitial carbon exactly works, we campare it to the source flux dependent growth (Figure 2.2(iv) and 2.2(v)), where only n_{out} is changed. As stated earlier, the increase of source flux results in the increase of growth rate. However, the amount of adlayers is also increased. This can be understood based on the intercalation model as discussed above. Since j_{pnen} remains unchanged, the increase in n_{out} results in more B and N atoms in the interface, thus more growth of adlayers. On the other hand, the increase of the amount of interstitial carbon also

results in larger growth speed, however, the amount of adlyers decreases [37]. This suggests that interstitial carbon does not increase h-BN growth rate simply by increasing the abosortion of B/N on the surface (increase of n_{out}). It improves the catalytic effect of the substrate as well. With improved catalytic effect, not only adsorption and diffusion of B and N atoms enhance [37], but also the h-BN edges are much more ready to catch upcoming B/N atoms, therefore j_{pnen} decreases, and fewer B/N atoms end up in the interface.

2.3.5 Adlayer-free monolayer film

So far, we have discussed the factors influencing the growth of h-BN adlayer, including substrate crystallographic defects, hydrogen, and interstitial carbon. While substrate crystallographic defects have strong influence on the nucleation process, hydrogen and interstitial carbon can control the growth of adlayers by engineering the activeness of h-BN edges. Activated edges diminish intercalation growth by decreasing the penetration probability of B/N atoms, while passivated edges promote intercalation growth by increasing the penetration probability of B/N atoms. Considering all these factors, we made an attempt to achieve precise control of the number of layers. First, uniform single-layer film can be obtained by eliminating intercalation growth. To achieve this, single crystalline Ni substrate was chosen in order to diminish the formation of multilayer seeds. A mixture of 10-sccm N_2 plasma and 2-sccm ammonia was used as nitrogen source, in which the 2-sccm ammonia help alleviate plasma bombardment effect and sew the gaps between flakes. 4-min C_2H_2 carburization was used to compensate the effect from the presence of H and

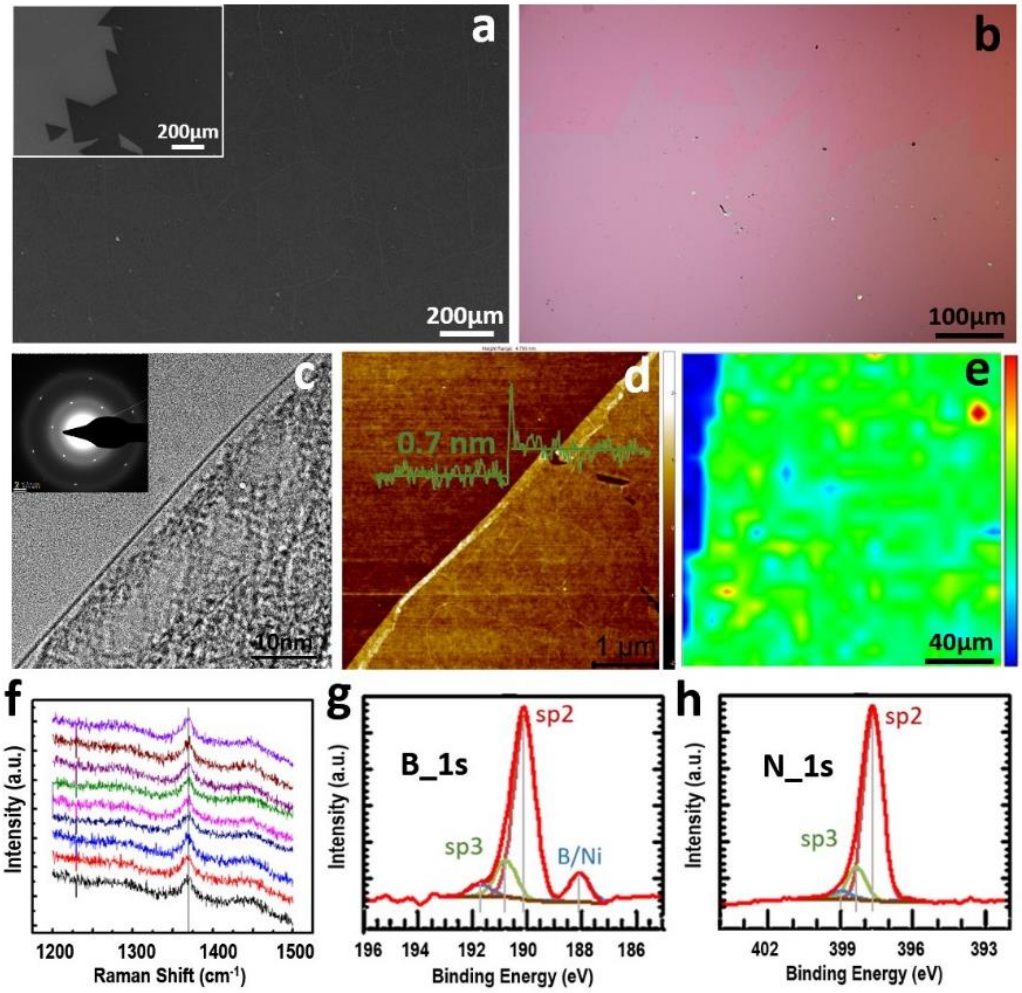

Figure 2.9. Characterization of single-layer h-BN film grown on Ni. (a) SEM image of as grown sample, with the inset showing edge area of film; (b) Optical microscope image of the sample after transferred onto SiO_2/Si substrate; (c) TEM image of the sample after transferred onto TEM grid, with inset showing the SAED pattern; (c) AFM image taken on the transferred sample; (d) Raman mapping of h-BN characteristic peak on the transferred sample; (f) 9 random Raman spectra extracted from (e); (g) XPS spectrum of B_1s; (h) XPS spectrum of N_1s.

keep the h-BN edge active to B and N. The temperature of B_2O_3 effusion cell and substrate were kept at 1150 °C and 900 °C, respectively. The growth time was 6 h. Figure 2.9a shows an SEM image of single-layer film taken at the center of as grown sample, with the inset showing the film edge area. No large adlayers were observed over the 1 cm^2 surface. Figure

2.9b shows an optical microscopy image of the transferred h-BN film on SiO_2/Si substrate. The film was transferred by modified RCA process [71], followed by an annealing at 400 °C in oxygen environment for 3 h to remove water and PMMA residue [72, 73]. The transferred film shows uniform contrast in large area despite of some small contaminations (black and yellow dots), indicating high film quality. The thickness of the single-layer h-BN film was confirmed by TEM as shown in Figure 2.9c. Inserted SAED pattern shows bright spots in hexagonal arrangement, indicating the hexagonal arrangement of B and N atoms. The rings in SAED pattern are formed due to the diffraction of electrons by amorphous holy carbon thin film on TEM grids. The AFM image in Figure 2.9d was taken on transferred film shown in Figure 2.9b. Larger thickness (0.7 nm) compared to theoretical value (0.33 nm) of single-layer film may be caused by different atomic forces between tip/h-BN and tip/SiO_2, weak binding between h-BN film and SiO_2/Si substrate, as well as water and gases intercalated in the interface [14]. Raman mapping was performed on the transferred sample, and the result is shown in Figure 2.9e. The green contrast is corresponding to E_{2g} peak of h-BN. The slight nonuniformity in Raman intensity may be caused by the corrugation of h-BN film formed during transfer process. Figure 2.9f shows Raman spectra extracted from nine different spots of Raman map, and all the peaks are located around 1369.5 cm^{-1}, which implies single-layer h-BN [74]. Figure 2.9 g/h show XPS spectra of B_1s and N_1s signals of as grown single layer h-BN film, respectively. As-measured XPS data was first deconvoluted, and fitted with Shirley background and GL(0) line shape. These spectra were then calibrated by shifting C-C main peak to 284.8 eV. The main peaks of B and N are measured to be 190.1 eV and 397.6 eV, respectively, an indication of sp^2 bonds, which is

consistent with other reports [15, 16]. The smaller peak next to the main peak at higher position, 190.7 (398.2) eV, is assigned to cubic-like sp^3 bond [75, 76]. The neglectable small peak at the highest position, 191.6 (399.5) eV, is assigned to oxygen related defects [77].

2.4 Conclusion

We have carried out a study of intercalation growth of h-BN adlayers. By comparing the growth on different catalyst substrates, we showed that crystallographic defects on catalyst substrates play an important role in adlayer nucleation process. By using N plasma, ammonia, and their mixtures as nitrogen sources, we found that hydrogen played multiple roles in h-BN growth. On one hand, hydrogen terminating growing edges can provide protection against plasma's bombardment effect, making 2D h-BN flakes easier to merge. On the other hand, it passivates h-BN edges, which results in slower lateral growth rate and more intercalation growth of 3D adlayers. We also further revealed an important role played by interstitial carbon in the transition metal substrates, which enhances the substrate catalytic effect. The enhanced catalytic effect not only promotes the adsorption of B and N atoms, but also makes h-BN edges active in catching upcoming B and N atoms, which results in larger growth speed and less intercalation growth of adlayers. By controlling the mixture of atomic N and molecular N sources, we achieved large-area growth of adlayer-free single-layer h-BN film on a carburized single-crystalline Ni substrate. Our research work helps reveal the h-BN adlayer growth mechanism and provides insight towards controllable growth of wafer-scale h-BN 2D films with uniform thickness.

2.5. References

1. Novoselov, K. S.; Geim, A. K.; Morozov, S. V.; Jiang, D.; Zhang, Y.; Dubonos, S. V.; Grigorieva, I. V.; Firsov, A. A., Electric Field Effect in Atomically Thin Carbon Films. *Science* **2004,** *306* (5696), 666-669.

2. Britnell, L.; Gorbachev, R.; Jalil, R.; Belle, B.; Schedin, F.; Mishchenko, A.; Georgiou, T.; Katsnelson, M.; Eaves, L.; Morozov, S., Field-Effect Tunneling Transistor Based on Vertical Graphene Heterostructures. *Science* **2012,** *335* (6071), 947-950.

3. Bao, Q.; Loh, K. P., Graphene Photonics, Plasmonics, and Broadband Optoelectronic Devices. *ACS Nano* **2012,** *6* (5), 3677-3694.

4. Cheng, R.; Li, D.; Zhou, H.; Wang, C.; Yin, A.; Jiang, S.; Liu, Y.; Chen, Y.; Huang, Y.; Duan, X., Electroluminescence and Photocurrent Generation from Atomically Sharp WSe_2/MoS_2 Heterojunction p–n Diodes. *Nano Letters* **2014,** *14* (10), 5590-5597.

5. Withers, F.; Del Pozo-Zamudio, O.; Mishchenko, A.; Rooney, A.; Gholinia, A.; Watanabe, K.; Taniguchi, T.; Haigh, S.; Geim, A.; Tartakovskii, A., Light-Emitting Diodes by Band-Structure Engineering in van der Waals Heterostructures. *Nature Materials* **2015,** *14* (3), 301.

6. Maity, A.; Doan, T.; Li, J.; Lin, J.; Jiang, H., Realization of Highly Efficient Hexagonal Boron Nitride Neutron Detectors. *Applied Physics Letters* **2016,** *109* (7), 072101.

7. Hui, F.; Villena, M. A.; Fang, W.; Lu, A.-Y.; Kong, J.; Shi, Y.; Jing, X.; Zhu, K.; Lanza, M., Synthesis of Large-Area Multilayer Hexagonal Boron Nitride Sheets on Iron Substrates and Its Use in Resistive Switching Devices. *2D Materials* **2018,** *5* (3), 031011.

8. Caneva, S.; Weatherup, R. S.; Bayer, B. C.; Brennan, B.; Spencer, S. J.; Mingard, K.; Cabrero-Vilatela, A.; Baehtz, C.; Pollard, A. J.; Hofmann, S., Nucleation Control for Large, Single Crystalline Domains of Monolayer Hexagonal Boron Nitride via Si-Doped Fe Catalysts. *Nano Letters* **2015,** *15* (3), 1867-1875.

9. Kim, G.; Jang, A.-R.; Jeong, H. Y.; Lee, Z.; Kang, D. J.; Shin, H. S., Growth of High-Crystalline, Single-Layer Hexagonal Boron Nitride on Recyclable Platinum Foil. *Nano Letters* **2013,** *13* (4), 1834-1839.

10. Kim, K. K.; Hsu, A.; Jia, X.; Kim, S. M.; Shi, Y.; Hofmann, M.; Nezich, D.; Rodriguez-Nieva, J. F.; Dresselhaus, M.; Palacios, T., Synthesis of Monolayer Hexagonal Boron Nitride on Cu Foil Using Chemical Vapor Deposition. *Nano Letters* **2011,** *12* (1), 161-166.

11. Meng, J.; Zhang, X.; Wang, Y.; Yin, Z.; Liu, H.; Xia, J.; Wang, H.; You, J.; Jin, P.; Wang, D., Aligned Growth of Millimeter Size Hexagonal Boron Nitride Single Crystal Domains on Epitaxial Nickel Thin Film. *Small* **2017,** *13* (18), 1604179.

12. Ying, H.; Li, X.; Li, D.; Huang, M.; Wan, W.; Yao, Q.; Chen, X.; Wang, Z.; Wu, Y.; Wang, L., Ni Foam Assisted Synthesis of High Quality Hexagonal Boron Nitride With Large Domain Size and Controllable Thickness. *2D Materials* **2018,** *5* (2), 025020.

13. Petrović, M.; Hagemann, U.; Horn-von Hoegen, M.; zu Heringdorf, F.-J. M., Microanalysis of Single-Layer Hexagonal Boron Nitride Islands on Ir (111). *Applied Surface Science* **2017,** *420*, 504-510.

14. Khan, M. H.; Huang, Z.; Xiao, F.; Casillas, G.; Chen, Z.; Molino, P. J.; Liu, H. K., Synthesis of Large and Few Atomic Layers of Hexagonal Boron Nitride on Melted Copper. *Scientific Reports* **2015,** *5*, 7743.

15. Kidambi, P. R.; Blume, R.; Kling, J.; Wagner, J. B.; Baehtz, C.; Weatherup, R. S.; Schloegl, R.; Bayer, B. C.; Hofmann, S., In situ Observations During Chemical Vapor Deposition of Hexagonal Boron Nitride on Polycrystalline Copper. *Chemistry of Materials* **2014,** *26* (22), 6380-6392.

16. Caneva, S.; Weatherup, R. S.; Bayer, B. C.; Blume, R.; Cabrero-Vilatela, A.; Braeuninger-Weimer, P.; Martin, M.-B.; Wang, R.; Baehtz, C.; Schloegl, R., Controlling Catalyst Bulk Reservoir Effects for Monolayer Hexagonal Boron Nitride CVD. *Nano Letters* **2016,** *16* (2), 1250-1261.

17. Robertson, A. W.; Warner, J. H., Hexagonal Single Crystal Domains of Few-Layer Graphene on Copper Foils. *Nano Letters* **2011,** *11* (3), 1182-1189.

18. Li, Q.; Chou, H.; Zhong, J.-H.; Liu, J.-Y.; Dolocan, A.; Zhang, J.; Zhou, Y.; Ruoff, R. S.; Chen, S.; Cai, W., Growth of Adlayer Graphene on Cu Studied by Carbon Isotope Labeling. *Nano Letters* **2013,** *13* (2), 486-490.

19. Yang, Y.; Fu, Q.; Li, H.; Wei, M.; Xiao, J.; Wei, W.; Bao, X., Creating a Nanospace under an h-BN Cover for Adlayer Growth on Nickel (111). *ACS nano* **2015,** *9* (12), 11589-11598.

20. Summerfield, A.; Davies, A.; Cheng, T. S.; Korolkov, V. V.; Cho, Y.; Mellor, C. J.; Foxon, C. T.; Khlobystov, A. N.; Watanabe, K.; Taniguchi, T., Strain-Engineered Graphene Grown on Hexagonal Boron Nitride by Molecular Beam Epitaxy. *Scientific Reports* **2016,** *6*, 22440.

21. Ferguson, J.; Weimer, A.; George, S., Atomic Layer Deposition of Boron Nitride Using Sequential Exposures of BCl_3 and NH_3. *Thin Solid Films* **2002,** *413* (1-2), 16-25.

22. Driver, M. S.; Beatty, J. D.; Olanipekun, O.; Reid, K.; Rath, A.; Voyles, P. M.; Kelber, J. A., Atomic Layer Epitaxy of h-BN (0001) Multilayers on Co (0001) and Molecular Beam Epitaxy Growth of Graphene on h-BN (0001)/Co (0001). *Langmuir* **2016,** *32* (11), 2601-2607.

23. Jones, J.; Beauclair, B.; Olanipekun, O.; Lightbourne, S.; Zhang, M.; Pollok, B.; Pilli, A.; Kelber, J., Atomic Layer Deposition of h-BN (0001) on RuO_2 (110)/Ru (0001).

Journal of Vacuum Science & Technology A: Vacuum, Surfaces, and Films **2017,** *35* (1), 01B139.

24. Shi, Y.; Hamsen, C.; Jia, X.; Kim, K. K.; Reina, A.; Hofmann, M.; Hsu, A. L.; Zhang, K.; Li, H.; Juang, Z.-Y., Synthesis of Few-Layer Hexagonal Boron Nitride Thin Film by Chemical Vapor Deposition. *Nano Letters* **2010,** *10* (10), 4134-4139.

25. Song, L.; Ci, L.; Lu, H.; Sorokin, P. B.; Jin, C.; Ni, J.; Kvashnin, A. G.; Kvashnin, D. G.; Lou, J.; Yakobson, B. I., Large Scale Growth and Characterization of Atomic Hexagonal Boron Nitride Layers. *Nano Letters* **2010,** *10* (8), 3209-3215.

26. Ismach, A.; Chou, H.; Mende, P.; Dolocan, A.; Addou, R.; Aloni, S.; Wallace, R.; Feenstra, R.; Ruoff, R. S.; Colombo, L., Carbon-Assisted Chemical Vapor Deposition of Hexagonal Boron Nitride. *2D Materials* **2017,** *4* (2), 025117.

27. Petrović, M.; Horn-von Hoegen, M.; zu Heringdorf, F.-J. M., Lateral Heterostructures of Hexagonal Boron Nitride and Graphene: BCN Alloy Formation and Microstructuring Mechanism. *Applied Surface Science* **2018,** *455*, 1086-1094.

28. Song, Y.; Zhang, C.; Li, B.; Jiang, D.; Ding, G.; Wang, H.; Xie, X., Triggering the Atomic Layers Control of Hexagonal Boron Nitride Films. *Applied Surface Science* **2014,** *313*, 647-653.

29. Nakhaie, S.; Wofford, J.; Schumann, T.; Jahn, U.; Ramsteiner, M.; Hanke, M.; Lopes, J.; Riechert, H., Synthesis of Atomically Thin Hexagonal Boron Nitride Films on Nickel Foils by Molecular Beam Epitaxy. *Applied Physics Letters* **2015,** *106* (21), 213108.

30. Tsai, C.; Kobayashi, Y.; Akasaka, T.; Kasu, M., Molecular Beam Epitaxial Growth of Hexagonal Boron Nitride on Ni (1 1 1) Substrate. *Journal of Crystal Growth* **2009,** *311* (10), 3054-3057.

31. Zuo, Z.; Xu, Z.; Zheng, R.; Khanaki, A.; Zheng, J.-G.; Liu, J., In-situ Epitaxial Growth of Graphene/h-BN van der Waals Heterostructures by Molecular Beam Epitaxy. *Scientific Reports* **2015,** *5*, 14760.

32. Vuong, T.; Cassabois, G.; Valvin, P.; Rousseau, E.; Summerfield, A.; Mellor, C.; Cho, Y.; Cheng, T.; Albar, J. D.; Eaves, L., Deep Ultraviolet Emission in Hexagonal Boron Nitride Grown by High-Temperature Molecular Beam Epitaxy. *2D Materials* **2017,** *4* (2), 021023.

33. Heilmann, M.; Bashouti, M.; Riechert, H.; Lopes, J., Defect Mediated van der Waals Epitaxy of Hexagonal Boron Nitride on Graphene. *2D Materials* **2018,** *5* (2), 025004.

34. Khanaki, A.; Tian, H.; Xu, Z.; Zheng, R.; He, Y.; Cui, Z.; Yang, J.; Liu, J., Effect of High Carbon Incorporation in Co Substrates on the Epitaxy of Hexagonal Boron Nitride/Graphene Heterostructures. *Nanotechnology* **2017,** *29* (3), 035602.

35. Summerfield, A.; Kozikov, A.; Cheng, T. S.; Davies, A.; Cho, Y.-J.; Khlobystov, A. N.; Mellor, C. J.; Foxon, C. T.; Watanabe, K.; Taniguchi, T., Moiré-Modulated Conductance of Hexagonal Boron Nitride Tunnel Barriers. *Nano Letters* **2018,** *18* (7), 4241-4246.

36. Cho, Y.-J.; Summerfield, A.; Davies, A.; Cheng, T. S.; Smith, E. F.; Mellor, C. J.; Khlobystov, A. N.; Foxon, C. T.; Eaves, L.; Beton, P. H., Hexagonal Boron Nitride Tunnel Barriers Grown on Graphite by High Temperature Molecular Beam Epitaxy. *Scientific Reports* **2016,** *6*, 34474.

37. Tian, H.; Khanaki, A.; Das, P.; Zheng, R.; Cui, Z.; He, Y.; Shi, W.; Xu, Z.; Lake, R.; Liu, J., Role of Carbon Interstitials in Transition Metal Substrates on Controllable Synthesis of High-Quality Large-Area Two-Dimensional Hexagonal Boron Nitride Layers. *Nano Letters* **2018,** *18* (6), 3352-3361.

38. Xie, Z.; Ni, S.; Song, M., Effect of Y_2O_3 Doping on FCC to HCP Phase Transformation in Cobalt Produced by Ball Milling and Spark Plasma Sintering. *Powder Technology* **2018,** *324*, 1-4.

39. Sutter, P.; Sutter, E., Thickness Determination of Few-Layer Hexagonal Boron Nitride Films by Scanning Electron Microscopy and Auger Electron Spectroscopy. *APL Materials* **2014,** *2* (9), 092502.

40. Tai, L.; Zhu, D.; Liu, X.; Yang, T.; Wang, L.; Wang, R.; Jiang, S.; Chen, Z.; Xu, Z.; Li, X., Direct Growth of Graphene on Silicon by Metal-Free Chemical Vapor Deposition. *Nano-Micro Letters* **2018,** *10* (2), 20.

41. Chugh, D.; Wong-Leung, J.; Li, L.; Lysevych, M.; Tan, H.; Jagadish, C., Flow Modulation Epitaxy of Hexagonal Boron Nitride. *2D Materials* **2018,** *5* (4), 045018.

42. Entani, S.; Takizawa, M.; Li, S.; Naramoto, H.; Sakai, S., Growth of Graphene on SiO_2 with Hexagonal Boron Nitride Buffer Layer. *Applied Surface Science* **2019,** *475*, 6-11.

43. Wang, Z.; Xue, Z.; Zhang, M.; Wang, Y.; Xie, X.; Chu, P. K.; Zhou, P.; Di, Z.; Wang, X., Germanium Assisted Direct Growth of Graphene on Arbitrary Dielectric Substrates for Heating Devices. S*mall* **2017,** *13* (28).

44. Chen, X.; Wu, B.; Liu, Y., Direct Preparation of High Quality Graphene on Dielectric Substrates. *Chemical Society Reviews* **2016,** *45* (8), 2057-2074.

45. Sutter, P. W.; Flege, J.-I.; Sutter, E. A., Epitaxial Graphene on Ruthenium. *Nature Materials* **2008,** *7* (5), 406.

46. Reina, A.; Jia, X.; Ho, J.; Nezich, D.; Son, H.; Bulovic, V.; Dresselhaus, M. S.; Kong, J., Large area, Few-Layer Graphene Films on Arbitrary Substrates by Chemical Vapor Deposition. *Nano Letters* **2008,** *9* (1), 30-35.

47. Reina, A.; Thiele, S.; Jia, X.; Bhaviripudi, S.; Dresselhaus, M. S.; Schaefer, J. A.; Kong, J., Growth of Large-Area Single-and Bi-Layer Graphene by Controlled Carbon Precipitation on Polycrystalline Ni Surfaces. *Nano Research* **2009,** *2* (6), 509-516.

48. Lahiri, J.; Miller, T. S.; Ross, A. J.; Adamska, L.; Oleynik, I. I.; Batzill, M., Graphene Growth and Stability at Nickel Surfaces. *New Journal of Physics* **2011,** *13* (2), 025001.

49. Zou, Z.; Fu, L.; Song, X.; Zhang, Y.; Liu, Z., Carbide-Forming Groups IVB-VIB Metals: a New Territory in the Periodic Table for CVD Growth of Graphene. *Nano Letters* **2014,** *14* (7), 3832-3839.

50. Fang, W.; Hsu, A. L.; Song, Y.; Kong, J., A review of Large-Area Bilayer Graphene Synthesis by Chemical Vapor Deposition. *Nanoscale* **2015,** *7* (48), 20335-20351.

51. Zhang, X. Y.; Wang, L.; Xin, J.; Yakobson, B. I.; Ding, F., Role of Hydrogen in Graphene Chemical Vapor Deposition Growth on a Copper Surface. *J Am Chem Soc* **2014,** *136* (8), 3040-3047.

52. Li, Y.; Wu, B.; Guo, W.; Wang, L.; Li, J.; Liu, Y., Tailoring Graphene Layer-to-Layer Growth. *Nanotechnology* **2017,** *28* (26), 265101.

53. Yang, P.; Prater, J.; Liu, W.; Glass, J.; Davis, R., The Formation of Epitaxial Hexagonal Boron Nitride on Nickel Substrates. *Journal of Electronic Materials* **2005,** *34* (12), 1558-1564.

54. Massalski, T. B., Binally Alloy Phase Diagrams. *American Society for Metals* **1986**.

55. Abdulrahman, R.; Hendry, A., Solubility of Nitrogen in Liquid Nickel-Based Alloys. *Metallurgical and Materials Transactions B* **2001,** *32* (6), 1103-1112.

56. KOJIMA, Y.; YAMADA, Y.; INOUYE, M., The Solubilities and Diffusion Coefficients of Nitrogen in the Liquid Iron-Nickel and Iron-Cobalt Alloys at 1600° C. *Tetsu-to-Hagane* **1975,** *61* (2), 195-201.

57. Loginova, E.; Bartelt, N. C.; Feibelman, P. J.; McCarty, K. F., Evidence for Graphene Growth by C Cluster Attachment. *New Journal of Physics* **2008,** *10* (9), 093026.

58. Ganley, J. C.; Thomas, F.; Seebauer, E.; Masel, R. I., A Priori Catalytic Activity Correlations: the Difficult Case of Hydrogen Production from Ammonia. *Catalysis Letters* **2004,** *96* (3-4), 117-122.

59. Rasim, K.; Bobeth, M.; Pompe, W.; Seriani, N., A Microkinetic Model of Ammonia Decomposition on a Pt Overlayer on Au (1 1 1). *Journal of Molecular Catalysis A: Chemical* **2010,** *325* (1-2), 15-24.

60. Wu, B.; Geng, D.; Xu, Z.; Guo, Y.; Huang, L.; Xue, Y.; Chen, J.; Yu, G.; Liu, Y., Self-Organized Graphene Crystal Patterns. *NPG Asia Materials* **2012,** *4* (1), e36.

61. Fan, Z.; Newman, N., Kinetic Energy Distribution of Nitrogen Ions in an Electron Cyclotron Resonance Plasma. *Journal of Vacuum Science & Technology A: Vacuum, Surfaces, and Films* **1998,** *16* (4), 2132-2139.

62. Fu, T.; Newman, N.; Jones, E.; Chan, J.; Liu, X.; Rubin, M.; Cheung, N.; Weber, E., The Influence of Nitrogen Ion energy on the Quality of GaN Films Grown with Molecular Beam Epitaxy. *Journal of Electronic Materials* **1995,** *24* (4), 249-255.

63. Hao, Y.; Bharathi, M.; Wang, L.; Liu, Y.; Chen, H.; Nie, S.; Wang, X.; Chou, H.; Tan, C.; Fallahazad, B., The Role of Surface Oxygen in the Growth of Large Single-Crystal Graphene on Copper. *Science* **2013**, 1243879.

64. Stehle, Y. Y.; Sang, X.; Unocic, R. R.; Voylov, D.; Jackson, R. K.; Smirnov, S.; Vlassiouk, I., Anisotropic Etching of Hexagonal Boron Nitride and Graphene: Question of Edge Terminations. *Nano Letters* **2017,** *17* (12), 7306-7314.

65. McDougall, N. L.; Partridge, J. G.; Nicholls, R. J.; Russo, S. P.; McCulloch, D. G., Influence of Point Defects on the Near Edge Structure of Hexagonal Boron Nitride. *Physical Review B* **2017,** *96* (14), 144106.

66. Saito, Y., Statistical Physics of Crystal Growth. *World Scientific* **1996**.

67. Zhang, Z.; Lagally, M. G., Atomistic Processes in the Early Stages of Thin-Film Growth. *Science* **1997,** *276* (5311), 377-383.

68. Weatherup, R. S.; Bayer, B. C.; Blume, R.; Ducati, C.; Baehtz, C.; Schlogl, R.; Hofmann, S., In situ Characterization of Alloy Catalysts for Low-Temperature Graphene Growth. *Nano Letters* **2011,** *11* (10), 4154-4160.

69. Bayer, B. C.; Bosworth, D. A.; Michaelis, F. B.; Blume, R.; Habler, G.; Abart, R.; Weatherup, R. S.; Kidambi, P. R.; Baumberg, J. J.; Knop-Gericke, A., In situ Observations of Phase Transitions in Metastable Nickel (Carbide)/Carbon Nanocomposites. *The Journal of Physical Chemistry C* **2016,** *120* (39), 22571-22584.

70. Xu, J.; Saeys, M., First Principles Study of the Stability and the Formation Kinetics of Subsurface and Bulk Carbon on a Ni Catalyst. *The Journal of Physical Chemistry C* **2008,** *112* (26), 9679-9685.

71. Liang, X.; Sperling, B. A.; Calizo, I.; Cheng, G.; Hacker, C. A.; Zhang, Q.; Obeng, Y.; Yan, K.; Peng, H.; Li, Q., Toward Clean and Crackless Transfer of Graphene. *ACS Nano* **2011,** *5* (11), 9144-9153.

72. Li, L. H.; Cervenka, J.; Watanabe, K.; Taniguchi, T.; Chen, Y., Strong Oxidation Resistance of Atomically Thin Boron Nitride Nanosheets. *ACS Nano* **2014,** *8* (2), 1457-1462.

73. Gong, C.; Floresca, H. C.; Hinojos, D.; McDonnell, S.; Qin, X.; Hao, Y.; Jandhyala, S.; Mordi, G.; Kim, J.; Colombo, L., Rapid Selective Etching of PMMA Residues from

Transferred Graphene by Carbon Dioxide. *The Journal of Physical Chemistry C* **2013,** *117* (44), 23000-23008.

74. Arenal, R.; Ferrari, A.; Reich, S.; Wirtz, L.; Mevellec, J.-Y.; Lefrant, S.; Rubio, A.; Loiseau, A., Raman Spectroscopy of Single-Wall Boron Nitride Nanotubes. *Nano Letters* **2006,** *6* (8), 1812-1816.

75. Deng, J.; Chen, G.; Song, X., Characterization of Cubic Boron Nitride Thin Films Deposited by RF Sputter. *International Journal of Modern Physics B* **2002,** *16* (28n29), 4339-4342.

76. Mirkarimi, P.; McCarty, K.; Medlin, D., Review of Advances in Cubic Boron Nitride Film Synthesis. *Materials Science and Engineering: R: Reports* **1997,** *21* (2), 47-100.

77. Sediri, H.; Pierucci, D.; Hajlaoui, M.; Henck, H.; Patriarche, G.; Dappe, Y. J.; Yuan, S.; Toury, B.; Belkhou, R.; Silly, M. G., Atomically Sharp Interface in an h-BN-Epitaxial Graphene van der Waals Heterostructure. *Scientific Reports* **2015,** *5*, 16465.

Chapter 3: Growth of High-quality Hexagonal Boron Nitride Single-layer Films on Carburized Ni Substrates for Metal-Insulator-Metal Tunneling Devices

3.1 Introduction

The recent booming of two-dimensional (2D) materials has paved the way for the next generation of quantum electrical devices. For example, graphene with high electrical conductivity has been used as electrodes in nanodevices based on van der Waals materials such as capacitors [1]; 2D transition metal dichalcogenides (TMD) semiconductors such as MoS_2 are often used as the channel in field-effect transistors [2-3] and photodetectors [4]. 2D hexagonal boron nitride (h-BN) is a layered material isostructural to graphene. The replacement of carbon with alternating boron and nitrogen in the honeycomb-like sp^2 network creates an utterly different material with a wide band gap (5.9 eV) [5], high breakdown electric field [6], high thermal conductivity [7], and chemical inertness [8]. Due to these properties, h-BN has been used as insulating layer in transistors [9] and capacitors [10], resistive switching layer for memristors [11-12], anti-scattering substrate for graphene and MoS_2 based devices [13-16], and so on. These applications impose strict requirement on h-BN film quality and spark the exploration of synthesis methodologies to achieve better films.

The exfoliation method is a very common way to obtain high-quality 2D flakes for research purpose [17]. Even though many different types of exfoliation methods have been developed [18-20], exfoliated flakes are usually very small in size. On the other hand, bottom-up synthesis methods such as chemical vapor deposition (CVD) [21], atomic layer deposition (ALD) [22-23], and molecular beam epitaxy (MBE) [24-31] can produce 2D h-BN films on wafer

scale. The bottom-up synthesis of larger area films relies strongly on the catalytic effect of metal substrates. Various metal substrates have been used for h-BN growth, such Fe [32], Cu [33-34], Co [35-36], Ni [37], etc. Because of their different properties, the thickness, uniformity, nucleation density, and growth speed of h-BN films are different. For example, Fe has been used for the precipitation growth of multilayer h-BN films thanks to its large nitrogen solubility [38-39], while other metal substrates such as Cu and Ni have mostly been used for the growth of single-layer films. However, even though there are various metal substrates to choose from for h-BN growth, the pristine substrate cannot always yield desirable h-BN growth results. Engineering metal substrate properties by the incorporation of impurities provides a solution to this problem. For example, Si was incorporated in Fe substrates to lower the nucleation density of h-BN for the growth of larger flakes [40]; oxygen was reported in improving the catalytic effect of Fe and Cu for better film growth [41-42]; and a recent article from our group reported that carburized Co substrates can improve the adsorption of B and N and eliminate the adlayer growth [43].

In this work, we extend our study of the carburization effects on h-BN growth to Ni substrates. Four different kinds of Ni substrates were obtained after thermal annealing process, namely, the (100)-polycrystal substrate, the (100)-single crystal substrate, the (111)-dominated-polycrystal substrate, and the (111)-single crystal substrate. Single-layer h-BN films with different morphologies were grown on these four types of substrates with and without carburization by MBE. The density functional theory (DFT) and climbing image nudged elastic band (CI-NEB) methods were employed to help explaining the results. Metal-insulator-metal (MIM) devices have been fabricated to characterize their

electrical properties, and a high breakdown electric field of 12.9MV/cm was demonstrated for a single layer h-BN film.

3.2 Experimental Details

3.2.1 Substrate Preparation

The substrates were purchased from Alfa Aesar (Product No. 12046). As received Ni substrates have two different purities. The one with lower purity of 99.997% (Lot No. L21X009) is named type-A, and the one with higher purity of 99.9994% (Lot No. Q19C020) is named type-B for convenience. As received substrates were mechanically polished, then cleaned with acetone, IPA and diluted hydrochloric acid (10%), and deionized (DI) water. Two different annealing treatments were involved, the low temperature annealing (LTA) was performed at 900 °C in MBE chamber with 10-sccm H_2 for 30 mins, and the high temperature annealing (HTA) was performed at 1400 °C in a low-pressure tube furnace with 200-sccm H_2 and 200-sccm Ar, and the pressure was kept at 500 Torr. After LTA, the type-A substrates evolve into two types of substrates, namely the (100)-dominated-polycrystal, and the (100)-single crystal. The (100)-dominated-polycrystal is a result of normal grain growth (NGG), and the formation of (100)-single crystal is a result of abnormal grain growth (AGG) [44]. The AGG happens with a statistical possibility of about 70%, as summarized in our previous paper [43]. Type-B substrates evolve into (111)-dominated-polycrystal after LTA, and no AGG was observed. Since the only difference between type-A and type-B substrates is the purity, and major difference in impurity is the amount of Mn (the certificate of analysis is available on Alfa Aesar website),

we hypothesize that Mn might play a major role in the formation of different textures after LTA. The significant role of Mn in metal grain growth was reported elsewhere [45-46]. The (111)-single crystal substrate was achieved by annealing type-B substrate through HTA. The carburization was achieved by introducing 0.5-sccm C_2H_2 at 900 °C for 4 minutes before growth.

3.2.2 Growth and Characterization

All samples were grown using a Perkin-Elmer MBE system with a background pressure of ~10^{-9} Torr. Boron was supplied by a Knudsen effusion cell filled with B_2O_3 powder (Alfa Aesar, 99.999% purity), and nitrogen was supplied by introducing Ammonia (American Gas Group, 99.9995% purity) through a mass flow controller. XRD spectra were acquired using a Panalytical Empyrean Series 2 system. Secondary electron SEM images and EBSD images were acquired using a FEI NNS450 system. Raman mapping was performed using a HORIBA LabRam system equipped with a 60-mW, 532-nm green laser. Tapping mode AFM images were acquired using a Veeco D5000 AFM system. Bright-field TEM images and SAED patterns were obtained using a FEI Tecnai12 system. XPS spectra were acquired using a Kratos AXIS ULTRA XPS system and deconvoluted using CasaXPS. STM image was acquired using NaioSTM, a tabletop STM from Nanosurf.

3.2.3 Theoretical Calculation

First-principles DFT calculations used the projector augmented wave method and the Perdew–Burke–Ernzerhof (PBE) type generalized gradient approximation [47-48] as implemented in the software package VASP. Spin polarization was included self-

consistently in all the calculations. For the unit cell calculations, a Monkhorst–Pack scheme was adopted to integrate over the Brillouin zone with a k-mesh of 9 × 9 × 1. A plane-wave basis cutoff of 550 eV was used. All structures were optimized until the largest force on the atoms was less than 0.01 eV $Å^{-1}$. The adsorption energies of B and N atoms on the different sites of Ni (111) were modeled. A single B or N atom was placed on a specific site of the surface of a supercell consisting of four atomic layers of Ni atoms. The supercell size in the XY-plane for (111) surface is 4 × 4. The integration over the Brillouin zone for the surfaces was done with a converged k-mesh of 3 × 3 × 1. The sites considered are the Top, FCC, and HCP site of Ni (111). This essentially mimics the epitaxial relationship between h-BN and the substrate atom considered. A vacuum gap of 15 Å was introduced to avoid interactions between the periodically repeated surfaces. To calculate the diffusion activation energies, the CI-NEB method was adopted [49]. The spring force between adjacent images was set to 5.0 eV $Å^{-1}$. The migration energies, namely, diffusion activation energies were obtained for the different adsorbates between the different sites of the (111) surface of Ni. The initial and final positions of the adsorbed atoms were set at two HCP sites of Ni (111). Eight images were considered to calculate the activation energies between the initial and final states. For calculation of adsorption and diffusion energies for B and N on carbon-incorporated Ni, one interstitial carbon occupying the octahedral site in a supercell of Ni (111), which is 1.58 Å below the surface, was assumed.

3.2.4 Device Fabrication and Characterization

Metal-insulator-metal (MIM) devices were fabricated by depositing metal contacts (Ni) of 100 nm on as grown film using e-beam evaporation. Photolithography and etching were

performed to form square Ni metal contacts of 50 μm × 50 μm. The Ni substrate was used as a global bottom contact for all devices. Device characterization was performed on a Signatone probe station connected with an Agilent 4155C semiconductor parameter analyzer.

3.3 Results and Discussion

3.3.1 Growth results on four different substrates

Ni substrates evolve into four different textures after the thermal annealing process. Figure 3.1 presents characterization results of the four different substrates, with the first column showing the X-ray diffraction (XRD) results, the second and third columns showing the electron backscatter diffraction (EBSD) band contrast and Z-axis inverse pole figure (IPF Z) images, respectively. The XRD results reveal the dominating surface directions in large area, while the EBSD results provide detailed information about the surface texture, such as grain size and high indexed surfaces. The substrates having results in Figure 3.1 a-c, d-f, g-i, and j-k were designated as (100)-dominated-poly substrate, (100)-single crystal substrate, (111)-dominated-polycrystal substrate, and (111)-single crystal substrates, respectively. It's worth noting that even though the XRD result in Figure 3.1g shows a dominating (111) peak for (111)-dominated-polycrystal substrates, the corresponding IPF Z image in Figure 3.1c reveals that the (111) grains only occupy a small portion across the whole surface. As a matter of fact, the surface also contains (100) and many other high-index surfaces. This discrepancy is caused by the diffraction selection rules of XRD; for face centered cubic (FCC) metal, only those surfaces with Miller indexes

(h, k and l) all odd or all even are allowed for reflections. On the other hand, even though EBSD is more detailed in showing surface textures, it can only show an image from a very small area of the whole sample. Therefore, both XRD and EBSD were used to obtain accurate information about the substrates.

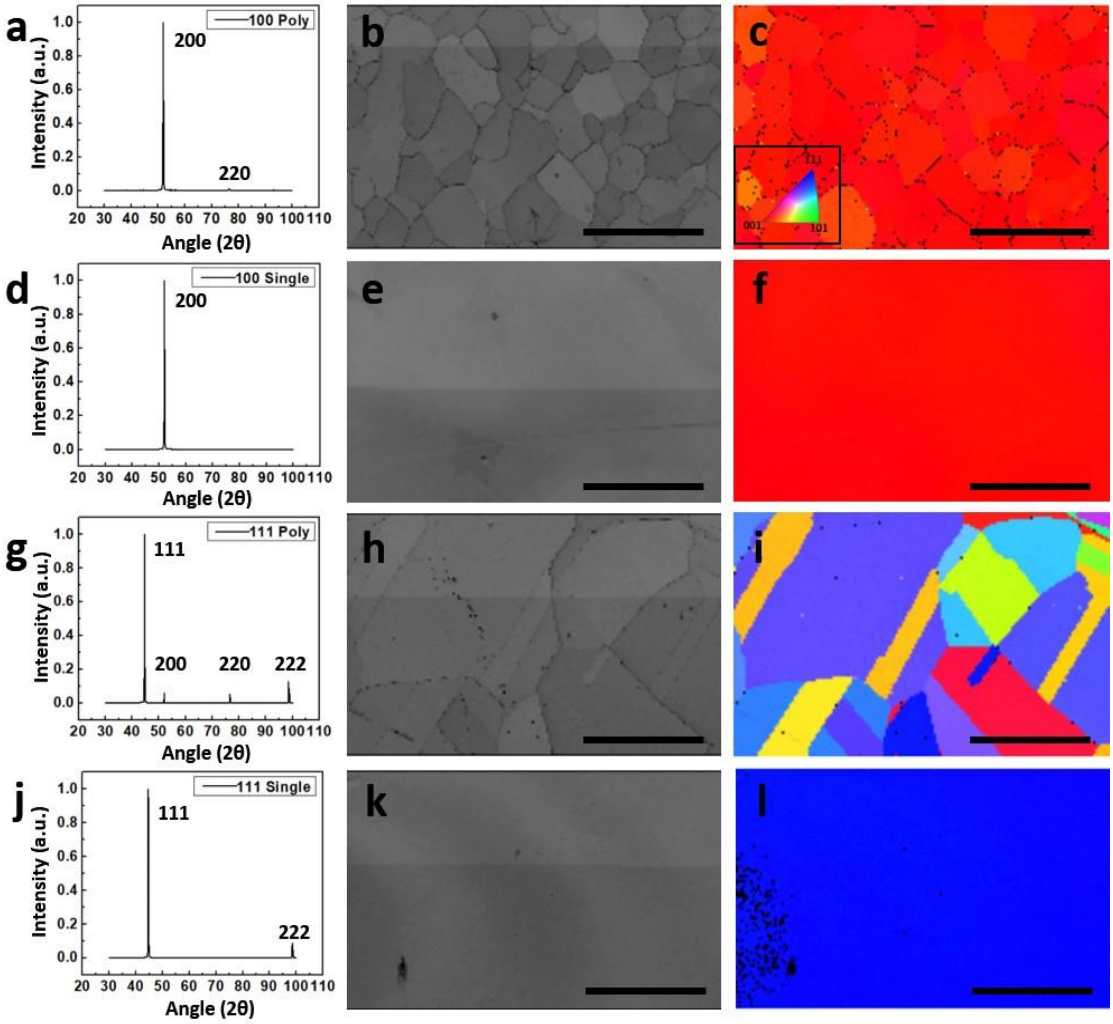

Figure 3.1. Characterization of four different types of Ni substrates. (a-c) (100)-dominated-polycrystal substrate; (d-f) (100)-single crystal substrate; (g-i) (111)-dominated-polycrystal substrate; (j-l) (111)-single substrate. The first column (a/d/g/j) shows XRD results, the second column (b/e/h/k) shows EBSD band contrast maps, and the third column (c/f/i/l) shows EBSD IPF Z images taken at the same area shown in the second column. All scale bars are 500 μm.

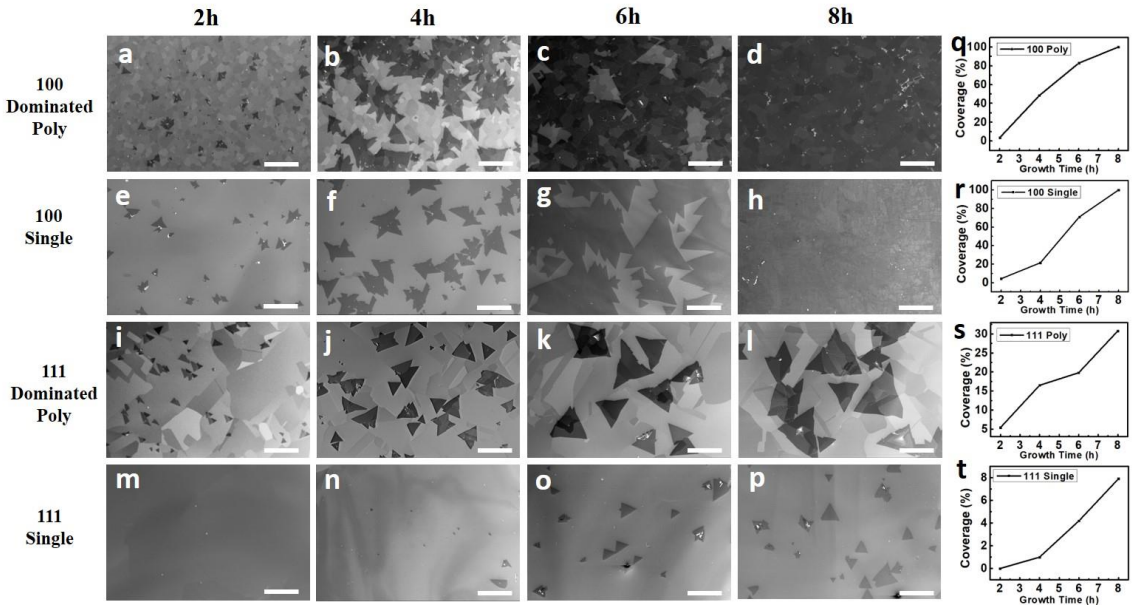

Figure 3.2. Results of time dependent growth of h-BN on carburized Ni substrates. (a-d) SEM images of h-BN samples on (100)-dominated-polycrystal substrates at a growth time of 2, 4, 6, and 8 hours, respectively, (e-h) SEM images of h-BN samples on (100)-single crystal substrates at a growth time of 2, 4, 6, and 8 hours, respectively, (i-l) SEM images of h-BN samples on (111)-dominated-polycrystal substrates at a growth time of 2, 4, 6, and 8 hours, respectively, (m-p) SEM images of h-BN samples on (111)-single crystal substrates at a growth time of 2, 4, 6, and 8 hours, respectively. (q-t) plots of h-BN coverage versus growth time on (100)-dominated polycrystal, (100)-single crystal, (111)-dominated polycrystal, and (111)-single crystal Ni substrates, respectively. All Ni substrates were carburized with 0.5-sccm C_2H_2 for 4 min at 900 °C before growth. All samples were grown at 880 °C with 10-sccm ammonia and B_2O_3 cell kept at 1150 °C. All scare bars here are 500 μm.

Figure 3.2 shows SEM characterization results of growth time dependent samples on the four different types of substrates. All samples were grown at 880 °C with 10-sccm ammonia and B_2O_3 cell at 1150 °C. Before introduction of B and N sources, the Ni substrates were carburized with 0.5-sccm C_2H_2 for 4 min at 900 °C. The C_2H_2 gas flow rate and duration were controlled to attain small amount of interstitial carbon in the Ni substrate for tuning its catalytic strength only, in other words, the amount of carbon was not enough for the formation of any graphene, graphite, or carbide during growth. The

proof of this using XPS studies is given elsewhere [37]. Similar studies of carburization of Co substrates showed that while high-amount carbon incorporation results in the formation of graphene or graphitic structures, low-amount carbon incorporation in the Co substrates as interstitials does not lead to these structures, instead it effectively tunes the catalytic effect of the substrates for h-BN growth [25, 35, 43]. Figure 3.2 a-d and e-h show SEM images of h-BN films on (100)-dominated-polycrystal and (100)-single crystal substrates, respectively. The growth results on these (100)-substrates are similar. Small and sparse h-BN flakes are formed at the early growth stage, and these flakes grow larger and merge with each other as the growth time increases. Continuous films are formed after 8 hours. The growth rate of h-BN on the polycrystalline substrates is slightly larger than that of the single crystal substrates, which may be due to an increase in the nucleation rate of h-BN around the grain boundaries [50]. In addition, the h-BN film on the (100)-dominated-polycrystal substrate appears to be less uniform due to the formation of adlayers (white features in Figure 3.2d), which is also attributed to crystallographic defects on the polycrystal substrate [50]. Figure 3.2 i-l show SEM images of h-BN films on (111)-dominated-polycrystal substrates. The growth results for growth times less than 4 hours are similar to that of the (100) substrates. However, as the growth time increases further, the flakes grow larger, but they do not merge to form continuous films. Instead, sub-millimeter sized triangular flakes are formed after 8-hour growth. Figure 3.2 m-p show SEM images of h-BN samples on (111)-single crystal substrates. Intriguingly, even though the Ni (111) surface has the same 6-fold symmetry as that of h-BN, the coverage and flake size of h-BN are extremely small compared to the growth on all other three substrates,

indicating that Ni (111) single crystal surfaces are less preferable for h-BN growth under the growth conditions imposed. In contrast, larger h-BN flakes and higher coverage of h-BN on (111)-dominated-polycrystal substrates clearly indicate that the nucleation and growth have been assisted by other factors such as grain boundaries and existing various other facets such as (100) and high indexed surfaces (Figure 3.1 g & i), which may be more preferable nucleation surfaces than (111) [51-52]. Figure 3.2 q-t show the plots of h-BN coverage as a function of growth time for the samples grown on (100)-dominated polycrystal, (100)-single crystal, (111)-dominated polycrystal, and (111)-single crystal Ni substrates, respectively. The coverage data were obtained using the ImageJ software package [43]. While the coverage increases as the increase of the growth time on all four types of substrates, the growth speed decreases monotonously for the h-BN on the substrates from (100)-dominated polycrystal, to (100)-single crystal, to (111)-dominated polycrystal, and to (111)-single crystal Ni substrates.

3.3.2 Influence of growth temperature

The (100)-single crystal and (111)-single crystal Ni substrates were selected for temperature dependent growth to further study h-BN growth behavior. All samples were grown with 10-sccm ammonia and B_2O_3 cell at 1150 °C for 6 hours. Figure 3.3 a-e show SEM images of h-BN samples on carburized single crystal Ni (100) substrates at a growth temperature ranging from 867 °C to 895 °C, respectively. Figure 3.3f shows the evolution of h-BN coverage versus growth temperature for this batch of samples. The h-BN coverage increases as the substrate temperature increases, the highest coverage of 85% is attained at around 880 °C, and the coverage decreases as the temperature increases further. Figures

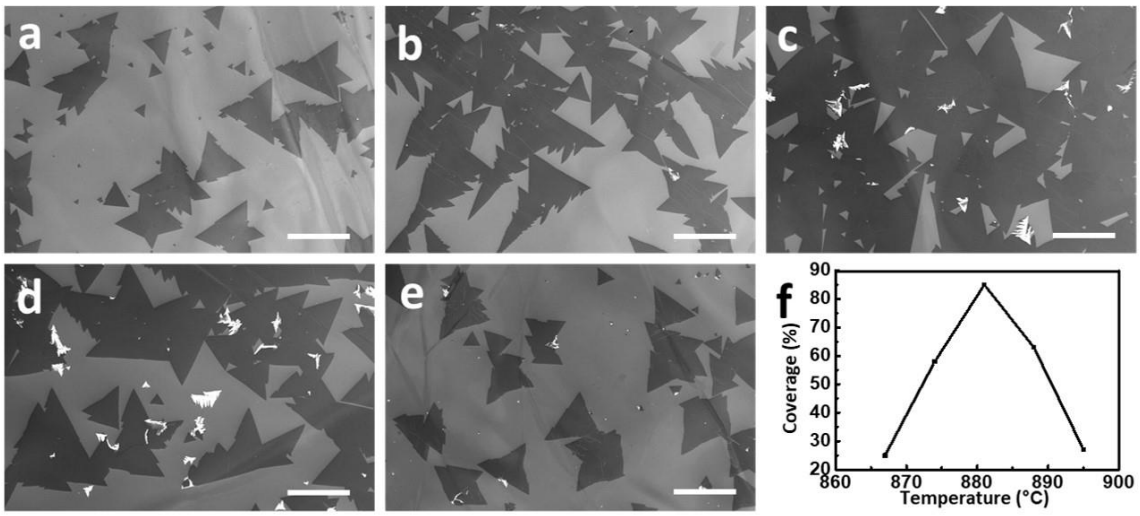

Figure 3.3. Temperature dependent growth of h-BN on carburized Ni (100)-single crystal substrates. (a-e) SEM images of as grown h-BN samples with growth temperature ranging from 867 to 895 °C, respectively, (f) plot of h-BN coverage versus growth temperature for this batch of samples. All samples were grown with 10-sccm ammonia and B_2O_3 cell kept at 1150 °C for 6 h. All scare bars here are 500 μm.

3.4 a-e show SEM images of h-BN samples on single crystal Ni (111) substrates without carburization at a growth temperature from 846 to 874 °C, respectively. The evolution of h-BN coverage versus growth temperature is plotted in Figure 3.4f. Similarly, the h-BN coverage increases as the substrate temperature increases. The peak coverage is achieved at around 860 °C, which is about 20 °C lower than that on single crystal Ni (100) substrates. As the substrate temperature increases beyond 860 °C, the coverage decreases. These coverage-temperature plots indicate that the growth speed of h-BN has a nearly parabolic relationship with the growth temperature. This phenomenon was also reported in MBE growth of GaAs [53-54]. In general, there is an optimized growth temperature, around which the adsorption, diffusion, and bonding processes coordinate with each other to achieve the highest growth speed. Decreasing the temperature will hinder the diffusion and bonding processes, while increasing the temperature will enhance desorption exponentially.

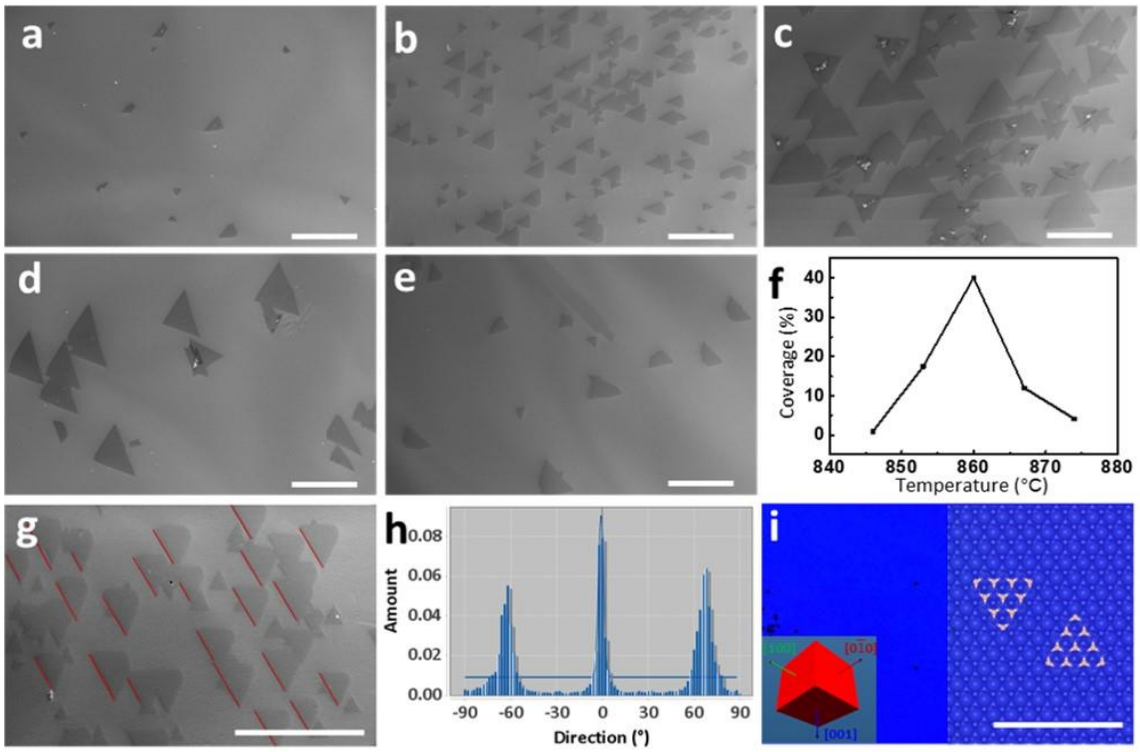

Figure 3.4. Temperature dependent growth of h-BN on pristine Ni (111) single crystal substrate. (a-e) SEM images of as grown h-BN samples with growth temperature ranging from 846 to 874 °C, respectively, (f) plot of h-BN coverage versus growth temperature for this batch of samples, (g) SEM image of another area on sample shown in (b) for EBSD mapping. The red lines mark one of the dominate edge directions, (h) directionality histograms of image (g) showing three dominated edge directions separated by 60°, (i) IPF Z image of EBSD mapping showing the blue color of (111) surface. Inset on the lower left shows the corresponding unit cell. Transparent inset on the right-hand side shows the substrate atom arrangement revealed by the unit cell. Two equivalent h-BN flakes with B atoms sitting on FCC sites, and N atoms sitting on Top sites. All samples were grown with 10-sccm ammonia and B_2O_3 cell kept at 1150 °C for 6 h. All scare bars here are 500 μm.

Therefore, both lead to lower growth rate. Another interesting phenomenon is that most of the flakes are well aligned on the (111)-single crystal substrates. Figure 3.4g shows an SEM image, which was taken from another part of the sample shown in Figure 3.4b. One of the aligned edges are marked with red lines to illustrate the alignment. The edge directions of the h-BN flakes were further analyzed with ImageJ software [55]. Figure 3.4h

shows the result. Three groups of edge's directions are observed with the center separated by around 60°. Figure 3.4i shows the result of EBSD mapping of the same area shown in Figure 3.4g. The blue color in IPF Z images represents (111) surfaces, while the corresponding unit cell reveals the close packed directions of surface atoms. Based on the surface direction revealed by unit cell, we can tell that red lines in Figure 3.4g are aligned with the $\langle 10\bar{1} \rangle$ direction. An image of corresponding Ni atom arrangement is superimposed on the IPF Z figure. Based on the SEM and EBSD results, two atom models of h-BN flake with identical registration relationship to the substrate are overlaid on the IPF Z figure, with B siting on the FCC site, and N siting on the TOP site. This registration relationship of h-BN on Ni (111) surface is supported by experimental [56-57] and DFT calculation results reported elsewhere [58-60]. The work here suggests that Ni (111) substrates can be another candidate for wafer-scale single crystal h-BN film growth. Nevertheless, the peak coverage is only about 40% under this growth condition. Increasing the growth time should lead to the full coverage.

3.3.3 Influence of carburization

To reveal the effect of carburization on the four types of substrates for h-BN growth, we compare results in Figure 3.5. The first and the second columns show SEM images of the samples grown on carburized substrates and pristine substrates, respectively. The third column shows the comparison of h-BN coverage for each type of the substrates. Figures 3.5a, c, e are the 6-h growth samples reproduced from Figure 3.2. The results on (111)-single crystal substrates (Figures 3.5 g, h) were obtained at a growth temperature of 860 °C, namely 20 °C lower than that for other samples. All other growth conditions are the

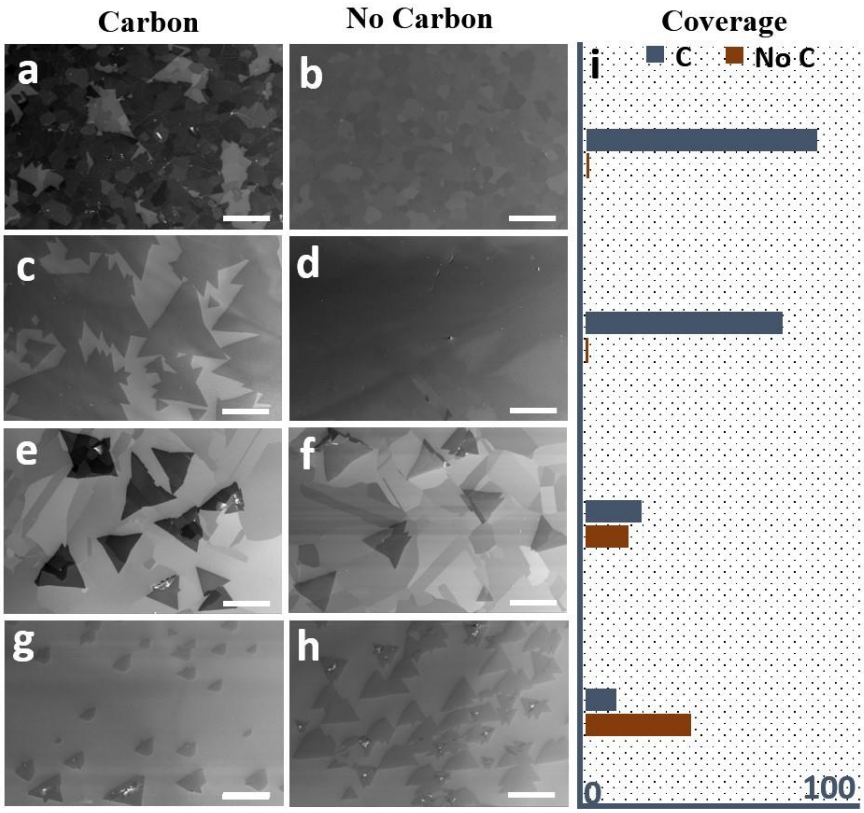

Figure 3.5. Carburization dependent growth of h-BN on different Ni substrates. (a/b) SEM images of h-BN samples on (100)-dominated-polycrystal substrates with and without carburization, respectively, (c/d) SEM images of h-BN samples on (100)-single crystal substrates with and without carburization, respectively, (e/f) SEM images of h-BN samples on (111)-dominated-polycrystal substrates with and without carburization, respectively, (g/h) SEM images of h-BN samples on (111)-single crystal substrates with and without carburization, respectively, (i) comparison of h-BN coverage with and without carbon on each substrate. All samples were grown with 10-sccm ammonia and B_2O_3 cell kept at 1150 °C for 6 hours. Carburization was done by introducing 4-sccm C_2H_2 for 4 min at 900 °C prior to growth. All scare bars here are 500 µm.

same. Figures 3.5 a/b and c/d show SEM images of h-BN samples on (100)-polycrystal and (100)-single crystal Ni substrates, respectively. Substantial coverage of h-BN was obtained on carburized substrates, but no growth occurred on pristine substrates, which means the carburization is essential for h-BN growth on Ni (100) surfaces at current growth conditions. Details regarding this aspect have already been reported elsewhere [61]. Figures

3.5 e/f and g/h show SEM images of h-BN samples grown on (111)-dominated-polycrystal and (111)-single crystal Ni substrates, respectively. There is growth on both carburized and pristine substrates: h-BN coverage is slightly higher on the carburized (111)-dominated-polycrystal substrate than that on the pristine (111)-dominated-polycrystal substrate. Since the (111)-dominated substrates consist of the mixture of (111), (100) and some other high indexed grains as shown in Figure 3.1, the incorporation of carbon into (100) and other higher index surfaces might have catalyzed more growth on the substrates. On the other hand, the h-BN coverage is clearly smaller with carburization than without carburization on (111)-single crystal Ni substrates. This is intriguing since the incorporation of carbon in pure Ni (111) substrates reduces its catalytic effect, which is exactly opposite to our observations on Ni (100) substrates [61].

To clarify the effect of carbon incorporation in Ni (111) on the nucleation and growth of h-BN, we carried out simulations using DFT and CI-NEB methods. Detailed information about the methodologies is reported elsewhere [61] and also briefly summarized in the Methods section. Since ammonia and B_2O_3 were used as sources, various species such as B and N atoms, B_xO_y, NH_x chemical compounds may be present on the hot Ni substrates during the growth. Nevertheless, Ni was used as a catalyst for N adatom and H_2 generation from the decomposition of NH_3 [62], and B_2O_3 is thermally decomposed to B atoms and O_2 gas in the effusion cell at high temperature. Thus, B and N atoms are considered as the dominant reactive species on the substrates for the nucleation and growth of h-BN here. The nucleation activation energy E_a is expressed as:

a

Adsorption Energy eV/atom	Adsorption sites	Ni (111)	
		Pristine	With C
B	FCC	1.94	2.70
	HCP	1.85	2.18
	Top	3.77	4.09
N	FCC	-2.16	-0.87
	HCP	-2.14	-1.62
	Top	0.66	1.03

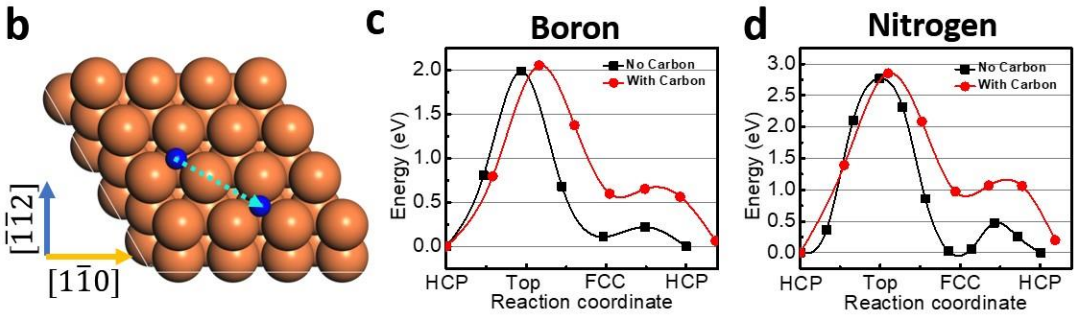

Figure 3.6. Theoretical calculation of adsorption and diffusion energies of B and N atoms on Ni (111) with and without an embedded interstitial carbon at adjacent subsurface octahedral site. (a) DFT calculation of adsorption energies of B and N on Ni (111), (b-d) CI-NEB calculation of diffusion energy of B and N on Ni (111). (b) Top view of the diffusion path from an FCC site to an adjacent HCP site; (c) and (d) are the energy profiles of B and N diffusing along the path indicated in (b).

$$E_a = E_{ads} + E_{diff} + E_{att}, \quad (1)$$

where E_{ads} is the adsorption energy, E_{diff} is the energy barrier for diffusion on the substrate surface, and E_{att} is the attachment energy, namely, the energy barrier to form a B-N covalent bond. Smaller E_a means easier growth, in turn, larger film coverage. Since the amount of carbon incorporation in Ni (111) is low, the change to the lattice constant of Ni (111) can be negligible, which means the change of attachment energies before and after carburization can be assumed to be insignificant. Thus, the effect of carburization on the

nucleation is mainly dominated by the absorption and diffusion energies. The adsorption energies of B and N atoms on Ni are defined in the following expression,

$$E_{ads} = -E_{B/N} - E_{surface} + E_{B/N\ on\ surface}, \quad (2)$$

where $E_{B/N}$ is the chemical potential of B or N, and $E_{surface}$ is the energy of clean Ni surface without adsorbents, and $E_{B/N\ on\ surface}$ is the total energy of B and N adsorbed on Ni surface. Smaller E_{ads} means more stable adsorption. Three different adsorption sites were calculated, namely, the FCC site, the HCP site, and the Top site. Figure 3.6a shows the DFT calculation results of adsorption energy. The adsorption energies of B and N atoms on Ni (111) surface are larger with a carbon atom placed at the adjacent subsurface octahedral site, indicating adverse effect of embedded carbon on adsorption process. Figures 3.6 b-d show the CI-NEB calculation of diffusion energy. The diffusion path is shown in Figure 3.6b. A B or N atom diffuses from an HCP site, through a TOP site, an FCC site, and a bridge site to the second nearest HCP site, so that all diffusion scenarios are included. Figures 3.6 c-d show the calculated energy profiles of B and N versus adsorption positions. The black lines are energy profiles on pristine substrates, and the red lines are energy profiles on substrates with a carbon placed at the octahedral site along the diffusion path. As seen from Figures 3.6 c-d, the energy barriers of B and N diffusing from an HCP site to the second nearest HCP site are increased on carburized substrate, indicating the adverse effect of carbon incorporation on the diffusion process. With the increased adsorption and diffusion energies, the h-BN nucleation energy E_a increases with the incorporation of carbon, which reduces the h-BN growth on Ni (111) surfaces. The conclusion is consistent with our experimental results.

3.3.4 Characterization of h-BN film and MIM devices

Finally, we carried out in-depth characterization of the continuous h-BN film on carburized Ni (100) single crystal substrate (Figure 3.2h) since the film arguably has the best uniformity and continuity among all samples studied here. Figure 3.7a shows a photo of an as-grown sample placed next to a penny. The area covered by h-BN film exhibits blue color under illumination of white light from certain angle. The blue color is a result of light scattering from reconstructed surface. Figure 3.7b shows an STM image of the sample. The image was taken using a Nanosurf tabletop STM system at room temperature and ambient environment. Positive voltage was applied to the tip, therefore, only N atom was resolved. The image is distorted slightly due to the thermal drift, but the hexagonal arrangement of N atoms is evident. The average distance of N atoms was measured to be 0.24 nm, which is close to its theoretical value of 0.25 nm. Figure 3.7c shows XPS spectrum of the sample. B_1s and N_1s peaks are located at around 190 eV, and 397.5 eV, respectively. Figure 3.7d shows the AFM results taken on a transferred h-BN film. The thickness was measured to be 0.8 nm, corresponding to single-layer h-BN film. The larger experimental value comparing to theoretical value is due to the tip effect and trapped water and gas molecules in the interface between h-BN and SiO_2 substrate [50]. Figure 3.7e shows the Raman mapping near the edge of the transferred h-BN film, indicating uniform contrast over 200 μm^2. Figure 3.7f shows 9 Raman spectra extracted randomly from the region with rose color on the mapping data. The peak position is determined to be 1370 cm^{-1}, which implies that the h-BN film is single-layer [63].

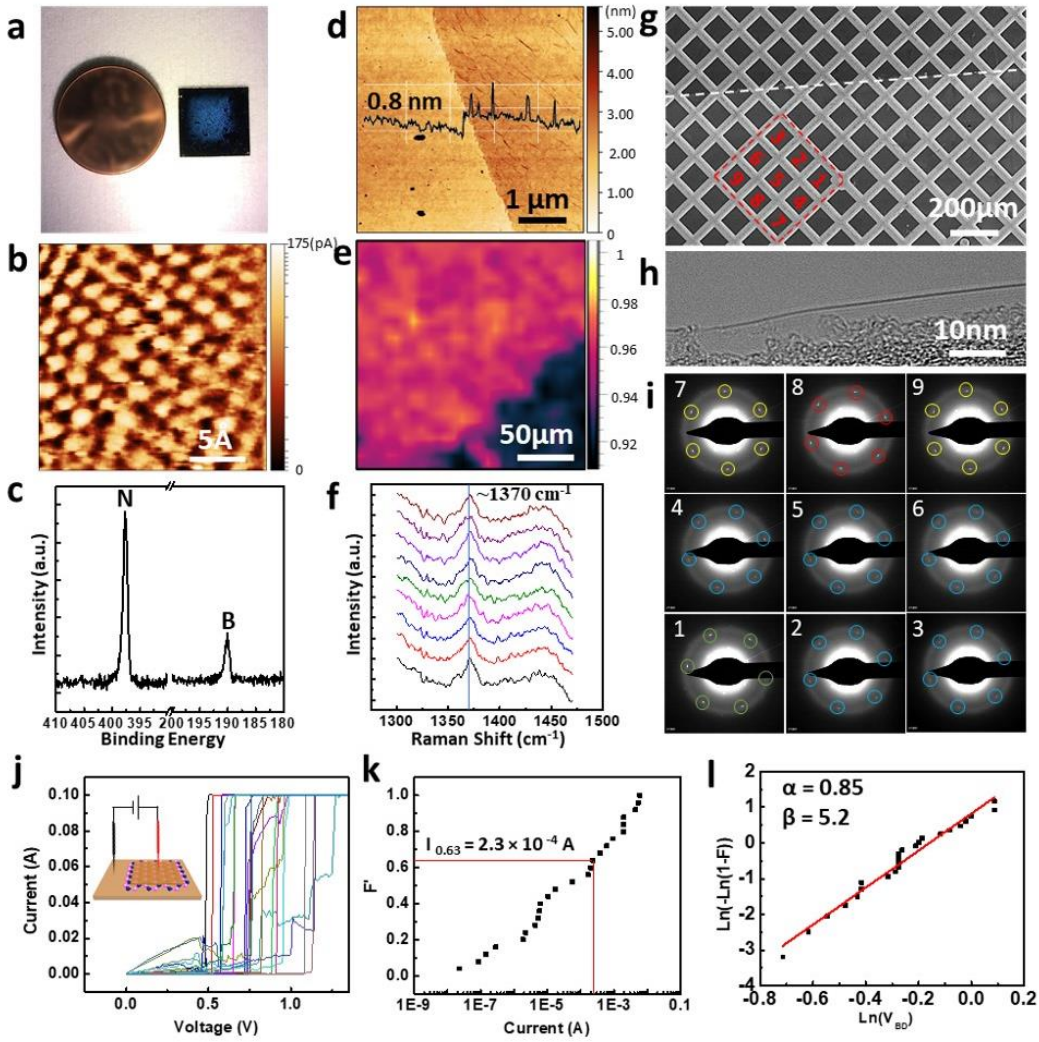

Figure 3.7. In-depth characterization of continuous h-BN film grown on (100)-single crystal Ni substrate. (a) Photo of as grown h-BN samples placed next to a penny coin. The blue color is caused by Ni surface reconstruction under h-BN film, (b) STM image of as-grown h-BN film showing the honeycomb structure of single layer film, (c) XPS spectrum of as-grown h-BN film, (d) AFM image of a transferred h-BN film, with the inset showing film thickness of 0.8 nm, (e) Raman mapping of a transferred h-BN film, (f) nine Raman spectra obtained from 9 random positions on Raman mapping showing the peak position at around 1370 cm^{-1}, (g) SEM image of h-BN film transferred onto TEM grid. The dotted line highlights the boundary of h-BN film, the red square and numbers mark the position of taking SAED patterns, (h) TEM image taken at the edge of h-BN film, (i) nine SAED patterns taken at corresponding areas marked in (g). The colored circles mark SAED patterns with the same azimuthal angles, (j) current–voltage characteristics of 25 Ni/h-BN/Ni capacitor devices. The inset shows the schematic of the device, (k) cumulative probability distribution of tunneling current at 0.1 V, (l) Weibull plot of breakdown voltages.

Figure 3.7g shows an SEM image of the h-BN film transferred on a TEM grid. The lower half is covered by h-BN film, and the white line marks the edge of h-BN film. The red square and numbers mark the region for selected area electron diffraction (SAED) analysis. Figure 3.7h shows a TEM image taken at the edge of h-BN film where the film is folded, enabling the imaging of the cross section of the film. Single-layer h-BN film is revealed. Figure 3.7i shows the 9 SAED patterns. The dimension of the square meshes marked in Figure 3.7g is 200 μm, and the SAED patterns were taken at their center areas. SAED patterns with the same azimuth angle were marked with the same color. Identical azimuth angles indicate identical atom arrangement, thereby, these atoms in the investigated area belong to the same crystal domain. As seen from the figure, three sets of SAED patterns are observed, indicating the polycrystal nature of the h-BN film. Even though the substrate is single crystal Ni (100), the h-BN flakes grown on top are randomly oriented due to the lack of epitaxial relationship, leading to polycrystal films. The grain size of polycrystal h-BN film is around 600 μm based on the SEM and TEM results. Larger grain size yields fewer grain boundaries.

Figure 3.7j shows I-V characteristics of 25 metal-insulator-metal (MIM) devices. The fabrication and characterization methodology are described in the Methods section. The inset is the characterization configuration. The voltage is swept from 0 to 1.5V, and the compliance current is set to be 0.1 A. At low voltages (< 0.2~0.3 V), the current mostly increases linearly with an increase of the voltage, indicating direct tunneling [64]. The tunneling current fluctuates in some devices as the voltage increases, which is due to the trap assisted tunneling [65]. These traps are formed due to the defects, such as h-BN grain

boundaries as discussed above. As the voltage is further increased, the devices start to breakdown, and the current increases sharply and reaches the compliance current. Figure 3.7k shows the cumulative probability of the tunneling currents at a bias of 0.1 V. The most probable tunneling currents at 0.1 V are obtained by setting the cumulative probability at 63.2%, yielding a value of 2.3×10^{-4}A. The direct tunneling current of a MIM device is expressed as [64, 66-67]:

$$\mathrm{I(V,T)} = \mathrm{I(V,0)} \times \left\{1 + \left[\frac{3\times10^{-9}(dT)^2}{\Phi_B/q}\right]\right\}, \quad (3)$$

where $\mathrm{I(V,0)} = \frac{A_{eff}\sqrt{2m\Phi_B}q^2V}{h^2d}\exp\left(\frac{-4\pi d\sqrt{2m\Phi_B}}{h}\right)$, m is the electron effective mass, which is $0.26\,m_0$, h is the Plank's constant, q is the fundamental charge, Φ_B is 3.0 eV [10, 67-68], d is 0.66 nm assuming this is the van der Waals distance between the top and the bottom contacts, and T is equal to 293K. Based on the tunneling current value at $0.1\ V$, an effective area A_{eff} is calculated to be $0.027\ \mu m^2$. This value is orders of magnitude smaller than the physical device area of 50 µm × 50 µm, suggesting that electron tunneling goes through a very small local area only [67]. Detailed studied of this phenomenon is provided in the next chapter. Figure 3.7i shows the Weibull plot of breakdown voltage V_{BD}. The cumulative failure probability F of breakdown voltage is defined as [67, 69]:

$$\mathrm{F}(V_{BD}) = 1 - \exp\left[-\left(\frac{V_{BD}}{\alpha}\right)^{\beta}\right], \quad (4)$$

where the scale parameter α indicates the most probable breakdown voltage, and the shape parameter β indicates the width of the distribution. This function can also be rearranged as:

$$\ln[-\ln(1-\mathrm{F})] = \beta \ln(V_{BD}) - \beta \ln\alpha. \quad (5)$$

Therefore, based on the plot of $\ln[-\ln(1-F)]$ versus $\ln(V_{BD})$, we extracted the value of α and β as 0.85 and 5.2, respectively. Using the breakdown voltage indicated by α, 0.85V, we can derive the breakdown electric field of the single-layer h-BN film as 12.9 MV/cm, which is comparable to that of exfoliated h-BN [6].

3.4 Conclusion

We have presented on the results of h-BN growth on four different kinds of Ni substrates. It has been found that carburization can enhance h-BN growth on Ni (100) surfaces, while suppresses h-BN growth on Ni (111) surfaces. DFT and CI-NEB calculations reveal that the adsorption and diffusion of B and N atoms on Ni (111) are suppressed by embedded interstitial carbon atoms. Well aligned h-BN flakes can be obtained on Ni (111) substrates. MIM devices were fabricated on as grown single-layer h-BN film on single crystal Ni (100), and the breakdown electric field was determined to be 12.9 MV/cm. Our work reveals the strong influence of substrate properties on h-BN growth, and explores the strategy of engineering the substrates to obtain better films.

3.5 References

1. Liu, C.; Yu, Z.; Neff, D.; Zhamu, A.; Jang, B. Z. Graphene-Based Supercapacitor with an Ultrahigh Energy Density. *Nano Letters* **2010,** *10* (12), 4863-4868.

2. Cui, Y.; Xin, R.; Yu, Z.; Pan, Y.; Ong, Z. Y.; Wei, X.; Wang, J.; Nan, H.; Ni, Z.; Wu, Y. High-performance Monolayer WS_2 Field-Effect Transistors on High-κ Dielectrics. *Advanced Materials* **2015,** *27* (35), 5230-5234.

3. Liu, W.; Kang, J.; Sarkar, D.; Khatami, Y.; Jena, D.; Banerjee, K. Role of Metal Contacts in Designing High-Performance Monolayer n-Type WSe2 Field Effect Transistors. *Nano Letters* **2013,** *13* (5), 1983-1990.

4. Jing, X.; Panholzer, E.; Song, X.; Grustan-Gutierrez, E.; Hui, F.; Shi, Y.; Benstetter, G.; Illarionov, Y.; Grasser, T.; Lanza, M. Fabrication of Scalable and Ultra Low Power Photodetectors with High Light/Dark Current Ratios Using Polycrystalline Monolayer MoS_2 Sheets. *Nano Energy* **2016,** *30*, 494-502.

5. Cassabois, G.; Valvin, P.; Gil, B. Hexagonal Boron Nitride Is an Indirect Bandgap Semiconductor. *Nature Photonics* **2016,** *10* (4), 262-266.

6. Hattori, Y.; Taniguchi, T.; Watanabe, K.; Nagashio, K. Layer-by-Layer Dielectric Breakdown of Hexagonal Boron Nitride. *ACS Nano* **2015,** *9* (1), 916-921.

7. Jo, I.; Pettes, M. T.; Kim, J.; Watanabe, K.; Taniguchi, T.; Yao, Z.; Shi, L. Thermal Conductivity and Phonon Transport in Suspended Few-Layer Hexagonal Boron Nitride. *Nano Letters* **2013,** *13* (2), 550-554.

8. Kostoglou, N.; Polychronopoulou, K.; Rebholz, C. Thermal and Chemical Stability of Hexagonal Boron Nitride (h-BN) Nanoplatelets. *Vacuum* **2015,** *112*, 42-45.

9. Lee, G.-H.; Yu, Y.-J.; Cui, X.; Petrone, N.; Lee, C.-H.; Choi, M. S.; Lee, D.-Y.; Lee, C.; Yoo, W. J.; Watanabe, K. Flexible and Transparent MoS2 Field-Effect Transistors on Hexagonal Boron Nitride-Graphene Heterostructures. *ACS Nano* **2013,** *7* (9), 7931-7936.

10. Jang, S. K.; Youn, J.; Song, Y. J.; Lee, S. Synthesis and Characterization of Hexagonal Boron Nitride as a Gate Dielectric. *Scientific Reports* **2016,** *6*, 30449.

11. Jing, X.; Puglisi, F.; Akinwande, D.; Lanza, M. Chemical Vapor Deposition of Hexagonal Boron Nitride on Metal-Coated Wafers and Transfer-Free Fabrication of Resistive Switching Devices. *2D Materials* **2019,** *6* (3), 035021.

12. Pan, C.; Miranda, E.; Villena, M. A.; Xiao, N.; Jing, X.; Xie, X.; Wu, T.; Hui, F.; Shi, Y.; Lanza, M. Model for Multi-Filamentary Conduction in Graphene/Hexagonal-Boron-Nitride/Graphene Based Resistive Switching Devices. *2D Materials* **2017,** *4* (2), 025099.

13. Dean, C. R.; Young, A. F.; Meric, I.; Lee, C.; Wang, L.; Sorgenfrei, S.; Watanabe, K.; Taniguchi, T.; Kim, P.; Shepard, K. L. Boron Nitride Substrates for High-Quality Graphene Electronics. *Nature Nanotechnology* **2010,** *5* (10), 722-726.

14. Dean, C. R.; Young, A. F.; Cadden-Zimansky, P.; Wang, L.; Ren, H.; Watanabe, K.; Taniguchi, T.; Kim, P.; Hone, J.; Shepard, K. Multicomponent Fractional Quantum Hall Effect in Graphene. *Nature Physics* **2011,** *7* (9), 693-696.

15. Cui, X.; Lee, G.-H.; Kim, Y. D.; Arefe, G.; Huang, P. Y.; Lee, C.-H.; Chenet, D. A.; Zhang, X.; Wang, L.; Ye, F. Multi-Terminal Transport Measurements of MoS_2 Using a van der Waals Heterostructure Device Platform. *Nature Nanotechnology* **2015,** *10* (6), 534-540.

16. Murakami, K.; Igari, T.; Mitsuishi, K.; Nagao, M.; Sasaki, M.; Yamada, Y. Highly Monochromatic Electron Emission from Graphene-Hexagonal Boron Nitride-Si Heterostructure. *ACS Applied Materials & Interfaces* **2020,** *12* (3), 4061-4067.

17. Novoselov, K. S.; Geim, A. K.; Morozov, S. V.; Jiang, D.; Zhang, Y.; Dubonos, S. V.; Grigorieva, I. V.; Firsov, A. A. Electric Field Effect in Atomically Thin Carbon Films. *Science* **2004,** *306* (5696), 666-669.

18. Huang, Y.; Sutter, E.; Shi, N. N.; Zheng, J.; Yang, T.; Englund, D.; Gao, H.-J.; Sutter, P. Reliable Exfoliation of Large-Area High-Quality Flakes of Graphene and Other Two-Dimensional Materials. *ACS Nano* **2015,** *9* (11), 10612-10620.

19. Hernandez, Y.; Nicolosi, V.; Lotya, M.; Blighe, F. M.; Sun, Z.; De, S.; McGovern, I.; Holland, B.; Byrne, M.; Gun'Ko, Y. K. High-Yield Production of Graphene by Liquid-Phase Exfoliation of Graphite. *Nature Nanotechnology* **2008,** *3* (9), 563-568.

20. Zhao, H.-R.; Ding, J.-H.; Shao, Z.-Z.; Xu, B.-Y.; Zhou, Q.-B.; Yu, H.-B. High-Quality Boron Nitride Nanosheets and Their Bioinspired Thermally Conductive Papers. *ACS Applied Materials & Interfaces* **2019,** *11* (40), 37247-37255.

21. Shi, Y.; Hamsen, C.; Jia, X.; Kim, K. K.; Reina, A.; Hofmann, M.; Hsu, A. L.; Zhang, K.; Li, H.; Juang, Z.-Y. Synthesis of Few-Layer Hexagonal Boron Nitride Thin Film by Chemical Vapor Deposition. *Nano Letters* **2010,** *10* (10), 4134-4139.

22. Ferguson, J.; Weimer, A.; George, S. Atomic Layer Deposition of Boron Nitride Using Sequential Exposures of BCl3 and NH3. *Thin Solid Films* **2002,** *413* (1-2), 16-25.

23. Driver, M. S.; Beatty, J. D.; Olanipekun, O.; Reid, K.; Rath, A.; Voyles, P. M.; Kelber, J. A. Atomic Layer Epitaxy of h-BN (0001) Multilayers on Co (0001) and Molecular Beam Epitaxy Growth of Graphene on h-BN (0001)/Co (0001). *Langmuir* **2016,** *32* (11), 2601-2607.

24. Nakhaie, S.; Wofford, J.; Schumann, T.; Jahn, U.; Ramsteiner, M.; Hanke, M.; Lopes, J.; Riechert, H. Synthesis of Atomically Thin Hexagonal Boron Nitride Films on Nickel Foils by Molecular Beam Epitaxy. *Applied Physics Letters* **2015,** *106* (21), 213108.

25. Zuo, Z.; Xu, Z.; Zheng, R.; Khanaki, A.; Zheng, J.-G.; Liu, J. In-situ Epitaxial Growth of Graphene/h-BN van der Waals Heterostructures by Molecular Beam Epitaxy. *Scientific Reports* **2015,** *5*, 14760.

26. Vuong, T.; Cassabois, G.; Valvin, P.; Rousseau, E.; Summerfield, A.; Mellor, C.; Cho, Y.; Cheng, T.; Albar, J. D.; Eaves, L. Deep Ultraviolet Emission in Hexagonal Boron Nitride Grown by High-Temperature Molecular Beam Epitaxy. *2D Materials* **2017,** *4* (2), 021023.

27. Cho, Y.-J.; Summerfield, A.; Davies, A.; Cheng, T. S.; Smith, E. F.; Mellor, C. J.; Khlobystov, A. N.; Foxon, C. T.; Eaves, L.; Beton, P. H. Hexagonal Boron Nitride Tunnel Barriers Grown on Graphite by High Temperature Molecular Beam Epitaxy. *Scientific Reports* **2016,** *6*, 34474.

28. Zheng, R.; Khanaki, A.; Tian, H.; He, Y.; Cui, Y.; Xu, Z.; Liu, J. Precipitation Growth of Graphene under Exfoliated Hexagonal Boron Nitride to Form Heterostructures on Cobalt Substrate by Molecular Beam Epitaxy. *Applied Physics Letters* **2017,** *111* (1), 011903.

29. Pierucci, D., Zribi, J., Henck, H., Chaste, J., Silly, M.G., Bertran, F., Le Fevre, P., Gil, B., Summerfield, A., Beton, P.H. and Novikov, S.V. Van der Waals Epitaxy of Two-Dimensional Single-Layer H-BN on Graphite by Molecular Beam Epitaxy: Electronic Properties and Band Structure. *Applied Physics Letters* **2018**, *112* (25), 253102.

30. Co, Y.J., Summerfield, A., Davies, A., Cheng, T.S., Smith, E.F., Mellor, C.J., Khlobystov, A.N., Foxon, C.T., Eaves, L., Beton, P.H. and Novikov, S.V. Hexagonal Boron Nitride Tunnel Barriers Grown on Graphite by High Temperature Molecular Beam Epitaxy. *Scientific Reports* **2016**, *6*, 34474.

31. Elias, C., Valvin, P., Pelini, T., Summerfield, A., Mellor, C.J., Cheng, T.S., Eaves, L., Foxon, C.T., Beton, P.H., Novikov, S.V. and Gil, B. Direct Band-Gap Crossover in Epitaxial Monolayer Boron Nitride. *Nature Communications* **2019**, *10* (1), 1-7.

32. Caneva, S.; Weatherup, R. S.; Bayer, B. C.; Blume, R.; Cabrero-Vilatela, A.; Braeuninger-Weimer, P.; Martin, M.-B.; Wang, R.; Baehtz, C.; Schloegl, R. Controlling Catalyst Bulk Reservoir Effects for Monolayer Hexagonal Boron Nitride CVD. *Nano Letters* **2016,** *16* (2), 1250-1261.

33. Sharma, K. P.; Sharma, S.; Sharma, A. K.; Jaisi, B. P.; Kalita, G.; Tanemura, M. Edge Controlled Growth of Hexagonal Boron Nitride Crystals on Copper Foil by Atmospheric Pressure Chemical Vapor Deposition. *CrystEngComm* **2018,** *20* (5), 550-555.

34. Wood, G. E.; Marsden, A. J.; Mudd, J. J.; Walker, M.; Asensio, M.; Avila, J.; Chen, K.; Bell, G. R.; Wilson, N. R. Wan der Waals Epitaxy of Monolayer Hexagonal Boron Nitride on Copper Foil: Growth, Crystallography and Electronic Band Structure. *2D Materials* **2015,** *2* (2), 025003.

35. Khanaki, A.; Tian, H.; Xu, Z.; Zheng, R.; He, Y.; Cui, Z.; Yang, J.; Liu, J. Effect of High Carbon Incorporation in Co Substrates on the Epitaxy of Hexagonal Boron Nitride/Graphene Heterostructures. *Nanotechnology* **2017,** *29* (3), 035602.

36. Xu, Z.; Tian, H.; Khanaki, A.; Zheng, R.; Suja, M.; Liu, J. Large-Area Growth of Multi-Layer Hexagonal Boron Nitride on Polished Cobalt Foils by Plasma-Assisted Molecular Beam Epitaxy. *Scientific Reports* **2017,** *7* (1), 1-7.

37. He, Y.; Tian, H.; Khanaki, A.; Shi, W.; Tran, J.; Cui, Z.; Wei, P.; Liu, J. Large-Area Adlayer-Free Single-Layer h-BN Film Achieved by Controlling Intercalation Growth. *Applied Surface Science* **2019,** *498*, 143851.

38. Kim, S. M.; Hsu, A.; Park, M. H.; Chae, S. H.; Yun, S. J.; Lee, J. S.; Cho, D.-H.; Fang, W.; Lee, C.; Palacios, T. Synthesis of Large-area Multilayer Hexagonal Boron Nitride for High Material Performance. *Nature Communications* **2015,** *6*, 8662.

39. Uchida, Y.; Nakandakari, S.; Kawahara, K.; Yamasaki, S.; Mitsuhara, M.; Ago, H. Controlled Growth of Large-Area Uniform Multilayer Hexagonal Boron Nitride as an Effective 2D Substrate. *ACS Nano* **2018,** *12* (6), 6236-6244.

40. Caneva, S.; Weatherup, R. S.; Bayer, B. C.; Brennan, B.; Spencer, S. J.; Mingard, K.; Cabrero-Vilatela, A.; Baehtz, C.; Pollard, A. J.; Hofmann, S. Nucleation Control for Large, Single Crystalline Domains of Monolayer Hexagonal Boron Nitride via Si-Doped Fe Catalysts. *Nano Letters* **2015,** *15* (3), 1867-1875.

41. Zhuang, P.; Lin, W.; Xu, B.; Cai, W. Oxygen-Assisted Synthesis of Hexagonal Boron Nitride Films for Graphene Transistors. *Applied Physics Letters* **2017,** *111* (20), 203103.

42. Babenko, V.; Fan, Y.; Veigang-Radulescu, V.-P.; Brennan, B.; Pollard, A. J.; Burton, O.; Alexander-Webber, J. A.; Weatherup, R. S.; Canto, B.; Otto, M. Oxidising and Carburising Catalyst Conditioning for the Controlled Growth and Transfer of Large Crystal Monolayer Hexagonal Boron Nitride. *2D Materials* **2020,** *7* (2), 024005.

43. Tian, H.; Khanaki, A.; Das, P.; Zheng, R.; Cui, Z.; He, Y.; Shi, W.; Xu, Z.; Lake, R.; Liu, J. Role of Carbon Interstitials in Transition Metal Substrates on Controllable Synthesis of High-Quality Large-Area Two-Dimensional Hexagonal Boron Nitride Layers. *Nano Letters* **2018,** *18* (6), 3352-3361.

44. Lee, S. B.; Yoon, D. Y.; Hwang, N. M.; Henry, M. F. Grain Boundary Faceting and Abnormal Grain Growth in Nickel. *Metallurgical and Materials Transactions A* **2000,** *31* (3), 985-994.

45. Vollmer, M.; Arold, T.; Kriegel, M.; Klemm, V.; Degener, S.; Freudenberger, J.; Niendorf, T. Promoting Abnormal Grain Growth in Fe-Based Shape Memory Alloys Through Compositional Adjustments. *Nature Communications* **2019,** *10* (1), 1-10.

46. Brückner, W.; Weihnacht, V.; Pitschke, W.; Thomas, J.; Baunack, S. Abnormal Grain Growth of Sputtered CuNi (Mn) Thin Films. *Journal of Materials Research* **2000,** *15* (5), 1062-1068.

47. Perdew, J. P.; Burke, K.; Ernzerhof, M. Generalized Gradient Approximation Made Simple. *Physical Review Letters* **1996,** *77* (18), 3865-3868.

48. Ernzerhof, M.; Scuseria, G. E. Assessment of the Perdew–Burke–Ernzerhof Exchange-Correlation Functional. *The Journal of Chemical Physics* **1999,** *110* (11), 5029-5036.

49. Henkelman, G.; Uberuaga, B. P.; Jónsson, H. A Climbing Image Nudged Elastic Band Method for Finding Saddle Points and Minimum Energy Paths. *The Journal of Chemical Physics* **2000,** *113* (22), 9901-9904.

50. Khan, M. H.; Huang, Z.; Xiao, F.; Casillas, G.; Chen, Z.; Molino, P. J.; Liu, H. K. Synthesis of Large and few atomic layers of hexagonal boron nitride on melted copper. *Scientific Reports* **2015,** *5* (1), 1-11.

51. Li, X.; Li, Y.; Wang, Q.; Yin, J.; Li, J.; Yu, J.; Guo, W. Oxygen-Suppressed Selective Growth of Monolayer Hexagonal Boron Nitride on Copper Twin Crystals. *Nano Research* **2017,** *10* (3), 826-833.

52. Cho, H.; Park, S.; Won, D.-I.; Kang, S. O.; Pyo, S.-S.; Kim, D.-I.; Kim, S. M.; Kim, H. C.; Kim, M. J. Growth Kinetics of White Graphene (h-BN) on a Planarised Ni Foil Surface. *Scientific Reports* **2015,** *5* (1), 1-10.

53. Kadhim, N. J., and D. Mukherjee. Rate-Temperature Relation for MBE Growth of GaAs Layers. International Journal of Electronics Theoretical and Experimental 1990, 69 (5), 641-645.

54. Shaw, Don W. Influence of Substrate Temperature on GaAs Epitaxial Deposition Rates. Journal of The Electrochemical Society 1968, 115 (4), 405-408.

55. Schneider, C. A.; Rasband, W. S.; Eliceiri, K. W. NIH Image to ImageJ: 25 Years of Image Analysis. Nature Methods 2012, *9* (7), 671-675.

56. Auwärter, W.; Muntwiler, M.; Osterwalder, J.; Greber, T. Defect Lines and Two-Domain Structure of Hexagonal Boron Nitride Films on Ni (1 1 1). *Surface Science* **2003,** *545* (1-2), L735-L740.

57. Yang, Y.; Fu, Q.; Li, H.; Wei, M.; Xiao, J.; Wei, W.; Bao, X. Creating a Nanospace under an h-BN Cover for Adlayer Growth on Nickel (111). *ACS Nano* **2015,** *9* (12), 11589-11598.

58. Sun, X.; Pratt, A.; Li, Z.; Ohtomo, M.; Sakai, S.; Yamauchi, Y. The Adsorption of h-BN Monolayer on the Ni (111) Surface Studied by Density Functional Theory Calculations with a Semiempirical Long-Range Dispersion Correction. *Journal of Applied Physics* **2014,** *115* (17), 17C117.

59. Huda, M.; Kleinman, L. H-BN Monolayer Adsorption on the Ni (111) Surface: A Density Functional Study. *Physical Review B* **2006,** *74* (7), 075418.

60. Grad, G.; Blaha, P.; Schwarz, K.; Auwärter, W.; Greber, T. Density Functional Theory Investigation of the Geometric and Spintronic Structure of h-BN/Ni (111) in View of Photoemission and STM Experiments. *Physical Review B* **2003,** *68* (8), 085404.

61. Tian, H.; He, Y.; Das, P.; Cui, Z.; Shi, W.; Khanaki, A.; Lake, R. K.; Liu, J. Growth Dynamics of Millimeter-Sized Single-Crystal Hexagonal Boron Nitride Monolayers on Secondary Recrystallized Ni (100) Substrates. *Advanced Materials Interfaces* **2019,** *6* (22), 1901198.

62. Yin, S.; Xu, B.; Zhou, X.; Au, C. A Mini-Review on Ammonia Decomposition Catalysts for On-Site Generation of Hydrogen for Fuel Cell Applications. *Applied Catalysis A: General* **2004**, 277 (1-2), 1-9.

63. Arenal, R.; Ferrari, A.; Reich, S.; Wirtz, L.; Mevellec, J.-Y.; Lefrant, S.; Rubio, A.; Loiseau, A. Raman Spectroscopy of Single-Wall Boron Nitride Nanotubes. *Nano Letters* **2006,** *6* (8), 1812-1816.

64. Simmons, J. G. Generalized Formula for the Electric Tunnel Effect Between Similar Electrodes Separated by a Thin Insulating Film. *Journal of applied physics* **1963,** *34* (6), 1793-1803.

65. Jiang, L.; Shi, Y.; Hui, F.; Tang, K.; Wu, Q.; Pan, C.; Jing, X.; Uppal, H.; Palumbo, F.; Lu, G. Dielectric Breakdown in Chemical Vapor Deposited Hexagonal Boron Nitride. *ACS Applied Materials & Interfaces* **2017,** *9* (45), 39758-39770.

66. Simmons, J. G. Generalized Thermal J-V Characteristic for the Electric Tunnel Effect. *Journal of Applied Physics* **1964,** *35* (9), 2655-2658.

67. Cui, Z.; He, Y.; Tian, H.; Khanaki, A.; Xu, L.; Shi, W.; Liu, J. Study of Direct Tunneling and Dielectric Breakdown in Molecular Beam Epitaxial Hexagonal Boron Nitride Monolayers Using Metal-Insulator-Metal Devices. *ACS Applied Electronic Materials* **2020,** *2* (3), 747-755.

68. Lee, G.-H.; Yu, Y.-J.; Lee, C.; Dean, C.; Shepard, K. L.; Kim, P.; Hone, J. Electron Tunneling through Atomically Flat and Ultrathin Hexagonal Boron Nitride. *Applied Physics Letters* **2011,** *99* (24), 243114.

69. Dodson, B. *Weibull analysis*, Asq Press: **1994**.

Chapter 4: Robust Nano Capacitors based on Wafer-Scale Single-Crystal Hexagonal Boron Nitride Monolayer Films

4.1 Introduction

Two-dimensional (2D) h-BN materials and their applications in vast areas have been at the forefront of 2D materials research for the last two decades. Its wide bandgap (5.9 eV), high breakdown electric field (12 MV/cm),[1] and dangling bond free surface render it a perfect insulating layer especially for van der Waals (vdW) devices. Exfoliated h-BN flakes have been widely used in tunneling devices, field effect transistors, and capacitors.[2-4] In contrast, h-BN films obtained from bottom-up synthesis such as chemical vapor deposition (CVD) and molecular beam epitaxy (MBE) possess larger defect density compared to exfoliated single-crystal flakes. The defects in h-BN films, such as grain boundaries, have been utilized in resistive switching memory devices[5, 6] and are also promising for single photon emitter devices.[7] However, when its insulating properties are needed, h-BN films with a larger density of defects would exhibit large leakage current, which essentially degrades the performance of the devices. Thus, it is critical to enhance the quality of the h-BN films for these applications.

One way to reduce and diminish the defect density is to grow high-quality single-crystal h-BN films. Song et al. achieved the growth of wafer-scale single-crystal h-BN films by utilizing the self-collimation of h-BN flakes on melted Au surface.[8] Wang et al. adopted another method, step edge enhanced epitaxy, by taking the advantage of step edges on a Cu (110) surface.[9] Similarly, Chen et al. reported the step edge enhanced epitaxial growth

of wafer-scale single-crystal h-BN on single-crystal Cu (111) substrate.[10] However, such methods to obtain single-crystal metal substrates for h-BN growth are rather sophisticated. In the case of using metal films obtained from deposition as substrates, desorption and surface pitting during annealing were observed.[11, 12] Another issue is that even though wafer-scale single-crystal h-BN films were reported, electrical devices were rarely fabricated. Chen et al. reported that the metal-insulator-metal (MIM) devices comprising (Ti/h-BN/Cu) layers on polycrystal monolayer h-BN films are almost conductive, while those on single-crystal monolayer h-BN films have small breakdown voltage at 0.1 V.[10] In contrast, the breakdown voltage of MIM devices with Ni and Co as electrodes on our MBE grown monolayer h-BN films is around 0.8 V, indicating higher film quality.[13-15] One issue in these h-BN samples is the long growth time required to obtain continuous h-BN film, which is not efficient.

The second way to ensure the quality of the h-BN film is to minimize the process induced defects during device fabrication. 'High-energy' atoms or clusters evaporated from hot metal surface in vacuum chamber for metal contacts to the material has been known to damage the targeted surfaces by physical bombardment or strong local heating.[16, 17] For multilayer films a few damages on the surface layer may not become an issue,[18, 19] but for single-layer films, the same damages can cause the entire films to be leaky electrically. Efforts have been made to address this problem. For example, to prevent damage of MoS_2 from heavy transition metal, Kim et al employed low-thermal-energy evaporation deposition of indium,[20] and Liu et al replaced metal deposition with the electrode transfer

technique.[17] In the fabrication of molecular electronic devices, an indirect deposition technique was adopted to avoid damage from direct atomic beams.[21, 22]

The work presented in this article aims to address the problems mentioned above. Many methods such as MBE,[23] CVD,[24] atomic layer deposition,[25] and solution processed fabrication[26, 27] have been adopted to obtain large area h-BN films. Among these tools, MBE with precise control of growth parameters is an excellent candidate for epitaxial growth of high-quality films with atomic-layer thicknesses, thus it is employed for h-BN growth in this project. Single-crystal substrates were obtained simply by thermal annealing of Ni foils. Different to thin metal films obtained by metal deposition techniques, post annealed Ni foils can be further polished to keep the metal surface fresh and flat. By replacing mechanical polishing with electropolishing in this effort, we discovered that the h-BN nucleation density and the growth speed are drastically increased. Robust nano capacitors were fabricated on as grown h-BN films using "low-energy" Al atoms from a Temescal BJD 1800 e-beam evaporator to mitigate the process induced damage effects on the films. The growth mechanism and film quality were also studied with scanning electron microscopy (SEM), scanning tunneling microscopy (STM), reflection high-energy electron diffraction (RHEED), atomic force microscopy (AFM), X-ray photoelectron spectroscopy (XPS), Raman spectroscopy, and ultraviolet-visible absorption spectroscopy (UV-Vis). The 'effective distance' between two electrodes was extracted from capacitance analysis. Tunneling currents were measured and analyzed.

4.2 Experimental Details

4.2.1 Growth and Characterization

A Perkin-Elmer MBE system with a background pressure of ~10^{-9} Torr was employed for h-BN growth. B_2O_3 powder (Alfa Aesar, 99.999% purity) was used as the B source, and the effusion cell temperature was kept at 1170 °C. Ammonia gas (American Gas Group, 99.9995% purity) was used as N source, and the flow rate was kept at 10 sccm. The substrate temperature for time dependent growth was kept at 867 °C. Secondary electron SEM images and electron backscattered diffraction (EBSD) images were acquired using a FEI NNS450 system. X-ray diffraction (XRD) spectra were acquired using a Panalytical Empyrean Series 2 system and the XPS spectra were acquired using a Kratos AXIS ULTRA XPS system. The Raman spectra was obtained using a HORIBA LabRam system equipped with a 60-mW, 532-nm green laser. AFM images were acquired using a tapping mode Veeco D5000 AFM system, and STM images were acquired using a tabletop NanoSTM. Please refer to our previous research for more information about the MBE growth procedures.[28, 29] The RHEED experiment is carried out using 15 keV electron beam with 7.5 mW beam energy.

4.2.2 Device Fabrication and Characterization

The capacitors were fabricated following photolithography, metal deposition, and lift-off patterning. Metal contacts were deposited with an e-beam evaporator where a 20-nm thick Al layer was deposited at a rate of 0.2 Å/s, and a 100-nm thick Au layer was deposited at a rate of 1 Å/s. Electrical characterization of the devices was performed on a Signatone

probe station, and the I-V measurements were acquired using an Agilent 4155C semiconductor parameter analyzer. Finally, C-V and C-f measurements were acquired using a Keysight E4980A precision LCR meter.

4.3 Results and Discussion

4.3.1 Single crystal substrate and electropolish

a

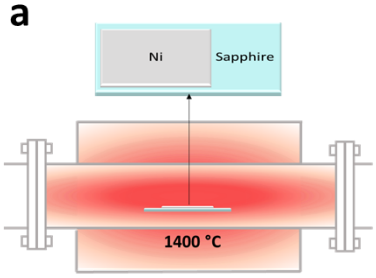

b

Gas	Ar: 200 sccm H_2: 200 sccm
Pressure	500 Torr
Temperature	1400°C
Time	90 min

c

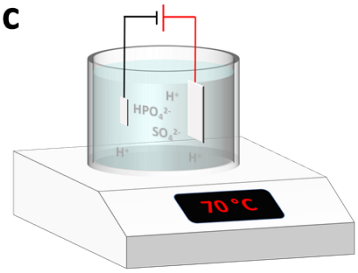

d

Electrolyte	H_2O: H_2SO_4: H_3PO_4 3:4:7
Current Density	0.5 A/cm^2
Temperature	70 °C
Time	2 min

Figure 4.1. Substrate preparation procedure. (a) Schematic of high temperature annealing process; (b) parameters used in anneal process; (c) schematic of electropolishing process; (d) parameter used in electropolishing process.

Figure 4.1 summarizes the key parameters in substrate preparation procedure. As received polycrystal Ni foil (Alfa Aesar, 99.994%) was cut into 1 in^2 pieces and loaded in the ceramic tube furnace with c-sapphire as the support. The ceramic tube is filled with Ar and H_2 gas and the gas flow rate is 200 sccm for each. The pressure is controlled at 500 Torr by a partial valve. The substrate was then annealed at 1400°C for 90 mins to obtain

the single crystal substrate with (111) surface. Noting that the purity of the Ni foil matters a lot. Foil with low purity would end up with polycrystal substrate. After annealing, the substrates were treated with electropolishing. The mechanism of electropolishing was thoroughly studied and reported elsewhere.[30, 31] The electrolyte we used is a mixture of DI water, sulfuric acid (96%), phosphoric acid (85%) in the ratio of 3:4:7. The substrate is connected to the anode of the DC power supply, and the counter electrode is a piece of as received Ni foil. During electropolishing, the current density on metal surface is controlled at around 0.5 A/cm^2. In other words, for the 1 in^2 substrate, the current is around 6 A. Smaller current would result in pits on the surface because the gas bubble formed on the surface cannot be released in time, while larger current would result in the groves (bubble trace) on the surface. The temperature is kept around 70 °C to promote the dissolution of Ni ions while maintaining the viscous layer on the surface. It takes two minutes to polish 1 piece of substrate. After electropolishing, the substrate was rinsed in DI water to remove the acid.

Figure 4.2a shows a photograph of a post-annealed 1-in^2 single-crystal substrate. There is a very small portion of polycrystal remaining at the lower left corner. Figures 4.2 b and c show EBSD and XRD results, respectively. The blue color of the Z-direction inverse pole figure (IPF Z) and the diffraction peaks of XRD at 44.6° and 98.6° indicate that the surface orientation is (111). Figures 4.2 d and e show the photos of substrates before and after electropolishing, respectively, demonstrating that the substrate surface after electropolishing is much smoother and cleaner. Figure 4.2f shows AFM and STM images of an electropolished substrate surface, where the root mean square (RMS) roughness from

a 10-um^2 area is 0.5 nm. The STM image reveals that the nanoscale terraces and pits are formed on metal surface after electro-chemical reaction.

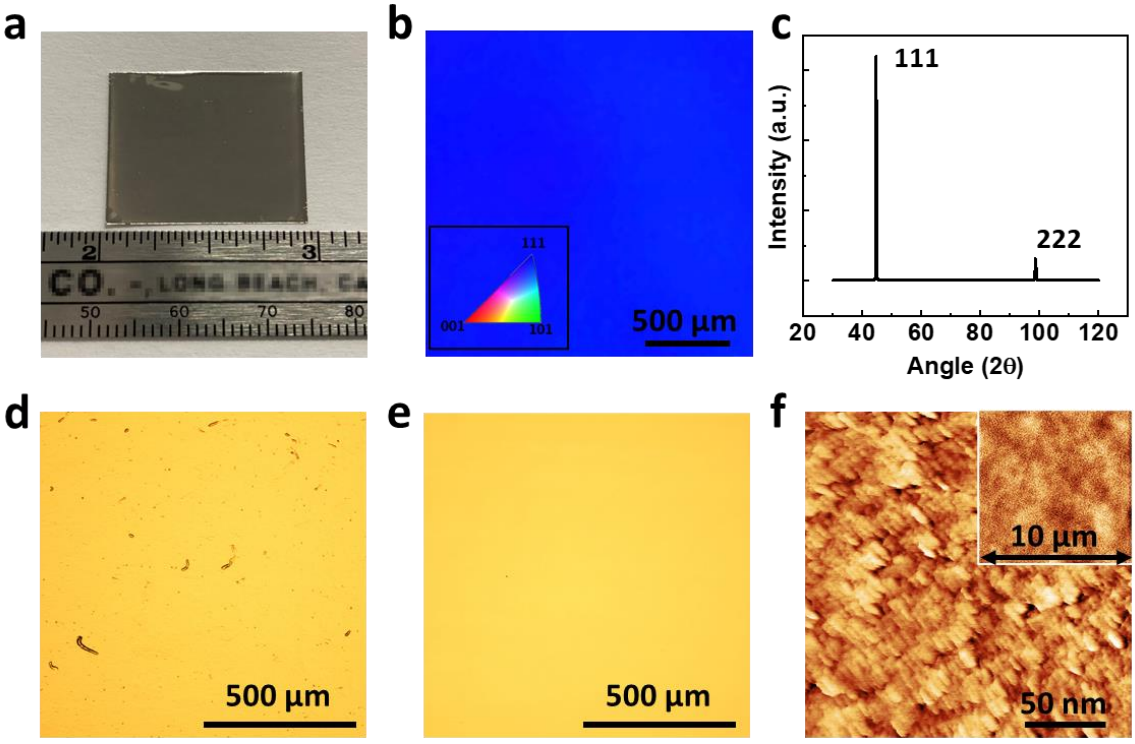

Figure 4.2. Characterization of Ni (111) substrate. (a) Photo of 1 in^2 single crystal substrate obtained after thermal anneal; (b) EBSD IPF Z image showing (111) surface direction; (c) XRD result showing (111) surface direction; (d) photo of substrate before electropolishing; (e) photo of substrate after electropolishing; (f) STM and AFM (inset) images of substrate surface after electropolishing.

The XPS analysis was carried out to understand the chemical reaction of three different substrates. Figure 4.3 shows the B_1s, N_1s, S_1s, P_1s, and O_1s XPS results on mechanically polished (M-P) substrate, electropolished (E-P) substrate, and E-P substrate after h-BN growth. The substrates were first polished, then etched with diluted HCl solution (10%, 1 min), rinsed with DI water, and blown dry with compressed N_2 gas. The h-BN sample is a continuous film grown with the same condition used in the main

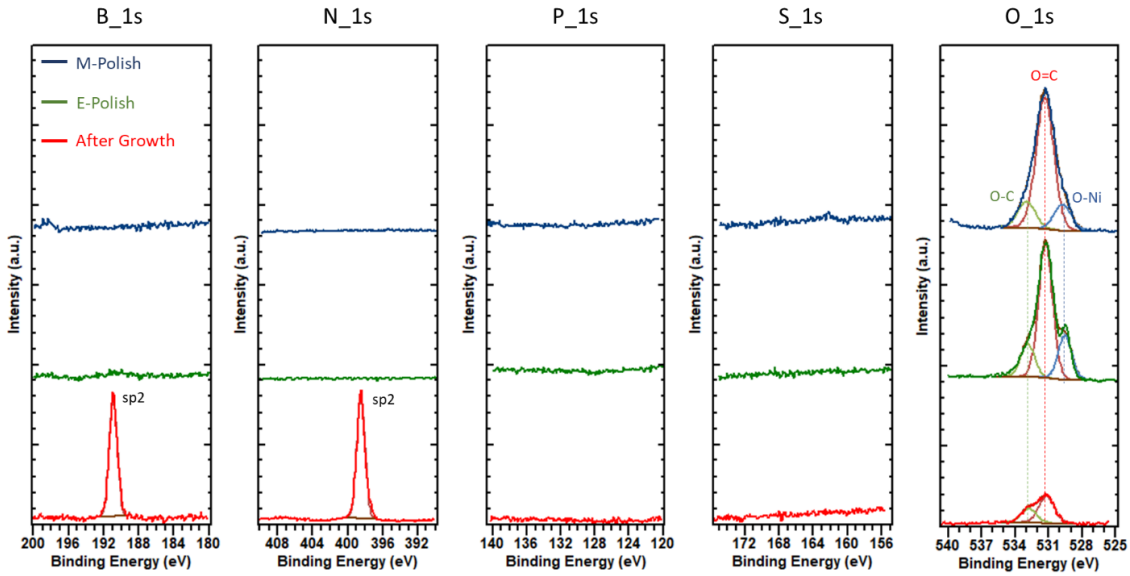

Figure 4.3. XPS results obtained on mechanically polished substrate, electropolished substrate, and sample after h-BN growth.

manuscript. The ex-situ XPS was done two days after the sample was grown. The XPS results are deconvoluted and fitted with CasaXPS and Shirley background. No P- or S-related peaks are observed, indicating that the E-P substrate is not contaminated by electrolyte. Strong oxygen peaks appear on both M-P and E-P substrates, each of them can be deconvoluted into three peaks with GL(30) line shape and identical FWHM. The peaks at 533.0 eV and 531.4 eV are assigned to O-C and O=C, respectively, which are due to the adventitious oxygen absorption commonly observed on samples being exposed to air. The peak at 529.7 eV is assigned to O-Ni peak, indicating that the metal surface is slightly oxidized after being exposed to air. The E-P substrate exhibits stronger O-Ni peak, indicating that the E-P substrate is more easily oxidized, which may provide the evidence that E-P substrate is more chemically reactive. Strong B and N peaks appear on E-P substrate after h-BN growth. Each of them can be fitted well with one symmetric peak (GL(0)) at 190.7 eV and 398.3 eV, respectively, indicating the high-quality sp^2 structure.

On h-BN covered surface, the adventitious oxygen peak is relatively weak, and no metal oxide related peaks are observed.

4.3.2 Growth and characterization of single crystal film

Figures 4.4 a-d show SEM images of samples after 10-min, 20-min, 30-min, and 40-min growth, respectively. Continuous films have been observed to form after 40-min growth. Figure 4.4e shows the h-BN coverage versus growth time. Our recent article reported on the h-BN growth on mechanically polished Ni (111) substrates under similar growth conditions.[14] We have discovered that the growth speed on electropolished substrates is nearly 20 times faster compared to growth on mechanically polished substrates.[14] The reason for this dramatic improvement could be the availability of many more h-BN nucleation sites obtained via electropolishing. As shown in Figure 4.2f, the nanoscale protrusions and pits formed by electro-chemical reactions may evolve into favorable h-BN nucleation sites at the growth temperatures. The time-dependent growth results reveal that the h-BN flakes are well aligned before merging, indicating a strong epitaxial growth relationship between h-BN and the Ni (111) surface. Figure 4.4f provides a summary of edge direction distribution of h-BN flakes on the sample shown in Figure 4.4b. Three major peaks are separated by 60°, confirming a good level of unidirectionality of h-BN flakes, which has been considered to be the key to achieve high quality single crystal films.[9, 10] This strongly suggests that the continuous film shown in Figure 4.4d has a single crystal structure.

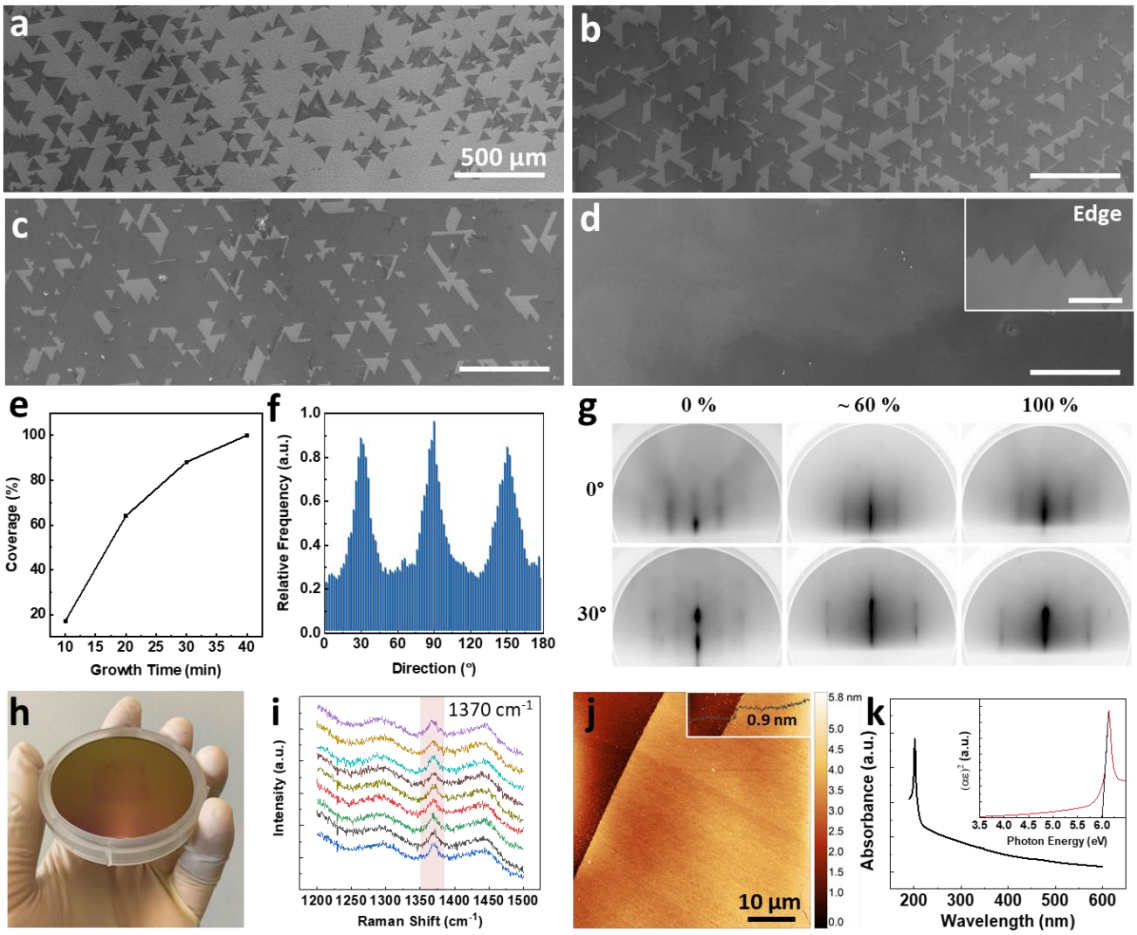

Figure 4.4. Characterization of h-BN grown on Ni (111) single-crystal substrate. (a-d) SEM images of h-BN after growth for 10 min, 20 min, 30 min, and 40 min, respectively; an inset in d is the image of the sample at the edge area. All scale bars are 500 µm; (e) coverage of h-BN versus growth time; (f) edge direction analysis of sample shown in (b); (g) h-BN coverage dependent RHEED analysis; (h) photo of h-BN film transferred on a 2-inch SiO_2/Si wafer; (i) Raman spectra taken on 9 different areas on transferred sample shown in (h); (j) AFM image taken on transferred sample shown in (h); inset is a linear scan profile across the edge; (k) UV–Vis absorption spectrum of a transferred h-BN sample on sapphire. The inset is a Tauc plot.

The epitaxial relationship was studied using an h-BN coverage dependent RHEED analysis, as shown in Figure 4.4g. The RHEED patterns were obtained on samples with 0% (Ni substrate after annealing), 60% (sample shown in Figure 4.4b), and 100% (sample shown in Figure 4.4d) h-BN coverage. Only two set of patterns were observed, and they

were separated by 30°. The row labeled by 0° corresponds to the <$1\bar{1}0$> directions, and the row labeled as 30° corresponds to the <$11\bar{2}$> directions. The lattice constants calculated based on the RHEED patterns are ~4.37 Å for the <$1\bar{1}0$> directions, and ~2.52 Å for the <$11\bar{2}$> directions. No differences in lattice constants have been resolved between Ni (111) and h-BN. The RHEED patterns for Ni (111) substrate are slightly dotty, which is attributed to oxidation after being exposed to air.[32] In addition, due to the surface corrugations after h-BN film growth,[14] the RHEED patterns obtained on h-BN films are also fainted. Nevertheless, the coverage dependent RHEED analysis confirms that there is no in-plane rotation between h-BN and Ni (111) surface, further indicated by theoretical calculations.[33, 34]

Figure 4.4h shows a photograph of a single-crystal h-BN film transferred onto a 2-inch diameter SiO_2/Si wafer. The detailed transfer process is available in our previous report.[35] The Raman spectra in Figure 4.4i are obtained from 9 different spots on the transferred h-BN film. The h-BN peaks are located at around 1370 cm^{-1}, indicating a uniform single-layer h-BN film.[36] The other two peaks at 1293 cm^{-1} and 1445 cm^{-1} are from SiO_2/Si substrate.[37] The film thickness was further confirmed by AFM imaging, as shown in Figure 4.4j. The 50×50 μm^2 AFM image shows a clean and flat h-BN film after the transfer process. The film thickness obtained from a line profile scan at the film edge (see the inset) is around ~0.9 nm. This larger value compared to theoretical thickness (0.33 nm) is a result of AFM cantilever tip effects including trapped water and gas molecules at the tip-surface interface.[38] Figure 4.4k shows a UV–Vis absorption spectrum and a corresponding Tauc plot (assuming a direct band gap[39]) acquired from an h-BN film transferred onto a sapphire

substrate. A strong peak with a sharp absorption edge has been observed at 202 nm, corresponding to a band gap of around 6.03 eV as extracted from the Tauc plot.

4.3.3 Analysis of crystallinity and growth orientation

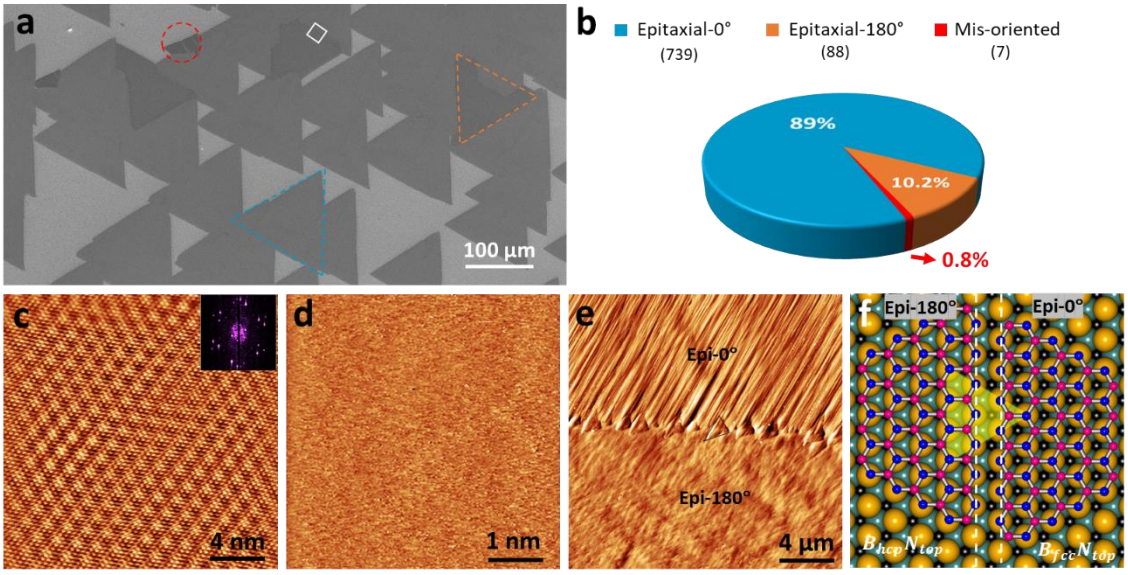

Figure 4.5. Analysis of h-BN growth orientations. (a) SEM image of h-BN flakes with different growth orientations. The blue and orange triangles, and purple circles mark the epitaxial-0°, epitaxial-180°, and mis-oriented h-BN flakes, respectively; (b) statistical analysis of h-BN flakes with three different growth orientations; (c) STM image taken on mis-oriented h-BN flake; (d) STM image taken on epitaxial-0° flake; the inset shows the pattern after FFT transformation; (e) AFM image taken on the grain boundary between epitaxial-0° and epitaxial-180° flakes as marked with the white square in (a); and (f) atomic model of proposed configuration of the grain boundary.

Figure 4.5 provides a summary of data of growth directions of h-BN flakes. Three different growth directions have been observed, as marked in the SEM image in Figure 4.5a. The blue triangle marks an h-BN flake in the dominant growth direction designated as epitaxial-0°; the orange triangle marks an h-BN flake in the second preferable growth direction designated as epitaxial-180°; and the red circle marks an h-BN flake which is misoriented. A statistical analysis of the three growth directions is summarized in Figure

4.5b. 89% of the h-BN flakes have been grown in the epitaxial-0° direction, about 10.2% percent of the h-BN flakes have been grown in the epitaxial-180° direction, and only about 0.8% of the h-BN flakes have been misoriented. According to theoretical[10, 34] and experimental[40] results, the epitaxial-0° orientation has the $B_{fcc}N_{top}$ configuration, and the epitaxial-180° orientation has the $B_{hcp}N_{top}$ configuration. The misoriented h-BN flakes are only observed around crystal defect sites or impurities over substrate surfaces. Figure 4.5 c and d show STM images taken on misoriented and epitaxial h-BN flakes, respectively. Moiré patterns have been obtained from misoriented flakes, while no features were resolved on epitaxial flakes. Note that the STM employed is a tabletop instrument, which can only be operated at room temperature and in the ambient environment, and the scanning tips are made from plier-cut Pt-Ir wires. Therefore, lateral and vertical resolutions are not as good to resolve the B or N atoms. Nevertheless, the relatively large features of the Moiré pattern on the misoriented flakes can be easily resolved. This result also confirms that there is no in-plane rotation between the epitaxial h-BN flakes and the Ni (111) surface. Figure 4.5e shows AFM images taken on the grain boundary between epitaxial-0° and epitaxial-180° h-BN flakes, as marked by the white square in Figure 4.5a. As seen from the images, surface morphologies under epitaxial-0° and epitaxial-180° flakes are different: the surface under epitaxial-0° flakes is corrugated, while the surface under epitaxial-180° flakes is relatively flat. This difference in morphologies might have been caused by the different epitaxial relationships,[41] and leads to different gray scale contrast in the SEM image. The corrugated surface has a larger surface-to-volume ratio, therefore many more secondary electrons have been generated, and in turn, the epitaxial-0° flakes look brighter than the

epitaxial-180° flakes. Small h-BN adlayers are formed along the grain boundary, as marked by the black triangle, which is attributed to the intercalation growth at line defects.[34] Figure 4.5f shows a proposed atomic model at the grain boundary by assuming that all triangular h-BN flakes have N-terminated zigzag edges and N will always sit on the top site.[42] When epitaxial-0° and epitaxial-180° h-BN flakes meet, a mismatch region is formed. According to the theoretical calculation,[43] instead of forming stable line defects, this type of mismatch will lead to a transition region, which opens up a channel for intercalation growth of h-BN adlayers. The yellow triangle illustrates the h-BN adlayers at the interface as observed in Figure 4.5e. The intercalated h-BN adlayers patch up the line defects, ensuring the insulating character of the h-BN film.

Figure 4.6 further illustrates the growth mechanism of h-BN on E-P substrates. Figure 4.6a shows a SEM image of dense h-BN nuclei observed in-between large h-BN flakes. Considering the low solubility of B (~0.3 at.% at 1085 °C [44]) and N (~0.004 at.% at 1550 °C [45]) in Ni, the nuclei cannot be formed through precipitation during substrate cooling period. Therefore, they should have existed on the surface during growth. Thereby, they can contribute to the fast growth speed by merging with expanding flakes. Figure 4.6 b and c show dark field optical microscope image and AFM image of h-BN nuclei after being transferred onto SiO_2/Si substrate, respectively. The AFM image shows that the nuclei have dendritic edges, which usually appear when edge diffusion is inefficient and may be related to the presence of hydrogen atoms.[46] The presence of dense nuclei indicates that the nucleation sites are abundant on the electropolished surface, while they are absent on mechanically polished substrate.

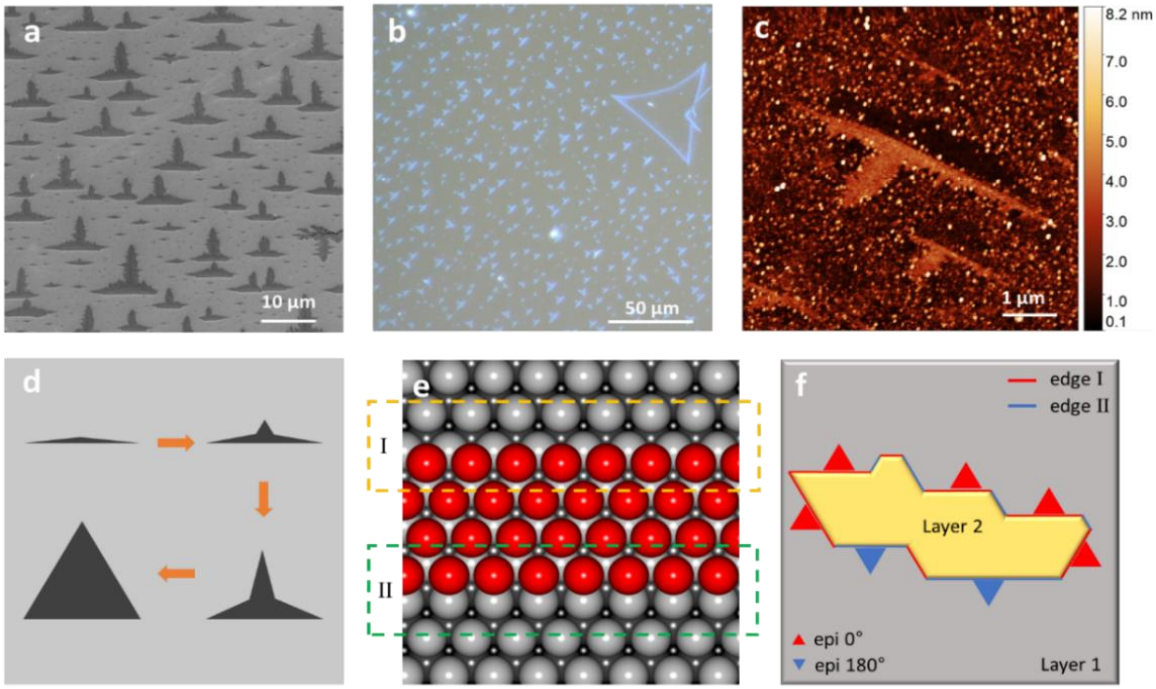

Figure 4.6. H-BN nuclei on Ni (111) surface. (a) SEM image of h-BN nuclei; (b) dark-field optical microscope image of h-BN nuclei after being transferred onto SiO_2/Si substrate; (c) AFM image of h-BN nuclei after being transferred onto SiO_2/Si substrate; (d) schematic of evolution of h-BN nuclei with the increase of size; (e) schematic of two types of step edges on Ni (111) surface; (f) schematic of growth scenario of epi-0° and epi-180° nuclei.

The typical evolution of h-BN nuclei as they grow larger is shown in Figure 4.6d. The "T" shape of nuclei is attributed to the faster growth speed along and perpendicular to the atomic steps on the substrate. As the nuclei grow larger, it is rounded to triangular shape driven by the tendency for lowest free energy.[47] The "T" shaped nuclei mainly face in one direction, which is attributed to the direction of the atomic steps. As shown in Figure 4.6e, there are two types of steps on Ni (111) surfaces, labeled as type-I and type-II. According to DFT calculations, type-I edge is energetically more favorable for h-BN growth,[10] which results in the growth scenario illustrated in Figure 4.6f. The gray layer represents layer 1,

and the yellow layer represents layer 2. Type-I steps are colored in red, and type-II steps are colored in blue. The type-I and type-II edges are anti-parallel or intersect with a 120° corner. The red triangles represent the epi-0° flakes, and blue triangles represent the epi-180° flakes, respectively. Because edge-I is more energetically favorable for h-BN nucleation, there are more epi-0° flakes than epi-180° flakes.[10]

4.3.4 Characterization of nano capacitors

Figure 4.7 shows the electrical characterization results obtained from nano capacitors fabricated on single-crystal h-BN films. A schematic of the capacitor structure is shown in Figure 4.7a, where the bottom electrode is the Ni (111) substrate. The top electrodes are square shaped metal contacts fabricated by conventional photolithography and e-beam evaporation, which consist of 20-nm thick Al and 100-nm thick Au layers. The rationale of choosing Al as top contact is as follows: as mentioned in the introduction section, h-BN films can be damaged by 'high-energy' atoms evaporated from a hot metal surface. Since the energy possessed by evaporated atoms or a cluster is mainly from e-beam thermal heating, one way to diminish the damage on a target surface is to cool the hot atoms. Al can reach a high vapor pressure at a very low temperature of 821 °C under 10^{-6} Torr. In comparison, it takes Pt to reach 1492 °C, Ti to reach 1235 °C, and Ni to reach 1072 °C to attain the same vapor pressure (from Kurt J. Lesker, Inc). Overall, evaporated Al atoms possess less energy at the same deposition rate. Furthermore, energy stored in the excitation states of commonly used heavy transition metals can be converted into kinetic energy upon reaching the surface, which possess much higher energy compared to lighter Al atoms.[48] As mentioned in the introduction section, similar strategy has been reported recently, where

low-thermal-energy evaporation deposition of indium is employed to avoid damaging MoS_2 film.[20]

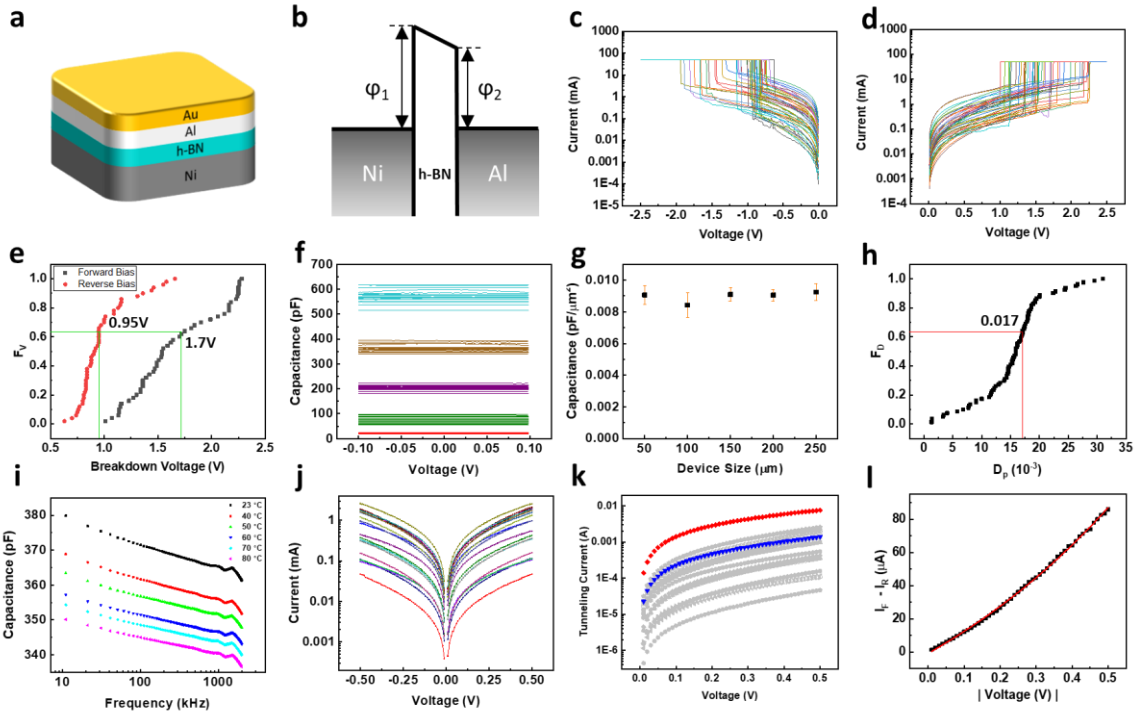

Figure 4.7. Characterization of nano capacitors fabricated on single-crystal h-BN film. (a) Model of capacitor's structure; (b) energy band diagram of the capacitor at thermal equilibrium; (c) reverse I-V characteristics on 50 capacitors with the sweeping voltage reaching -2.5 V; (d) forward I-V characteristics on 50 capacitors with the sweeping voltage reaching 2.5 V; (e) cumulative probability distribution of breakdown voltages; (f) C-V characteristics at 1 MHz of 100 capacitors with size of 50×50, 100×100, 150×150, 200×200, 250×250 μm^2; (g) specific capacitance for capacitors with each size; (h) cumulative probability distribution of dissipation factor of C-V results shown in (f); (i) temperature dependent frequency dependent capacitance of a capacitor with a size of 200×200 μm^2; (j) tunneling currents on 20 capacitors with size of 200×200 μm^2; (k) tunneling current with the calculated results colored in red (hole tunneling) and blue (electron tunneling) and experimental results colored in gray; (l) plot of forward current minus reverse current (i_F - i_R) versus |voltage|.

Figure 4.7b shows the energy band diagram of capacitors at equilibrium, where φ_1 and φ_2 are the barrier heights of Ni/h-BN and Al/h-BN junctions, respectively. Due to the difference in work function between Ni and Al, φ_1 is about 1 eV larger than φ_2

theoretically,[49] which results in a built-in potential across the h-BN layer. For convenience, the electrical characteristic will be described as 'forward' when Ni is positively biased, and as 'reverse' when Al is positively biased. Figure 4.7c shows the reverse I-V characteristics on 50 capacitors with the sweeping voltage reaching -2.5 V. Figure 4.7d shows the forward I-V characteristics on 50 capacitors with the sweeping voltage reaching 2.5 V. The cumulative probability distribution of forward and reserve breakdown voltages is summarized in Figure 4.7e. By setting the probability to 0.63 according to Weibull distribution,[50] we estimate the characteristic forward and reverse breakdown voltages to be 1.7 V, and 0.95 V, respectively, and the difference (0.85 V) is attributed to the built-in voltage at equilibrium.

Figure 4.7f shows C-V characteristics of 100 capacitors with different sizes. The C-V measurement was done with Agilent E4980A precision LCR meter in the Cp-D mode at a frequency of 1 MHz, and the sweep range is from -0.1 V to 0.1 V. Before measurement, the system is open/short corrected. Overall, the average capacitance value for different sizes is ~23 pF for devices with 50×50 μm^2 (red), ~90 pF for devices with 100×100 μm^2 (green), ~210 pF for devices with 150×150 μm^2 (purple), ~363 pF for devices with 200×200 μm^2 (brown), and ~580 pF for devices with 250×250 μm^2 (blue). No discernable changes of capacitance are observed within the sweeping range. The specific capacitances of devices with all sizes are summarized in Figure 4.7g, and the average value is estimated to be 0.009 pF/μm^2. The cumulative probability distribution of average dissipation factor of the devices is shown in Figure 4.7h. The characteristic value at probability of 0.63 is 0.017. The dissipation factor shows no apparent relationship with voltage and device size

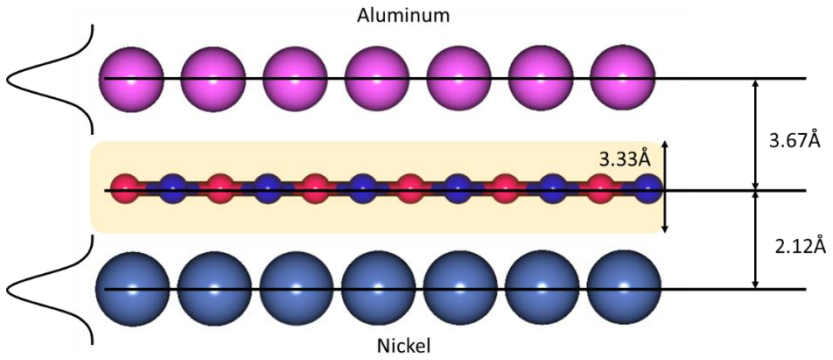

Figure 4.8. Atomic scale configuration of an ideal capacitor with monolayer h-BN as dielectric.

within the measured range. The geometric configuration of the capacitor based on monolayer h-BN is shown in Figure 4.8. Due to the van der Waals interaction, an interface space exists between h-BN and metal electrodes, which is confirmed by both experimental[51, 52] and theoretical[53] results. The h-BN/Ni separation is 2.12 Å and h-BN/Al separation is 3.67 Å.[53] The charge density at the interface when bias is applied is illustrate by the profiles on the left-hand side of the figure, which are assumed to be centered at the middle of surface layer metal atoms.[54] Therefore, the geometric distance between two electrodes can be estimated to be 5.79 Å, which consists of 3.33 Å of h-BN (ε_r = 3.29 [37,55]) and 2.46 Å of a low-permittivity layer (ε_r = 1). The geometric capacitance (C_g) is the series capacitance of the h-BN and low-permittivity layer, which can be calculated based on the following equation:

$$C = \frac{\varepsilon_0 \varepsilon_r S}{d}, \quad (1)$$

where ε_0 is the permittivity of free space, ε_r is the relative permittivity, S is the device area, and d is the dielectric thickness. The calculated geometric capacitance is 0.025 pF/μm^2. As

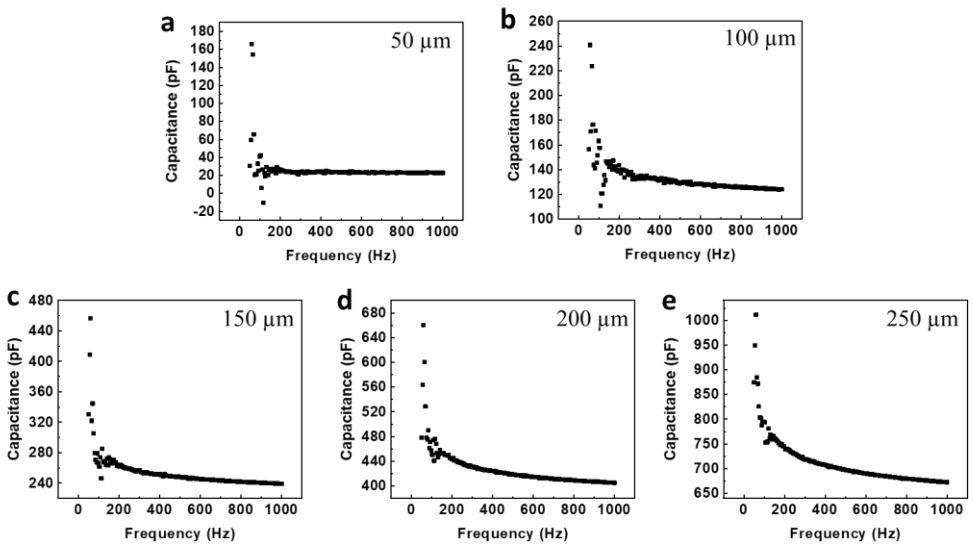

Figure 4.9 Low-frequency C-f characterization result for capacitors with different sizes: (a) 50×50 μm^2; (b) 100×100 μm^2; (c) 150×150 μm^2; (d) 200×200 μm^2; (e) 250×250 μm^2.

a result, the measured capacitance at 1 MHz is only 36% of the geometric capacitance. Similar phenomenon was observed in capacitors fabricated with ferroelectric dielectric materials, which is attributed to the low permittivity 'dead layer' formed at the ferroelectric-metal interface.[56, 57] This low permittivity 'dead layer' is related to the intrinsic properties of the bulky ferroelectric materials, thus should not be the reason of our case. To clarify this issue, we noted that for normal capacitors with thick dielectric materials, the contribution of quantum effects and uneven interfacial distance to the total capacitance is negligible. However, when the dielectric thickness goes down to the nanometer scale, their contribution should be considered.[58, 59] The quantum capacitance (C_q) and "vacuum layer" capacitance (C_v) are considered in series with the geometric capacitance. Therefore:

$$\frac{1}{C_m} = \frac{1}{C_g} + \frac{1}{C_q} + \frac{1}{C_v}. \quad (2)$$

To eliminate the decrease of measured capacitance caused by dielectric dispersion, the C_m used here is the average capacitance obtained at 200 Hz. Figure 4.9 summarizes the low-frequency (50 – 1000 Hz) C-f characterization results of 5 capacitors with different sizes. The capacitance is unstable at frequency below 200 Hz, which is attribute to the system error. The specific capacitance at 200 Hz is around 0.012 pF/μm^2. The quantum capacitance is caused by penetration of the electric field into to the electrodes and a decrease of electron energy states at metal surface, the so-called Thomas–Fermi screening effect. The quantum capacitance is defined as:[58]

$$C_q = \frac{\varepsilon_m S}{2.3L}, \tag{3}$$

where $L = \left(\frac{\varepsilon_m E_f}{2n_0 e^2}\right)^{1/2}$ is the Debye length; ε_m is the permittivity of metal, which equals the permittivity of free space (ε_0); E_f is the Fermi energy, and n_0 is the free electron density. Using the parameters of Al (n_0 = 18.1×10^{28} m^{-3}, E_f = 11.7 eV [60]), we can get L = 0.042 nm. The calculation based on Ni yields a similar result. However, due to the lower atomic density of deposited metal films, the free electron density might be lower on the Al side. Similarly, considering the large amount of B dissolved into the substrate during growth, the free electron density might also be reduced on the Ni side. Therefore, the actual value of L might be larger than 0.042 nm. For quantitative analysis, we chose the commonly recommended value for the Debye length, 0.05 nm,[58] and based on this value, the quantum capacitance C_q is 0.077 pF/μm^2. Substituting C_m, C_g, and C_q into equation (2) yields the vacuum capacitance C_v of 0.033 pF/μm^2, and the corresponding effective vacuum layer thickness calculated based on equation (1) is 2.68 Å. The vacuum layer can be attributed

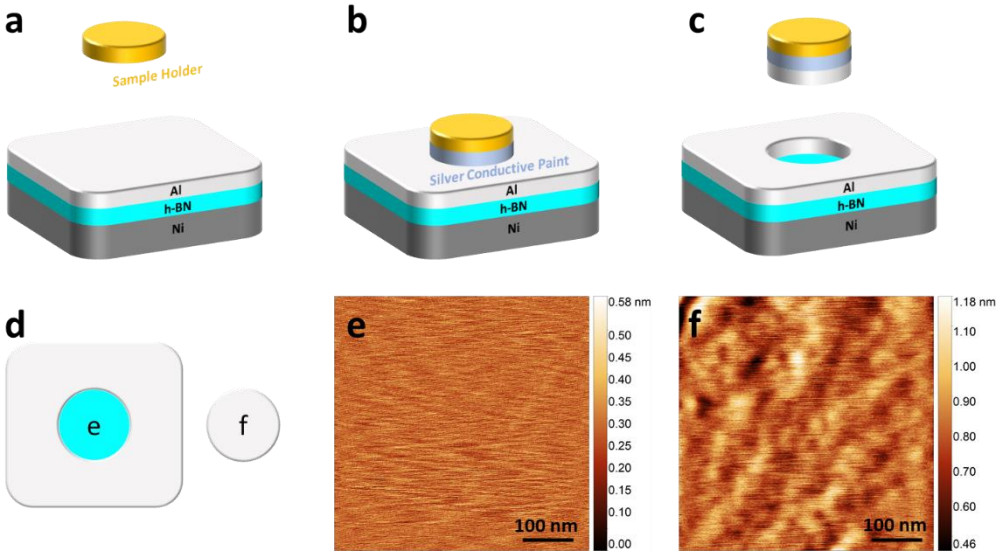

Figure 4.10. Characterization of Al/h-BN interface morphology. (a-d) Sample preparation procedure; (e) AFM image acquired on h-BN surface; (f) AFM image acquired on corresponding Al surface.

to the corrugations of h-BN film,[61, 62] metal substrate surface reconstruction,[14, 41] and crystallographic defects on metal contacts such as grain boundaries, atomic steps, and dislocations. The interface of Al/h-BN stack was characterized using AFM, and the result is shown in Figure 4.10. Figures 4.10 a-d show the sample preparation procedure. Al film with thickness of 100 nm was deposited on a single-crystal h-BN sample by e-beam evaporator at a rate of 0.2 Å/s, which is the same as that used in the device fabrication in the main text. Silver conductive paint was used as adhesion to peel the Al film off the substrate to expose the interface. Then AFM images were acquired on h-BN surface and corresponding Al surface, as being marked in Figure 4.10d. The AFM image acquired on h-BN surface is shown in Figure 10e, and root mean square (RMS) roughness is ~0.06 nm. The AFM image acquired on Al surface is shown in Figure 4.10f, and the RMS roughness is ~0.11 nm. Since the h-BN surface is extremely flat within imaging scale (500 nm), the

roughness of Al interface reflects uneven gaps between the metal and h-BN film. Considering that the metallization is done at room temperature, the metal atoms may not have enough energy to get to their sites of exactly one van der Waals radius away. An effective distance d^* between positive and negative charges accumulated in the capacitor thus can be estimated by summing up the geometric distance (5.79 Å), quantum layer thickness (2.3 L), and effective vacuum layer thickness (2.68 Å), which yields 9.62 Å.

Figure 4.8i shows the temperature-dependent C-f sweep on capacitors with the size of 200×200 μm^2. The sweeping frequency ranges from 10 kHz to 2 MHz, and the temperature ranges from room temperature to 80 °C. The capacitance decreases almost linearly with the increase of temperature. The temperature capacitance coefficient (TCC) at 1 MHz is calculated using the following equation:[63]

$$TCC = \frac{\Delta C \times 10^6}{C \times \Delta T} \quad (4)$$

Using the capacitance at 23°C as reference, the TCC is calculated to be -1200 ppm/°C. The relationship between polarization P and relative permittivity ε_r can be expressed in the following equation:[64]

$$P = P_e + P_i + P_d + P_s = \varepsilon_0(\varepsilon_r - 1)E \quad (5)$$

where P_e is electronic polarization, P_i is ionic polarization, P_d is dipolar polarization, and P_s is space charge polarization. The decrease of capacitance with the increase of temperature may be due to the decrease of electronic polarizability and the decrease in the number of polarizable electrons per unit volume according to the Clausius-Mossotti

equation.[65] The capacitance decreases with the increase of frequency below 1 MHz, which may be attributed to the decrease of electronic polarizability, and the rapid decrease beyond 1 MHz may be attributed to the decrease of ionic polarizability.[64] However, even though similar phenomenon has also been observed in tri-layer h-BN capacitors,[37] it is theoretically not allowed in materials with small dielectric constant. While more investigation is needed to understand the reason, we hypothesize that it is related to the interface interaction between the monolayer h-BN and metal electrode, especially between the epitaxial h-BN and Ni (111) substrate surface, which may render it very different to its bulk or free-standing state. For thick h-BN films where the contribution of interface interaction is negligible, there is no apparent dielectric loss observed below 3 MHz.[19]

Figure 4.8j shows the tunneling current characteristics of 20 capacitors, with the same size of 200×200 μm^2. For each capacitor, we perform the forward sweeping first, then perform the reverse sweeping. Curves with the same color are from the same devices. The tunneling current density between dissimilar electrodes is expressed with the following Simmons equation (for $0 < V < \varphi_{min}/e$):[66]

$$J = \frac{e}{2\pi h d^2} \times \left[\bar{\varphi} \times e^{-\frac{4\pi d\sqrt{2m\bar{\varphi}}}{h}} - (\bar{\varphi} + eV) \times e^{-\frac{4\pi d\sqrt{2m(\bar{\varphi}+eV)}}{h}} \right], \quad (6)$$

where $\bar{\varphi} = (\ \varphi_1 + \varphi_2 - eV)/2$, is the average potential across the dielectric barrier, V is the applied voltage, e is the electron charge, m is the tunneling carrier's mass, h is the Planck's constant, and d is the tunneling distance. While some reports assumed that electrons are the tunneling carrier,[67, 68] some other reports assumed holes as the tunneling carrier.[69, 70] Obviously, it is still under debate on which type of carrier is tunneling carrier,

and more investigations are needed to reach a conclusive conclusion. There are many factors contributing to the inconclusiveness. One of them is originated from an uncertain estimation of the effective masses of the carriers. Most of the reports used 0.26 m_0 for effective electron mass, and 0.5 m_0 for effective hole mass, both values come from the paper of Ching et al.[71] While the tunneling happens perpendicular to the 2D plane, these two values are the in-plane effective carrier masses. Nevertheless, according to Ching et al,[71] "the effective mass for h-BN is highly anisotropic with average in-plane components a factor of 5 smaller than the components perpendicular to the plane". Specifically as reported in ref. [71], the out-of-plane effective electron mass is 2.21 m_0, and out-of-plane effective hole mass is 1.33m_0. For materials with apparent anisotropy, corresponding effective carrier masses in the tunneling direction should be used.[72, 73] Thus we will use out-of-plane effective masses in the calculations below.

Another parameter to determine is tunneling barriers for electrons and holes. Yoshiaki et al reported the Fermi level pinning effect at h-BN interface when heavy transition metals are used.[70] In general, Fermi level pinning happens at the interface where large amount of surface states exist, and it is usually related to defects at the dielectric/metal interface. For our monolayer h-BN MIM devices, it is unlikely that such large amount of surface states would exist while maintaining good insulating property. On the other hand, the Fermi level pinning observed in the multilayer h-BN MIM devices with heavy transition metals as electrode indicates that the h-BN surface was damaged,[70] which supports our hypothesis that heavy transition metal can damage h-BN film during metallization. Moreover, the Fermi level pinning in MoS_2 MIM devices was avoided by electrode transfer and low-

thermal-energy deposition of indium as mentioned above.[17, 20] Similarly in our case, we believe there is no Fermi level pinning since low-energy Al evaporation is employed. To the best of our knowledge, the absolute values of barrier heights ϕ_1 and ϕ_2 have not been experimentally determined to date. It is reported that the barrier height in the Au/h-BN/AFM tip and Au/h-BN/Au configuration is about 3 eV, and the tunneling carrier is assumed to be electron.[3, 68] In our earlier paper [13] and the references therein, Schottky barrier between Ni/h-BN for electrons is 3.0 eV. Thus, to estimate the tunneling current, we assume that ϕ_1 equals 3 eV, the bandgap of h-BN equals 6 eV,[39] the tunneling distance equals the geometric distance (5.79 Å), and the tunneling area is 200 μm × 200 μm. The tunneling current at 0.1 V would be 3.87 A assuming electrons are the tunneling carrier, and 10.8 A assuming holes are the tunneling carrier. Comparing to the measured tunneling current (~0.3 mA at 0.1 V) shown in Figure 4.8f, the calculated results are about four orders of magnitude larger. This discrepancy is originated from the fact that the actual tunneling area is different with the physical area of the device.[13] If we assume that the tunneling only happens in some local area, we can infer that the effective tunneling area is about 0.01% of the physical area of the devices, which is consistent with our previous report.[13] It should be noted that the Thomas-Fermi screen effect and the uneven interface distance were not considered in the above calculation. The justification is that the tunneling has the highest probability at the locations with thinnest barrier per quantum mechanics. On the other hand, if we assume an ideal case with the following two conditions: 1) the tunneling happens all over the physical area of the devices; 2) the same effective distance (9.62 Å) obtained from the capacitance measurement/discussion applies to the entire physical area of the devices

even if uneven interface distance is obvious across the device area, the electron tunneling current is estimated to be 0.23 mA, and the hole tunneling current is 1.41 mA at a bias of 0.1 V. The calculated tunneling currents versus applied voltages are plotted in Figure 4.8k. The hole current is colored in red, the electron current is colored in blue, and the experimental results from Figure 4.8j are colored in gray. As seen from the figure, both values are very close to the experimental results, especially the electron tunneling current, which lie within the range of our measured results. This situation prevents us from precisely determining which carrier is the dominating tunneling carrier. Based on the fact that the calculated electron tunneling current and hole tunneling current are not substantially different although hole current is larger than electron current, we hypothesize that in the present h-BN MIM system with monolayer h-BN film, both electrons and holes have participated in the tunneling process.

To study the relationship between the tunneling current and the bias polarity, we plotted the average difference between the forward and reverse currents versus the bias voltage, and the result is shown in Figure 4.8i. It turns out that the forward current is larger than the reverse current at the same bias. According to theoretical calculations, polarity dependent tunneling should only appear when the applied bias is larger than one of the barrier heights, the so-called field emission region.[66, 74] Our results show that even for the direct tunneling region, an asymmetric I-V characteristic appears, and the difference in the tunneling current can be fitted well with the following equation:

$$|i_{Forward}| - |i_{Reverse}| = A_1 exp\left(-{}^{V}/_{t_1}\right) + A_2 exp\left(-{}^{V}/_{t_2}\right), \quad (7)$$

where A_1, A_2, t_1, t_2 are constants, and V is the applied voltage. This asymmetric I-V relationship indicates that, thermionic emission might have also contributed to the measured current.[75]

4.4 Conclusion

Monolayer single-crystal h-BN films with a size of 1 in^2 were synthesized on single-crystal Ni (111) substrates obtained by high temperature annealing of Ni foil. By adopting an electropolishing procedure, the h-BN nucleation density and the growth speed increase significantly, and high-quality h-BN films could be obtained within one hour. Robust nano capacitors were fabricated on as grown monolayer single-crystal h-BN films with Al as the top electrode. The tunneling current mechanism with asymmetric metal electrodes and the nano-capacitance effect were studied in detail. The effective distance, which is larger than the geometric dielectric thickness, was introduced based on theoretical and experimental analysis to explain the capacitances of the MIM nano capacitors. Both electrons and holes may have been tunneling carriers contributing to the tunneling currents. Our studies provide an insight into quantum tunneling devices based on van der Waals materials. Finally, our experimental procedures are readily replicable, which provides a reliable method for developing practical devices based on monolayer single-crystal h-BN films.

4.5 Reference

1. Hattori, Y.; Taniguchi, T.; Watanabe, K.; Nagashio, K., Layer-by-Layer Dielectric Breakdown of Hexagonal Boron Nitride. *ACS Nano* **2015,** *9* (1), 916-921.

2. Lee, G.-H.; Yu, Y.-J.; Cui, X.; Petrone, N.; Lee, C.-H.; Choi, M. S.; Lee, D.-Y.; Lee, C.; Yoo, W. J.; Watanabe, K., Flexible and Transparent MoS_2 Field-Effect Transistors on Hexagonal Boron Nitride-Graphene Heterostructures. *ACS Nano* **2013,** *7* (9), 7931-7936.

3. Jang, S. K.; Youn, J.; Song, Y. J.; Lee, S., Synthesis and Characterization of Hexagonal Boron Nitride as a Gate Dielectric. *Sci. Rep.* **2016,** *6*, 30449.

4. Gupta, B. and Matte, H.R., Solution-Processed Layered Hexagonal Boron Nitride Dielectrics: A Route toward Fabrication of High Performance Flexible Devices. *ACS Appl. Electron. Mater.* **2019**. *1* (10), 2130-2139.

5. Pan, C.; Ji, Y.; Xiao, N.; Hui, F.; Tang, K.; Guo, Y.; Xie, X.; Puglisi, F. M.; Larcher, L.; Miranda, E., Coexistence of Grain-Boundaries-Assisted Bipolar and Threshold Resistive Switching in Multilayer Hexagonal Boron Nitride. *Adv. Funct. Mater.* **2017,** *27* (10), 1604811.

6. Qian, K.; Tay, R. Y.; Nguyen, V. C.; Wang, J.; Cai, G.; Chen, T.; Teo, E. H. T.; Lee, P. S., Hexagonal Boron Nitride Thin Film for Flexible Resistive Memory Applications. *Adv. Funct. Mater.* **2016,** *26* (13), 2176-2184.

7. Grosso, G.; Moon, H.; Lienhard, B.; Ali, S.; Efetov, D. K.; Furchi, M. M.; Jarillo-Herrero, P.; Ford, M. J.; Aharonovich, I.; Englund, D., Tunable and High-Purity Room Temperature Single-Photon Emission From Atomic Defects in Hexagonal Boron Nitride. *Nat. Commun.* **2017,** *8* (1), 1-8.

8. Lee, J. S.; Choi, S. H.; Yun, S. J.; Kim, Y. I.; Boandoh, S.; Park, J.-H.; Shin, B. G.; Ko, H.; Lee, S. H.; Kim, Y.-M., Wafer-Scale Single-Crystal Hexagonal Boron Nitride Film via Self-Collimated Grain Formation. *Science* **2018,** *362* (6416), 817-821.

9. Wang, L.; Xu, X.; Zhang, L.; Qiao, R.; Wu, M.; Wang, Z.; Zhang, S.; Liang, J.; Zhang, Z.; Zhang, Z., Epitaxial Growth of a 100-Square-Centimetre Single-Crystal Hexagonal Boron Nitride Monolayer on Copper. *Nature* **2019,** *570* (7759), 91-95.

10. Chen, T.-A.; Chuu, C.-P.; Tseng, C.-C.; Wen, C.-K.; Wong, H.-S. P.; Pan, S.; Li, R.; Chao, T.-A.; Chueh, W.-C.; Zhang, Y., Wafer-Scale Single-Crystal Hexagonal Boron Nitride Monolayers on Cu (111). *Nature* **2020,** *579* (7798), 219-223.

11. Zuo, Z.; Xu, Z.; Zheng, R.; Khanaki, A.; Zheng, J.-G.; Liu, J., In-situ Epitaxial Growth of Graphene/h-BN van der Waals Heterostructures by Molecular Beam Epitaxy. *Sci. Rep.* **2015,** *5*, 14760.

12. Schmid, U., The Impact of Thermal Annealing and Adhesion Film Thickness on the Resistivity and the Agglomeration Behavior of Titanium/Platinum Thin Films. *J. Appl. Phys.* **2008,** *103* (5), 054902.

13. Cui, Z.; He, Y.; Tian, H.; Khanaki, A.; Xu, L.; Shi, W.; Liu, J., Study of Direct Tunneling and Dielectric Breakdown in Molecular Beam Epitaxial Hexagonal Boron Nitride Monolayers Using Metal–Insulator–Metal Devices. *ACS Appl. Electron. Mater.* **2020,** *2* (3), 747-755.

14. He, Y.; Tian, H.; Das, P.; Cui, Z.; Pena, P.; Chiang, I.; Shi, W.; Xu, L.; Li, Y.; Yang, T., Growth of High-Quality Hexagonal Boron Nitride Single-Layer Films on Carburized Ni Substrates for Metal–Insulator–Metal Tunneling Devices. *ACS Appl. Mater. Interfaces* **2020,** *12* (31), 35318-35327.

15. Tian, H.; He, Y.; Das, P.; Cui, Z.; Shi, W.; Khanaki, A.; Lake, R. K.; Liu, J., Growth Dynamics of Millimeter-Sized Single-Crystal Hexagonal Boron Nitride Monolayers on Secondary Recrystallized Ni (100) Substrates. *Adv. Mater. Interfaces* **2019,** *6* (22), 1901198.

16. Kim, C.; Lee, K. Y.; Moon, I.; Issarapanacheewin, S.; Yoo, W. J., Metallic Contact Induced van der Waals Gap in a MoS_2 FET. *Nanoscale* **2019,** *11* (39), 18246-18254.

17. Liu, Y.; Guo, J.; Zhu, E.; Liao, L.; Lee, S.-J.; Ding, M.; Shakir, I.; Gambin, V.; Huang, Y.; Duan, X., Approaching the Schottky–Mott Limit in van der Waals Metal–Semiconductor Junctions. *Nature* **2018,** *557* (7707), 696-700.

18. Guo, N., Wei, J., Jia, Y., Sun, H., Wang, Y., Zhao, K., Shi, X., Zhang, L., Li, X., Cao, A. and Zhu, H., Fabrication of Large Area Hexagonal Boron Nitride Thin Films for Bendable Capacitors. *Nano Res.* **2013**, *6* (8), 602-610.

19. Ahmed, F.; Heo, S.; Yang, Z.; Ali, F.; Ra, C. H.; Lee, H. I.; Taniguchi, T.; Hone, J.; Lee, B. H.; Yoo, W. J., Dielectric Dispersion and High Field Response of Multilayer Hexagonal Boron Nitride. *Adv. Funct. Mater.* **2018,** *28* (40), 1804235.

20. Kim, B.K., Kim, T.H., Choi, D.H., Kim, H., Watanabe, K., Taniguchi, T., Rho, H., Kim, J.J., Kim, Y.H. and Bae, M.H., Origins of Genuine Ohmic van der Waals Contact Between Indium and MoS_2. *NPJ 2D Mater. Appl.* **2021**, *5* (1), 1-10.

21. Bonifas, A. P.; McCreery, R. L., 'Soft'Au, Pt and Cu Contacts for Molecular Junctions Through Surface-Diffusion-Mediated Deposition. *Nat. Nanotechnol.* **2010,** *5* (8), 612-617.

22. Haick, H.; Ambrico, M.; Ghabboun, J.; Ligonzo, T.; Cahen, D., Contacting Organic Molecules by Metal Evaporation. *Phys. Chem. Chem. Phys.* **2004,** *6* (19), 4538-4541.

23. Nakhaie, S.; Wofford, J.; Schumann, T.; Jahn, U.; Ramsteiner, M.; Hanke, M.; Lopes, J.; Riechert, H. Synthesis of Atomically Thin Hexagonal Boron Nitride Films on Nickel Foils by Molecular Beam Epitaxy. *Applied Physics Letters* **2015,** *106* (21), 213108.

24. Shi, Y.; Hamsen, C.; Jia, X.; Kim, K. K.; Reina, A.; Hofmann, M.; Hsu, A. L.; Zhang, K.; Li, H.; Juang, Z.-Y. Synthesis of Few-Layer Hexagonal Boron Nitride Thin Film by Chemical Vapor Deposition. *Nano Letters* **2010,** *10* (10), 4134-4139.

25. Ferguson, J.; Weimer, A.; George, S. Atomic Layer Deposition of Boron Nitride Using Sequential Exposures of BCl_3 and NH_3. *Thin Solid Films* **2002,** *413* (1-2), 16-25.

26. Esfahani, A.N., Malcolm, A.J., Xu, L., Yang, H., Storwick, T., Kim, N.Y. and Pope, M.A., Ultra-thin films of Solution-Exfoliated Hexagonal Boron Nitride by Langmuir Deposition. *J. Mater. Chem. C.* **2020**, *8* (39), 13695-13704.

27. Zhu, J., Kang, J., Kang, J., Jariwala, D., Wood, J.D., Seo, J.W.T., Chen, K.S., Marks, T.J. and Hersam, M.C., Solution-Processed Dielectrics Based on Thickness-Sorted Two-Dimensional Hexagonal Boron Nitride Nanosheets. *Nano Lett*. **2015**, *15* (10), 7029-7036.

28. Tian, H.; Khanaki, A.; Das, P.; Zheng, R.; Cui, Z.; He, Y.; Shi, W.; Xu, Z.; Lake, R.; Liu, J., Role of Carbon Interstitials in Transition Metal Substrates on Controllable Synthesis of High-Quality Large-Area Two-Dimensional Hexagonal Boron Nitride Layers. *Nano Lett.* **2018,** *18* (6), 3352-3361.

29. Khanaki, A.; Tian, H.; Xu, Z.; Zheng, R.; He, Y.; Cui, Z.; Yang, J.; Liu, J., Effect of High Carbon Incorporation in Co Substrates on the Epitaxy of Hexagonal Boron Nitride/Graphene Heterostructures. *Nanotechnology* **2017,** *29* (3), 035602.

30. Landolt, D., Fundamental Aspects of Electropolishing. *Electrochim. Acta* **1987,** *32* (1), 1-11.

31. Han, W.; Fang, F., Fundamental Aspects and Recent Developments in Electropolishing. *International Journal of Machine Tools and Manufacture* **2019,** *139*, 1-23.

32. Okazawa, T.; Nishizawa, T.; Nishimura, T.; Kido, Y., Oxidation Kinetics for Ni (111) and the Structure of the Oxide Layers. *Phys. Rev. B* **2007,** *75* (3), 033413.

33. Huda, M.; Kleinman, L., H-BN Monolayer Adsorption on the Ni (111) Surface: A Density Functional Study. *Phys. Rev. B* **2006,** *74* (7), 075418.

34. Grad, G.; Blaha, P.; Schwarz, K.; Auwärter, W.; Greber, T., Density Functional Theory Investigation of the Geometric and Spintronic Structure of h-BN/Ni (111) in View of Photoemission and STM Experiments. *Phys. Rev. B* **2003,** *68* (8), 085404.

35. He, Y.; Tian, H.; Khanaki, A.; Shi, W.; Tran, J.; Cui, Z.; Wei, P.; Liu, J., Large-Area Adlayer-Free Single-Layer h-BN Film Achieved by Controlling Intercalation Growth. *Appl. Surf. Sci.* **2019,** *498*, 143851.

36. Gorbachev, R.V., Riaz, I., Nair, R.R., Jalil, R., Britnell, L., Belle, B.D., Hill, E.W., Novoselov, K.S., Watanabe, K., Taniguchi, T. and Geim, A.K., Hunting for Monolayer Boron Nitride: Optical and Raman Signatures. *Small* **2011**, *7* (4), 465-468.

37. Hong, S.; Lee, C.-S.; Lee, M.-H.; Lee, Y.; Ma, K. Y.; Kim, G.; Yoon, S. I.; Ihm, K.; Kim, K.-J.; Shin, T. J., Ultralow-Dielectric-Constant Amorphous Boron Nitride. *Nature* **2020,** *582* (7813), 511-514.

38. Khan, M. H.; Huang, Z.; Xiao, F.; Casillas, G.; Chen, Z.; Molino, P. J.; Liu, H. K., Synthesis of Large and Few Atomic Layers of Hexagonal Boron Nitride on Melted Copper. *Sci. Rep.* **2015,** *5* (1), 1-11.

39. Elias, C.; Valvin, P.; Pelini, T.; Summerfield, A.; Mellor, C.; Cheng, T.; Eaves, L.; Foxon, C.; Beton, P.; Novikov, S., Direct Band-Gap Crossover in Epitaxial Monolayer Boron Nitride. *Nat. Commun.* **2019,** *10* (1), 1-7.

40. Auwärter, W.; Muntwiler, M.; Osterwalder, J.; Greber, T., Defect Lines and Two-Domain Structure of Hexagonal Boron Nitride Films on Ni (1 1 1). *Surf. Sci.* **2003,** *545* (1-2), L735-L740.

41. Fernández, L.; Makarova, A.; Laubschat, C.; Vyalikh, D. V.; Usachov, D. Y.; Ortega, J. E.; Schiller, F., Boron Nitride Monolayer Growth on Vicinal Ni (111) Surfaces Systematically Studied with a Curved Crystal. *2D Mater.* **2019,** *6* (2), 025013.

42. Liu, S.; Van Duin, A. C.; Van Duin, D. M.; Liu, B.; Edgar, J. H., Atomistic Insights into Nucleation and Formation of Hexagonal Boron Nitride on Nickel from First-Principles-Based Reactive Molecular Dynamics Simulations. *ACS Nano* **2017,** *11* (4), 3585-3596.

43. Park, H. J.; Cha, J.; Choi, M.; Kim, J. H.; Tay, R. Y.; Teo, E. H. T.; Park, N.; Hong, S.; Lee, Z., One-Dimensional Hexagonal Boron Nitride Conducting Channel. *Sci. Adv.* **2020,** *6* (10), 4958.

44. Yang, P.C., Prater, J.T., Liu, W., Glass, J.T. and Davis, R.F., The Formation of Epitaxial Hexagonal Boron Nitride on Nickel Substrates. *Journal of electronic materials*, **2005**, *34* (12), 1558-1564.

45. Abdulrahman, R.F. and Hendry, A., Solubility of Nitrogen in Liquid Nickel-Based Alloys. *Metallurgical and Materials Transactions B*, **2001**, *32* (6), 1103-1112.

46. Wu, B., Geng, D., Xu, Z., Guo, Y., Huang, L., Xue, Y., Chen, J., Yu, G. and Liu, Y., Self-Organized Graphene Crystal Patterns. *NPG Asia Materials*, **2013**, *5* (2), 36-e36.

47. Liu, S., Comer, J., Van Duin, A.C., Van Duin, D.M., Liu, B. and Edgar, J.H., Predicting the Preferred Morphology of Hexagonal Boron Nitride Domain Structure on Nickel from ReaxFF-Based Molecular Dynamics Simulations. *Nanoscale*, **2019**, *11* (12), 5607-5616.

48. Asano, T.; Uetake, N.; Suzuki, K., Mean Atomic Velocities of Uranium, Titanium and Copper During Electron Beam Evaporation. *J. Nucl. Sci. Technol.* **1992,** *29* (12), 1194-1200.

49. Derry, G. N.; Kern, M. E.; Worth, E. H., Recommended Values of Clean Metal Surface Work Functions. *J. Vac. Sci. Technol., A* **2015,** *33* (6), 060801.

50. Chauvet, C.; Laurent, C., Weibull Statistics in Short-Term Dielectric Breakdown of Thin Polyethylene Films. *IEEE Trans. Electr. Insul.* **1993,** *28* (1), 18-29.

51. Yang, Y., Fu, Q., Li, H., Wei, M., Xiao, J., Wei, W. and Bao, X., Creating a Nanospace under an h-BN Cover for Adlayer Growth on Nickel (111). *ACS Nano* **2015**, *9* (12), 11589-11598.

52. Brülke, C., Heepenstrick, T., Humberg, N., Krieger, I., Sokolowski, M., Weiß, S., Tautz, F.S. and Soubatch, S., Long Vertical Distance Bonding of the Hexagonal Boron Nitride Monolayer on the Cu (111) Surface. *J. Phys. Chem. C* **2017**. *121* (43), 23964-23973.

53. Bokdam, M., Brocks, G., Katsnelson, M.I. and Kelly, P.J., Schottky Barriers at Hexagonal Boron Nitride/Metal interfaces: A First-Principles Study. *Phys. Rev. B*, **2014**, *90* (8), 085415.

54. Zhou, L.G. and Huang, H., Are Surfaces Elastically Softer or Stiffer?. *Applied Physics Letters*, **2004**. *84* (11), 1940-1942.

55. Laturia, A., Van de Put, M.L. and Vandenberghe, W.G., Dielectric Properties of Hexagonal Boron Nitride and Transition Metal Dichalcogenides: from Monolayer to Bulk. *NPJ 2D Mater. Appl.* **2018**, *2* (1), 1-7.

56. Stengel, M.; Spaldin, N. A., Origin of the Dielectric Dead Layer in Nanoscale Capacitors. *Nature* **2006,** *443* (7112), 679-682.

57. Chang, L. W.; Alexe, M.; Scott, J. F.; Gregg, J. M., Settling the "dead layer" Debate in Nanoscale Capacitors. *Adv. Mater.* **2009,** *21* (48), 4911-4914.

58. Ku, H.; Ullman, F., Capacitance of Thin Dielectric Structures. *J. Appl. Phys.* **1964,** *35* (2), 265-267.

59. Chkhartishvili, L.; Beridze, M.; Dekanosidze, S.; Esiava, R.; Kalandadze, I.; Mamisashvili, N.; Tabatadze, G., How to Calculate Nanocapacitance. *Am. J. Nano Res. Appl*. **2017,** *5* (3-1), 9-12.

60. Ashcroft, N. W.; Mermin, N. D., Solid State Physics (saunders college, philadelphia, 1976). *Appendix N* **2010,** 166.

61. Schwarz, M., Riss, A., Garnica, M., Ducke, J., Deimel, P.S., Duncan, D.A., Thakur, P.K., Lee, T.L., Seitsonen, A.P., Barth, J.V. and Allegretti, F., Corrugation in the Weakly Interacting Hexagonal-BN/Cu (111) System: Structure Determination by Combining Noncontact Atomic Force Microscopy and X-ray Standing Waves. *ACS Nano*, **2017**, *11* (9), 9151-9161.

62. de Lima, L.H., Greber, T. and Muntwiler, M., The True Corrugation of a h-BN Nanomesh layer. *2D Mater*. **2020**, *7* (3), 035006.

63. Freire, F.N.A., Santos, M.R.P., Pereira, F.M.M., Sohn, R.S.T.M., Almeida, J.S.D., Medeiros, A.M.L., Sancho, E.D.O., Costa, M.M. and Sombra, A.S.B., Studies of the Temperature Coefficient of Capacitance (TCC) of a New Electroceramic Composite: $Pb(Fe_{0.5}Nb_{0.5})O_3$(PFN)–$Cr_{0.75}Fe_{1.25}O_3$(CRFO). *J. Mater. Sci.: Mater. Electron.* **2009**. *20* (2), 149-156.

64. Badr, A.M., Elshaikh, H.A. and Ashraf, I.M., Impacts of Temperature and Frequency on the Dielectric Properties for Insight into the Nature of the Charge Transports in the Tl_2S Layered Single Crystals. *J. Mod. Phys*, **2011**, 2011.

65. Cockbain, A.G. and Harrop, P.J., The Temperature Coefficient of Capacitance. *J PHYS D APPL PHYS*, **1968**. *1* (9), 1109.

66. Simmons, J. G., Electric Tunnel Effect Between Dissimilar Electrodes Separated by a Thin Insulating Film. *J. Appl. Phys.* **1963,** *34* (9), 2581-2590.

67. Iqbal, M.Z. and Faisal, M.M., Fowler-Nordheim Tunneling Characteristics of Graphene/hBN/Metal Heterojunctions. *J. Appl. Phys.* **2019**. *125* (8), 084902.

68. Lee, G.-H.; Yu, Y.-J.; Lee, C.; Dean, C.; Shepard, K. L.; Kim, P.; Hone, J., Electron Tunneling through Atomically Flat and Ultrathin Hexagonal Boron Nitride. *Appl. Phys. Lett.* **2011,** *99* (24), 243114.

69. Britnell, L., Gorbachev, R.V., Jalil, R., Belle, B.D., Schedin, F., Katsnelson, M.I., Eaves, L., Morozov, S.V., Mayorov, A.S., Peres, N.M. and Castro Neto, A.H., Electron Tunneling through Ultrathin Boron Nitride Crystalline Barriers. *Nano Lett.* **2012**, *12* (3), 1707-1710.

70. Hattori, Y., Taniguchi, T., Watanabe, K. and Nagashio, K., Determination of Carrier Polarity in Fowler–Nordheim Tunneling and Evidence of Fermi Level Pinning at the Hexagonal Boron Nitride/Metal Interface. *ACS Appl. Mater. Interfaces* **2018**. *10* (14), 11732-11738.

71. Xu, Y.N. and Ching, W.Y., Electronic, Optical, and Structural Properties of Some Wurtzite Crystals. *Phys. Rev. B*, **1993**, *48* (7), 4335.

72. Ilatikhameneh, H., Ameen, T., Novakovic, B., Tan, Y., Klimeck, G. and Rahman, R., Saving Moore's Law Down to 1 nm Channels with Anisotropic Effective Mass. *Sci. Rep.* **2016**, *6* (1), 1-6.

73. Robbins, M.C., Golani, P. and Koester, S.J., Right-Angle Black Phosphorus Tunneling Field Effect Transistor. *IEEE Electron Device Lett.* **2019**, *40* (12), 1988-1991.

74. Banerjee, S.; Zhang, P., A Generalized Self-Consistent Model for Quantum Tunneling Current in Dissimilar Metal-Insulator-Metal Junction. *AIP Adv.* **2019,** *9* (8), 085302.

75. Simmons, J. G., Potential Barriers and Emission-Limited Current Flow Between Closely Spaced Parallel Metal Electrodes. *J. Appl. Phys.* **1964,** *35* (8), 2472-2481.

Chapter 5: Summary

In summary, we discussed the molecular beam epitaxy of monolayer h-BN, and the fabrication and characterization of MIM devices on as grown films.

In the first project, we focused on the exploration of growth parameters for monolayer h-BN film. We find that the h-BN adlayers are formed at the h-BN/substrate interface through intercalation. The intercalation process is related to the interface space, h-BN edge atom state, and source density. Crystallographic defects such as grain boundary, scratches, pits, and dislocations promote the intercalation process by creating larger interface space. Hydrogen passivation of h-BN edge atoms promote intercalation process, while the carburization promotes the B-N bonding process and suppress the intercalation process. Larger source flux results in more B/N atoms at the interface, hence, also results the adlayer growth. By combining smooth Ni substrate, carburization, atomic source, and proper source flux, we achieved large-area adlayer-free monolayer h-BN films.

Following the research in our first project, we focused on studying the growth of h-BN on Ni substrate in our second project. Ni substrate evolves into two major surface direction after thermal annealing, (111) and (100). We find that the growth speed on (100) surface is faster than on (111) surface. While carburization promotes the h-BN growth speed on (100) surface, it hinders the growth on (111) substrate. DFT calculations reveal that subsurface interstitial carbon improves the absorption of B/N on (100) surface and impairs the absorption and diffusion of B/N on (111) surface. Even though no continuous film was obtained on (111) surface, our experimental results indicate that Ni (111) substrate has the

potential to grow single crystal h-BN film. The MIM devices fabricated on as grown monolayer h-BN film on Ni (100) has large breakdown voltage of around 0.85 V. However, the current before breakdown shows trap-assisted tunneling characteristic, indicating the presence of defects in as grown film.

Lastly, in project three, we focus on growing single crystal h-BN film and improving the performance of MIM devices. We obtained 1 $inch^2$ Ni (111) single crystal by thermal annealing at 1400 °C. Electropolishing was introduced which drastically increased the growth speed of h-BN on Ni (111). Wafer scale single-crystal monolayer h-BN film was obtained within growth time of 1h. Low-thermal-energy e-beam evaporation deposition of Al was introduced for device fabrication to prevent damage to h-BN film during metallization. In turn, robust nano capacitor was fabricated with record large specific capacitance. Effective distance, which is larger than the geometrical distance between two electrodes, was obtained based on the capacitance analysis, which also explains the small tunneling current before breakdown.

The research work in this dissertation presents a journey to bring monolayer h-BN film to reliable MIM device applications, and sheds light on the methodology of improving thin film growth parameters. There are a lot of progress being made at the time of writing. With the collaborative efforts of scientific workers, the real-world applications of van der Waals materials are promised to come.

Appendix: Publications

1. He, Y.; Li, Y.; Isarraraz, M.; Pena, P.; Tran, J.; Xu, L.; Tian, H.; Yang, T.; Wei, P.; Ozkan, C. S., Robust Nanocapacitors Based on Wafer-Scale Single-Crystal Hexagonal Boron Nitride Monolayer Films. *ACS Applied Nano Materials* **2021** (DOI: 10.1021/acsanm.1c00298)

2. He, Y.; Tian, H.; Das, P.; Cui, Z.; Pena, P.; Chiang, I.; Shi, W.; Xu, L.; Li, Y.; Yang, T., Growth of High-Quality Hexagonal Boron Nitride Single-Layer Films on Carburized Ni Substrates for Metal–Insulator–Metal Tunneling Devices. *ACS Applied Materials & Interfaces* **2020,** *12* (31), 35318-35327.

3. Cui, Z.; He, Y.; Tian, H.; Khanaki, A.; Xu, L.; Shi, W.; Liu, J. Study of Direct Tunneling and Dielectric Breakdown in Molecular Beam Epitaxial Hexagonal Boron Nitride Monolayers Using Metal-Insulator-Metal Devices. *ACS Applied Electronic Materials* **2020,** *2* (3), 747-755.

4. He, Y.; Tian, H.; Khanaki, A.; Shi, W.; Tran, J.; Cui, Z.; Wei, P.; Liu, J. Large-Area Adlayer-Free Single-Layer h-BN Film Achieved by Controlling Intercalation Growth. *Applied Surface Science* **2019,** *498*, 143851.

5. Tian, H.; He, Y.; Das, P.; Cui, Z.; Shi, W.; Khanaki, A.; Lake, R. K.; Liu, J. Growth Dynamics of Millimeter-Sized Single-Crystal Hexagonal Boron Nitride Monolayers on Secondary Recrystallized Ni (100) Substrates. *Advanced Materials Interfaces* **2019,** *6* (22), 1901198.

6. Tian, H.; Khanaki, A.; Das, P.; Zheng, R.; Cui, Z.; He, Y.; Shi, W.; Xu, Z.; Lake, R.; Liu, J. Role of Carbon Interstitials in Transition Metal Substrates on Controllable Synthesis of High-Quality Large-Area Two-Dimensional Hexagonal Boron Nitride Layers. *Nano Letters* **2018,** *18* (6), 3352-3361.

7. Khanaki, A.; Tian, H.; Xu, Z.; Zheng, R.; He, Y.; Cui, Z.; Yang, J.; Liu, J. Effect of High Carbon Incorporation in Co Substrates on the Epitaxy of Hexagonal Boron Nitride/Graphene Heterostructures. *Nanotechnology* **2017,** *29* (3), 035602.

8. Zheng, R.; Khanaki, A.; Tian, H.; He, Y.; Cui, Y.; Xu, Z.; Liu, J. Precipitation Growth of Graphene under Exfoliated Hexagonal Boron Nitride to Form Heterostructures on Cobalt Substrate by Molecular Beam Epitaxy. *Applied Physics Letters* **2017,** *111* (1), 011903.